RADIATIVE CHARACTERIZATION OF ATMOSPHERIC AEROSOLS OVER SELECTED URBAN, RURAL AND MARITIME SITES OF KENYA USING SUN SPECTROPHOTOMETRY

BY

MAKOKHA JOHN WANJALA

B.Sc. (Hons)

Thesis submitted in partial fulfillment of the requirements for the degree of Master of Science (MSc) in Physics, University of Nairobi.

Declaration

This thesis is my own work and has not been examined or submitted for examination in any other university.

MAKOKHA JOHN WANJALA

I56/71197/2007

Signature……Date……

This thesis has been submitted for examination with our approval as supervisors.

1) Dr. J.N. Kimani

   Department of Physics

   University of Nairobi

   Signature……

   Date…….

2) Dr. H.K. Angeyo

   Department of Physics

   University of Nairobi

   Signature……

   Date…….

Dedication

To my son Bendtner, daughter Grace, wife Ann, parents, brothers, sisters and friends.

Acknowledgements

I would like to acknowledge the support, advice and constructive criticism by my supervisors Dr. J.N. Kimani and Dr. H.K. Angeyo. I acknowledge the support given to me by my colleagues, staff and Chairman of the Department of Physics, University of Nairobi not only in academics but also in challenging moments I underwent during this work. My sincere gratitude goes to Dr. K. Kaduki for facilitating acquisition of meteorological data from the Kenya Meteorological Department, which made this work a success. I thank the University of Nairobi for the scholarship and financial support given to me during the study. I also wish to acknowledge AERONET Network team (Brent Holben and staff) for installing, maintaining and even allowing me to use the data derived from sun photometers that made this work a reality. I wish to offer my sincere gratitude to all NASA officials particularly Dr. Thomas Charlock and Dr. Zhonghai Jin (online COART model) and Steve Kempler (MODIS satellite data) and their staff for maintaining and allowing me to use the NASA Goddard Earth Sciences (GES) data and information needs that made this work a success. Lastly I wish to offer my sincere thanks to my wife Ann, daughter Grace, son Bendtner, parents, brothers, sisters and friends for their patience, support and love. Above all, God deserves all my adoration and praise for strengthening me throughout this work.

Abstract

Atmospheric aerosols modulate the radiative budget and ambient air quality of the atmosphere, thus, there is a need to develop both analytical and computational methodological techniques that determine their physical, chemical and optical properties in order to characterize and model their effects. This thesis embodies the results of the derivation of radiative characteristics of the atmosphere over Nairobi (2006-2008), Mbita (2007) and Malindi (2008) using aerosol data obtained from sun spectrophotometry**.** Aerosol optical depths (τ), single scattering albedo (ω), angstrom exponent (α), asymmetry factor (g), real (n) and imaginary (k) refractive indices at zero Solar Zenith Angle (SZA) were derived through AErosol RObotic NETwork (AERONET) framework. Temporal and spatial characteristics in τ and α were investigated using multivariate techniques viz. Principal Component Analysis (PCA), Partial Least Squares Discriminant Analysis (PLS-DA), Principal Component Regression (PCR) and Hierarchical Cluster Analysis (HCA). Annual averages of the optical properties together with selected physico-chemical properties i.e. aerosol number densities and extinction cross section were determined. The Coupled Ocean and Atmosphere Radiative Transfer (COART) model was used to solve the radiative transfer equation (RTE) for an atmosphere assumed to be purely impacted by aerosols of different sizes and estimated their radiative impacts.

The use of multivariate chemometric techniques revealed that temporal and spatial characteristics of both τ and α over the study sites are modulated by weekly total rainfall, relative humidity, temperature, aerosol hygroscopic properties, aerosol burden, aerosol mode of generation and composition, both local air circulation and urban heat island effects. There was no significant spectral dependence in ω, g and both n and k at zero SZA over the study sites. Comparison of the measured τ and α from AERONET at λ = 500 nm and 440/675 nm respectively was achieved by utilizing Moderate Resolution Imaging Spectrometer (MODIS) data at 550 nm and 470/660 nm. The values agreed to within 12.4 % and 10.9 % levels of accuracy respectively, showing consistency in the two aerosol remote sensing techniques. There was a declining loss in radiant energy with increasing aerosol particle sizes over the sites of study which is associated to increasing heating effect of the incoming solar radiation. Radiative characteristics (spectral irradiance, integrated fluxes, reflectance) over Nairobi depicted temporal variations as influenced by rainfall distribution. There was an increase in up/down irradiance ratio of spectral irradiance of 2.6 %, 6.7 %, 7.2 % and 2.4 % and a drop of the ratio by 2.7 %,

12.2 %, 50.6 % and 25.6 % for 2007-2008 for λ = 440 nm, λ = 675 nm, λ = 870 nm and λ = 1020 nm respectively for 2006-2007 across all wavelength channels as impacted on by the total amount of rainfall received. Up/down integrated flux ratio remained virtually constant for time considered over each site. Utilizing these data, radiative forcing due to atmospheric aerosols was estimated, and found to remain relatively constant at $0.46\,K/(\mathrm{W/m^2})$ for all the three sites despite the observed differences in the various aerosol particle properties dominating the sites.

TABLE OF CONTENTS

CHAPTER 4: MATERIALS AND METHODS

LIST OF TABLES

LIST OF FIGURES

LIST OF SYMBOLS/ ACRONYMS

AERONET	AErosol RObotic NETwork
ANOVA	Analysis of Variance
BC	Black Carbon
BOA	Bottom of Atmosphere
CARES	Carbonaceous Aerosol and Radiative Effects Study
CCN	Cloud Condensation Nuclei
CDISORT	Coupled DIScrete Ordinate Radiative Transfer
COART	Coupled Ocean Atmosphere Radiative Transfer
CSPHOT	Cimel sun-photometer
GCM	Global Climate Model
GES-DISC	Goddard Earth Sciences Data and Information Services Center
GIOVANNI	GES-DISC Interactive Online Visualization ANd aNalysis Infrastructure
HCA	Hierarchical Cluster Analysis
ISDAC	Indirect and Semi-Direct Aerosol Campaign
MAX-DOAS	Multi-axis Differential Optical Absorption Spectroscopy
MODIS	MOderate-resolution Imaging Spectroradiometer
MOVAS	MODIS Online Visualization and Analysis System
MISR	Multi-angle Imaging Spectrometer
NASA	National Aeronautics and Space Administration
PCA	Principal Components Analysis
PCR	Principal Component Regression
PLS	Partial Least Squares
PLS-DA	Partial Least Squares Discriminant Analysis
SAL	Saharan Air Layer
STE	Stratospheric-Tropospheric Exchange
SZA	Solar Zenith Angle
TOA	Top of Atmosphere
TOMS	Total Ozone Mapping Spectrometer
TSI	Total Solar Irradiance
TSP	Total Suspended Particulate matter

RF	Radiative Forcing
RTE	Radiative Transfer Equation
τ	Aerosol Optical Depth
α	Angstrom exponent
g	Asymmetry factor
N	Aerosol number density
Ω	Climate sensitive parameter
n	Real refractive index
k	Imaginary refractive index
λ	Wavelength
ω	Single scattering albedo
M	Air mass
$P(\theta)$	Phase function
θ	Scattering angle
δ_e	Extinction cross section
r	Radius
α	Angstrom exponent
β	Angstrom turbidity coefficient
$n_c(r)$	Aerosol size distributions
$Q_{Ext}(r,\lambda,m)$	Mie extinction efficiency parameter
δ_e	Extinction cross section
$E_o(z,\lambda)$	Spectral irradiance
W	Week
ΔT_s	Equilibrium global mean surface temperature change
F_o	Solar beam intensity at the top of the atmosphere
Φ_o	Azimuthal angle for incident solar beam
μ_o	Cosine of the solar zenith angle
$I(\tau,\mu,\Phi)$	Specific intensity

CHAPTER 1

INTRODUCTION

1.0. Background

Aerosols are solid or liquid particles suspended in the atmosphere. They originate from both natural and man-made (anthropogenic) sources [Seinfeld and Pandis, 1998]. Aerosols constitute one of the most variable components of the earth's atmospheric environment; as a result they influence the energy budget and climate in numerous ways. They directly affect the radiation budget by absorbing and scattering solar radiation. Scattering of incoming solar radiation by aerosols yields a cooling effect on the atmosphere while absorption of incoming solar radiation has a warming effect; these effects are highly dependant on both the physical, chemical and optical properties of atmospheric aerosols. Aerosols also indirectly modify the properties of clouds by acting as Cloud Condensation Nuclei (CCN) that aid in the formation of cloud droplets.

Due to aerosols' role in modulating the radiative budget and ambient air quality of the atmosphere, there is need to develop both analytical and methodological techniques to determine as well as study their physical, chemical and optical properties in order to better characterize and model their environmental effects. This can be achieved by univariate techniques though the multivariate nature of the environment calls for more advanced techniques of analysis. Further more, applying univariate tests repeatedly increases the likelihood of an observation occurring by chance (the false-positive result). Hence, the use of multivariate techniques is advantageous since they are capable of handling a group of variables simultaneously. This can aid capture information about correlated trends in the measured and derived aerosol optical properties.

This thesis embodies the results of the radiative characterization study of atmospheric aerosols over selected urban (Nairobi-1S, 36E, elevation 1650 m), rural (Mbita-0S, 34E, elevation 1125 m) and maritime (Malindi-2S, 40E, elevation 12 m) sites of Kenya using sun spectrophotometry.

These results have been obtained in the framework of AErosol RObotic NETwork (AERONET). AERONET is a federated network of ground-based instruments and data archive for aerosol characterization of spectrophotometric measurements at 340 nm, 380 nm, 440 nm, 500 nm, 675 nm, 870 nm, 940 nm (water vapor channel) and 1020 nm wavelength channels in which direct sun measurements with a 1.2^{o} full field of view made every 15 minutes [Holben *et. al*, 1998]. Direct sun measurements are made in the above stated wavelength channels while the sky measurements are performed at 440 nm, 675 nm, 870 nm and 1020 nm.

AERONET aerosol optical depths (τ) corrected to zero Solar Zenith Angle (SZA) for Nairobi in 2006-2008, Mbita (2007) and Malindi (2008), selected aerosol optical properties (single scattering albedo (ω), angstrom exponent (α), asymmetry factor (g), real (n) and imaginary (k) refractive indices) were derived. τ and α were then grouped into Early Morning (7-8:59 AM), Late Morning (9-10:59 AM), Early Afternoon (11AM-12:59 PM) and Late Afternoon (1-3:30 PM) time intervals across all the possible wavelength channels for each site. This was done in order to aid in studying the temporal characteristics in both τ and α using multivariate chemometric techniques. Temporal characteristics in τ were studied using Principal Component Analysis (PCA) and Partial Least Squares Discriminant Analysis (PLS-DA) while that of α was through PLS-DA and Principal Component Regression (PCR) which validated each other.

On the other hand, Hierarchical Cluster Analysis (HCA) was used in the study of spatial characteristics by loading weekly τ and α into a MATLAB 7.1 algorithm and displaying in form of dendrograms. Validation of the measured τ and α from AERONET at 500 nm and 440/675 nm respectively was achieved by utilizing Moderate Resolution Imaging Spectrometer (MODIS) data acquired on the Aqua and Terra satellites at 550 nm and 470/660 nm. Radiative characteristics (i.e. spectral irradiance, integrated fluxes, reflectance) of aerosols over the study sites were determined utilizing the Coupled Ocean and Atmosphere Radiative Transfer (COART) model. The model was used to solve the radiative transfer equation (RTE) for an atmosphere assumed to be modulated by aerosols of different sizes only.

The study was aimed at deriving the radiative characteristics of atmosphere over Nairobi, Mbita and Malindi using aerosol data obtained from sun spectrophotometry. An outline of a brief

background on atmospheric aerosol studies and how this work relates to such studies is given. Chapter 2 outlines an in-depth discussion of related work carried out by other researchers. It also spells out the shortcomings of previous works and what the current work seeks to resolve. Chapter 3 deals with the theoretical background which includes the mathematical description of various aspects (aerosol properties, multivariate techniques, principle of sun photometry and radiative transfer modeling according to the COART-model under various assumptions). Chapter 4 details the materials and methods by which various optical properties of aerosols were retrieved from the AERONET sun photometer measurements and how they were utilized to obtain both radiative characteristics and forcing over the study sites.

In Chapter 5 gives a detailed discussion of the temporal and spatial characteristics, with respect to aerosol particle sizes for both τ and α using univariate and multivariate techniques. The spectral dependence of τ, ω, g, n and k are discussed; validation of both τ and α AERONET data was accomplished by the MODIS measurements. Physico-chemical properties (i.e. flux loss, aerosol number densities) were also determined. Lastly, utilizing τ, ω, and g, under various assumptions, radiative characteristics were obtained by the COART-model from which radiative forcing was estimated. Finally, Chapter 6 gives a summary of the findings and discusses them. It also gives the conclusion and perspectives to be pursued in future studies.

1.1 Statement of the Problem

Radiative forcing by natural and anthropogenic aerosols presently presents one of the most uncertain aspects of climate models due to various atmospheric processes e.g. coagulation, cloud cycling and long distance transport [Hansen *et. al.*, 1997; Penner *et. al.*, 2002]. Since aerosols are highly non-uniform in their distribution and physico-chemical properties in the atmosphere, they pose a challenge in their general utility, for instance in climate modeling [Hansen *et. al.*, 1998]. Atmospheric aerosols, among other influences perturb the radiation budget of the earth directly by scattering and absorbing the incoming and outgoing solar radiation, and indirectly by regulating cloud condensation through nucleation; therefore they may be considered as an important parameter in climate and air quality studies. The radiative forcing effects of aerosols on climate depends on aerosol properties such as the physico-chemical character (aerosol number

density, chemical composition, size fraction, e.t.c) and both scattering and absorption cross-section profiles.

In the East African region, there is not only need to measure the atmospheric aerosol optical properties namely aerosol optical depth (τ), single scattering albedo (ω), angstrom exponent (α), complex refractive index (both real (n) and imaginary (k)), asymmetric factor (g) and extinction cross section but also to utilize these measurements and compute the radiative characteristics, ambient air quality, climate and health effects as modulated by aerosol particles in the atmosphere over areas with known anthropogenic influence (e.g. Nairobi), rural (e.g. Mbita) and maritime (e.g. Malindi) and for use and inclusion into global climate modeling and air quality management models. This is because there is limited knowledge on aerosol optical properties, which currently impedes the quantitative assessment of the radiative characteristics of the lower atmosphere and therefore the energy balance of the regional atmosphere. This cannot be achieved with studies performed elsewhere owing to the tremendous variations in atmospheric aerosol characteristics.

1.2 Justification and Significance of the Study

Atmospheric characteristics such as pressure, humidity, wind direction and speed, and temperature are altered by aerosol profiles in the upper levels of the atmosphere. Because of this, aerosols influence the weather experienced near the surface of the earth. Aerosols, among other influences significantly impact the Earth's radiation budget directly through scattering, reflection and absorption of incoming solar radiation and indirectly impact on cloud formation as well as precipitation. Characterization of the spectral dependence of aerosol optical properties in the atmosphere is important for yielding data and information useful for modeling of the radiative effects of aerosols on the atmosphere. On the other hand, there is a large uncertainty in climatic and health effects of atmospheric aerosols in East Africa. This is due to the poor state of knowledge of the chemical, physical and optical properties of the region's aerosols, which can not be obtained from studies performed elsewhere owing to the tremendous variations in atmospheric aerosol characteristics. The knowledge of radiative characteristics of the atmosphere

is key in the development of climate models that can be used for prediction of climate change and also in the modeling of the impact of aerosols on environmental pollution and human health.

1.3 Objectives

1.3.1 General Objective

The main goal of this work was to derive the radiative characteristics of atmosphere over Nairobi, Mbita and Malindi using aerosol data obtained from sun spectrophotometry.

1.3.2 Specific Objectives

i. To retrieve aerosol optical properties, correct to zero SZA and perform univariate investigations of the temporal characteristics of aerosol optical depth (τ) with respect to rainfall and temperature over the study sites.
ii. To exploit multivariate chemometric techniques to explore temporal and spatial relationships in aerosol optical depth (τ) and angstrom exponent (α) values in the measured wavelength channels with respect to rainfall, relative humidity and temperature over Nairobi, Mbita and Malindi.
iii. To compare some of the above derived sun photometry measurements namely τ and α using MODIS satellite data.
iv. To study the spectral dependencies and correlation with rainfall, relative humidity and temperature in the measured aerosol optical depth (τ) and derived single scattering albedo (ω), real (n) and imaginary (k) refractive indices, and asymmetric factor (g) over the study sites.
v. To use the above measured and computed data and information to determine extinction cross-section and aerosol number density in different aerosol size fractions over Nairobi, Mbita and Malindi.
vi. To utilize the measured and derived data in (i)-(iv) above to solve the radiative transfer equation in order to derive the radiative characteristics of the studied atmosphere as impacted by aerosol particles and further estimate radiative forcing over the study sites.

CHAPTER 2

LITERATURE REVIEW

2.0 Preview

The Earth's atmosphere is a layer of gases surrounding the solid core and is maintained by the earth's gravity. It consists of various gases that include greenhouse gases and water vapor as indicated in Table 2.1. These gases play a major role in tropospheric chemistry, which includes stratospheric-tropospheric exchange processes. In addition to this, the atmosphere also contains aerosols. Aerosols are known to alter the radiative characteristics of the atmosphere. There are two types of aerosols, classified according to their size namely fine (particle diameter 0.001-0.1μm) and course aerosols (≥ particle diameter 1μm). Aerosols are introduced into the atmosphere as a result of both natural and human (anthropogenic) activities such as industrial emissions, biomass burning and agricultural sources. The global aerosol distribution be it spatial or vertical is uncertain due to various atmospheric processes e.g. coagulation, cloud cycling, aerosol production and transport mechanisms, sources and varying climatic conditions [Hansen *et. al.*, 1997; Penner *et. al.*, 2002].

Table 2.1: Composition of dry unpolluted air by volume [Source: Brimblecombe, 1996]

Nitrogen	78.084%	Methane	1.6 ppm
Oxygen	20.946%	Krypton	1.14 ppm
Argon	0.934%	Hydrogen	0.5 ppm
Carbon dioxide	360 ppm (variable)	Nitrous oxide	0.3 ppm
Neon	18.18 ppm	Xenon	0.087 ppm
Helium	5.24 ppm		

The scattering and absorption properties of aerosols depends on the chemical nature of these aerosols; for example, due to their size and composition, organic aerosols and soil dust absorb incoming radiation and re-emit the same to heat up the atmosphere thus increasing the atmospheric temperature profile (positive radiative forcing). These aerosol particles are

introduced into the atmosphere through combustion of biomass and fossil fuel [Penner *et. al*., 1992]. Sulfate-dominated aerosols scatter the incoming radiation into the atmosphere thus reducing temperature on the surface (negative radiative forcing). The principal anthropogenic source of sulfur is fossil fuels, which is emitted as SO_2 during combustion and oxidized in the atmosphere to become mainly sulfuric acid. The balance between dust absorption and scattering determine aerosol ability to mitigate the greenhouse effect and to affect atmospheric heating rates and cloud formation [Alpert *et al*., 1998]. Presently, dust absorption is uncertain and is usually expressed in terms of imaginary index of refraction (k) [Sokolik and Toon, 1996].

Aerosol optical properties (aerosol optical depth (τ), single scattering albedo (ω), asymmetric factor (g), real (n) and imaginary (k) refractive index) can be obtained by either passive or active remote sensing. These properties are key in understanding the radiative properties of an atmosphere under study. To fully understand these radiative properties, there are a number of aerosol campaigns, besides AERONET, that furnish information on aerosol optical properties through passive remote sensing. These include ground-based spectroscopic techniques such as the Multi-axis Differential Optical Absorption Spectroscopy (MAX-DOAS) which can also be used to retrieve aerosol profiles. The MAX-DOAS network has stations at different latitudes which can also be used for validation of satellite-based measurements of trace gases [Witrock *et. al.,* 2004]. Indirect and Semi-Direct Aerosol Campaigns (ISDAC) is an intensive cloud and aerosol observing system that facilitates both aerosol and cloud studies over the North Slope Alaska. Carbonaceous Aerosol and Radiative Effects Study (CARES), is centered on making field measurements of different types of atmospheric carbonaceous aerosols and their climate effects [Ghan *et. al.,* 2008].

A number of operational satellite sensors are available from NASA. These include, Total Ozone Mapping Spectrometer (TOMS); Moderate Resolution Imaging Spectrometer (MODIS) on Aqua and Terra satellites and Multi-angle Imaging Spectrometer (MISR) that is aboard instrument of the Earth Observing System (EOS) spacecraft providing a globally, radiometrically calibrated, georectified and co-registered imagery at nine viewing angles and four Vis-NIR spectral bands. Satellite born aerosol measurements have the advantage that they can cover the entire earth in a

day although only one or two observations can be made on a given position each day. Both ground-based and satellite observations are vital for different situations as well as for cross-validation of each other. AERONET, which is a ground based network, was used in this work not only because of its availability over the sites under consideration but also due to the fact that we can obtain data as many times as possible over the sites of study per day.

2.1 Background on AERONET

AERONET is a federated international network which was founded in 1993 and co-coordinated by National Aeronautics and Space Administration (NASA) Goddard Space Flight Centre that maintains more than 180 automatic sun/sky radiometers worldwide [Holben *et. al.,* 1998]. The main objectives of AERONET are to asses aerosol optical properties and validate satellite retrievals of aerosol optical parameters based on its ground measurements [Holben *et. al.,* 2001]. The measurement system is a solar powered weather hardy robotically pointed sun and sky radiometer based on the CIMEL Electronique 318A technique. This instrument has approximately a 1.2^{o} full field of view and two silicon detectors for measurement of direct sun, aureole and sky radiance. It utilizes 33 cm collimators which are designed for 10^{-5} stray light rejection for measurements of aureole 3^{0} from the sun. A robot mounted sensor head is parked pointed nadir when idle to prevent contamination of optical windows from rain and foreign particles. The radiometer makes only two basic measurements, either directly sun or sky, both within several programmed sequences that are discussed in details [Holben *et. al.,* 1998].

2.2 Aerosol Optical Properties

Aerosol optical properties are key in studying both the physical and radiative nature of atmospheres under study. These include aerosol optical depth (τ), which is a fraction of solar radiation that is not scattered or absorbed on its path in the atmosphere (it is also a measure of atmospheric turbidity). Derived optical properties include ω, which is the ratio of scattering efficiency to total extinction radiation. The angstrom exponent (α) is computed from two different wavelengths (λ). α is also an indicator of aerosol particle size variation and spectral variation in τ. Both real (n) and imaginary (k) refractive indices are indicators of aerosol

scattering and absorption properties respectively. Asymmetric factor (g) describes how much forward/backward scattering of the incoming solar radiation by aerosol particles dominates a particular atmosphere.

Low (0.056) values in winter and high (0.43) values in summer of τ are reported over Armilla, Granada in Spain [Alados-Arboleda *et. al.,* 2003]. The later was attributed to several feedback processes such as photochemical conversions of gaseous pollutants to secondary aerosols, low rainfall rates that enhanced extreme soil aridity hence high mineral dust loading, reduction of particulate scavenging potential through wet deposition and high frequency of Saharan dust incursions and vice versa for the former case. It was also found that a mean τ of 0.18 ($\pm$ 0.14) at λ=440 nm using CIMEL sun photometer [Toledano *et. al.,* 2009]. This mean exhibits two peaks during the year i.e. end of winter and during summer. This phenomenon is related to the seasonal pattern of dust aerosols which arrive at south-western Iberian Peninsula from North Africa. Low τ values of 0.28 at λ= 500 nm are attributed to more frequent rains in winter and few occurrences of dust events while maximum values of 0.83 at the same wavelength at Quarzazate (Morocco) during the Saharan Mineral Dust Experiment in May-June 2006. Measured τ values increase steadily from very low background value (less than 0.2) to very large values in few days (5-10 days) then drop sharply to a very low value in less than a day over northern China [Li *et. al*., 2007]. The sudden drop was associated to changes in air mass due to the passage of cold fronts.

Licor spectral data series showed a mean τ value at λ=500 nm of 0.12 for coastal marine aerosols, which was linked to frequent desert episodes, continental and polluted local influences [Vergaz *et. al.,* 2005]. Air craft *in situ* measurements showed a mixture of dust and biomass burning aerosol [Johnson *et. al.,* 2009]. This indicated a τ of 0.79 at λ=550 nm that compared well against the τ obtained from Banizoumbou AERONET site (τ = 0.74) while that of microtops sun photometer was τ = 0.72. This suggested that both biomass burning aerosol and mineral dust were equally important contributors to the τ values at this wavelength. Average τ at λ=750 nm for eight stations in China was also computed [Xia *et. al.,* 2005]. The values obtained ranged from 0.32 (Ejinaqi) to 0.68 (Beijing). The average coefficient of variation between the sites was 70 %, this was dominantly contributed by dust events over western China. A mean τ value of 0.07 (at λ=500 nm) was obtained over Pacific Ocean [Ramanathan *et. al*., 2001]; this agrees

with the recently calculated optical depth of 0.07 for natural component of aerosol in the polluted Indian Ocean, based on chemical analysis.

Perrone and others also noted that τ (at λ=441 nm) for every 15-day averaged values were larger than 0.2 from April to September 2003 and lower than 0.2 from October 2003 to March 2004 over south east Italy [Perrone *et. al*., 2005]. These large τ values indicate high concentration of aerosol particles characterized by high scattering and absorption coefficients. Aerosol optical depth (τ) values taken at 15-day averages span the range 0.2-0.4 for both spring and summer, while in autumn and winter, they vary between 0.1-0.2 [Perrone *et. al*., 2005]. This shows that the impact of continental pollution from Central and Eastern Europe, maritime and long-range transport of polluted air masses from Indian Ocean, mineral dust from North Africa and sea spray from the Mediterranean Sea over south east Italy dominates during spring and summer seasons. In Bamzoumbou, Niger, τ at λ=500 nm remains high (larger than 0.2) throughout the year with an annual average of 0.48. In Mongu, Zambia, τ at λ=500 nm was found to be as high as 0.8. Most influence on τ over these towns under study at this wavelength was due to the mixture of biomass burning aerosol and mineral dust [Liousse *et. al*., 1995].

Monthly mean values of ω at λ=675 nm and λ=778 nm vary having mean values of 0.940±0.014 and 0.934±0.015 respectively [Alados-Arboleda *et. al.,* 2004]. This depicts a temporal evolution of monthly mean ω at all wavelengths analyzed in the study. Single scattering albedo (ω) values at λ=368 nm vary between 0.923 and 0.963 with a mean value of 0.946±0.009 while ω at λ=500 nm range between 0.928 and 0.966 with a mean value of 0.948±0.011 [Alados-Arboleda *et. al.*, 2004]. These values were coherent with those obtained at Goa, India indicating that ω at λ=440 nm ranges from 0.88 to 0.93 [Leon *et. al.*, 2002]. At the island of Lampedusa in the Mediterranean Sea, values of ω at λ=532nm in the range 0.78-0.95 were obtained for aerosols originating from North Atlantic and Europe [Di Iorio *et. al*., 2003]. Time series analysis showed an evident existence of seasonal pattern with low values associated with winter conditions and vice versa for summer. The predominant aerosols in winter tend to be more absorbent due to greater combustion, traffic and other diesel engine systems that promote primary soot.

Single scattering albedo (ω) in the range 0.95-0.85 can change the radiative forcing from negative to positive. For heavy dust, ω was reported to be 0.87 [Levin *et. al*., 1980]. Urban

aerosols characterized at λ=450 nm show ω spanning the range 0.942-0.984 which indicates high degree of scattering [D'almeida *et. al*., 1991]. For dry externally mixed urban aerosols, the mean value of ω is 0.94 and reduces to 0.91 for dry internally mixed urban aerosols [Levoni *et. al*., 1997]. High ω values indicate elevated concentration of deflecting aerosols e.g. sulfates with low levels of absorbing properties. Studies over south east Italy for ω at λ=440 nm in 15-day averages span between 0.93-0.95 in spring and summer, evident of high concentration of absorbing aerosols e.g. mineral dust; and 0.97-0.98 in autumn and winter that is dominated by a mixture of scattering and absorbing aerosols [Perrone *et. al*., 2005].

Studies also indicate that Saharan and Arabian dust particles make ω as low as 0.08-0.09 because of the strong absorption of direct solar radiation [Toledano *et. al.,* 2009]. In Southern Africa, ω is as low as 0.08 in dry seasons due to predominant mineral dust incursions [Eck *et. al*., 1998]. AERONET studies conducted in Cuiaba, Brazil for 1993-1994 periods show that average ω at λ=670 nm is 0.87±0.08, this was indicative of dominant forest fires promoting primary biomass burning aerosols that absorb the incoming solar radiation [Dubovik *et. al*., 1998]. From the Global Climate Models (GCMs), aerosols such as sulfates have ω=0.95 and that of organics ω=0.92, while that of soil dust is wavelength-dependent [Penner *et. al*., 1992].

In a study over Beijing, it was noted that ω at λ=870 nm is within the range of 0.76-0.94 with an average value of 0.85 that suggests a considerable absorption of radiation by aerosols as a result of vehicular emissions [Li *et. al.,* 2004]. The total yearly mean of ω for six cities during 1993-2001 changed from 0.851 to 0.803 with a mean value of 0.827. This shows an increasing concentration of absorbing aerosols from heavy traffic experienced over the cities of China [Qiu *et. al.,* 2004]. The mean ω was close to the selection value (0.85) that is used in climate simulation [Menon *et. al.,* 2002]. Other studies show a difference in chemical composition of aerosols as reflected *in situ* ω [Cook *et. al.,* 2007]; the lower atmospheric layer had a ω mean value of 0.91 while the elevated atmospheric layer had a higher ω mean value of 0.95. This indicates a stronger scattering component at the elevated atmospheric layer over Adriatic and Black seas during summer 2004. AERONET derived ω at λ=550 nm was in close agreement with the aircraft measurements of 0.85 and 0.87 respectively over Banizoumbou. This shows a

uniform mixture of dust and biomass burning aerosols over different levels in the atmosphere [Johnson *et. al.*, 2009].

Angstrom exponent (α) is a measure of aerosol size and distribution whereby $\alpha \approx 0$ corresponds to coarse aerosol dust particles while $\alpha \approx 2$ corresponds to fine aerosol particles [Dubovik *et. al*., 2002]. The typical values of α range from 1.13-1.4 for continental polluted air mass containing insoluble particles, water soluble particles such as sulfates and nitrate particles and soot [Hess *et. al*., 1998]. Angstrom exponent (α) mean values (670 nm/443 nm) of 1.6 and 1.5 for the first six months of 1997 respectively was retrieved at Thessaloniki, Greece from CIMEL-sun photometer measurements. This was indicative of dominant biomass burning aerosols mixed with soot from diesel engine systems [Perrone *et. al*., 2005]. Angstrom exponent (α) varies from 0.8 to 1.0 computed in the UV-Visible (340-670 nm), and from 0.4 to 0.5 as estimated in the IR (870-2130 nm) spectral ranges. This shows a dominance of aerosol particle species in the 675 to 870 nm spectral range over the study sites [Smirnov *et. al.*, 2003].

Ground-based AERONET mean values of α obtained with a hand held sun photometer [Sabbah *et. al*., 2001] span the range 0.19-0.21 (with standard deviations of 0.08-0.17), for Barbados, Egypt. This suggests the influence of Saharan desert mineral dust loading over the town. In Bamzoumbou, Niger, the corresponding α is less than 0.3 in January and 0.15 in June while in December, it increases to 0.45. This indicates the influence of Saharan desert mineral dust loading over the site. In Mongu, Zambia, α spans the range 1.6-2.0, dominated by biomass burning aerosols while at Lamto, Ivory Coast, α has mean values of 0.84 and 1.42 for aged and fresh smoke respectively [Liousse *et. al*., 1995].

Angstrom exponent (α (440-870 nm)) of the Gulf of Cadiz (Southwest of Spain), obtained using Licor 1800 spectroradiaometer for the period 1996-1999 has a mean value of 0.93±0.58 thereby falling inside the range of marine aerosols [Vergaz *et. al.*, 2005]. At the El Arenosillo AERONET site (Huelva, Spain), the mean α (440-870 nm) was found to be 1.05±0.43; this was a threshold value separating coarse and fine aerosols [Toledano *et. al.*, 2007]. The mean α at Quarzazate (Morocco) during the Saharan Mineral Dust Experiment (SAMUM) (May-June 2006) was 0.35 indicating a mineral dust loading influence from Sahara desert [Toledano *et. al.*,

2009]. The α computed from adjacent wavelength pairs varies from 0.46 for 340-380 nm wavelength pair to 2.31 for 675-870 nm pair for biomass burning aerosols [Eck *et. al.,* 1998]. The frequency distribution of α has two peaks with one around 0.7, characterizing a situation when dust aerosols are more dominant, and the second at 1.2 corresponding to relatively dust-free cases [Smirnov *et. al.,* 2003].

A seasonal evolution of both real (n) and imaginary (k) refractive indices of aerosol particles was found to exist with large n values indicating large scattering coefficients while large k values depict larger absorption coefficients [Ackermann, 1998]. Imaginary part (k) values for biomass burning smoke particles vary from an average value of 1.47 for Amazonian forest region smoke to 1.52 South America Cerrado smoke. Other estimates of the n for biomass burning aerosol range between 1.52-1.55 [Westphal and Toon, 1991; Lenoble, 1991; Li and Mao, 1990]. The lowest k obtained for dust particles is 0.008 which is the value given for the visible spectrum by several models [Shettle and Fenn 1979; WMO 1983]. Comparable, low values of k were also reported to be 0.003 [Levin *et. al*., 1980] and 0.001 [Otterman *et. al*., 1982]. The low k values reported in literature correspond to low absorption coefficients and hence low aerosol particle concentration of absorbing properties. It was also noted that $k \approx 0.007$ in spring-summer and $k \approx 0.002$ in autumn-winter whereas n spans the range 1.40-1.47 and 1.48-1.54 in spring-summer and autumn-winter respectively over south east Italy [Perrone *et. al.,* 2005]. This shows low levels of concentration of aerosols in both summer and spring low concentration of absorbing aerosols in both autumn and winter but elevated concentration of scattering aerosols.

The real part (n) has values ranging from 1.49 to 1.61 while k values range from 0.001 to 0.16 over central Europe and Italy [Hanel, 1994]. It was deduced that k values greatly dependent on the concentration of black carbon (BC) and dust, which are preliminary absorbing aerosols. On the other hand, n values indicated elevated concentrations of sulfates and nitrates dominated aerosols that are known for scattering of radiation in the atmosphere over central Europe and Italy. The average value of the complex refractive index over Beijing was reported to be $n = 1.5$ while was $k = 0.02$ [Li *et. al.,* 2004]. Typical values of refractive indices at λ=550 nm for sea salt

aerosol are 1.50 and 1.0×10^{-8} for n and k indices respectively [Shettle and Fenn, 1979]. Low k values over the site indicated low concentration of absorbing aerosol particles.

Studies for six cities, in China showed that total yearly mean of k during 1993-2001 changed from 0.0207 to 0.0301 indicating a considerable increase in the concentration of absorbing aerosols [Qiu *et. al.*, 2004]. The refractive index at $\lambda = 550$ nm for each species of aerosols are n =1.53, k = 0 for $(NH_4)_2SO_4$ and n = 1.611, k = 0 for NH_4NO_3 with the species being totally scattering aerosols [Weast, 1985]. On the other hand, it was found that n = 1.45, k = 0.001 values correspond to organic carbon [Krekov, 1993] while n = 1.75, k = 0.44 is for black carbon with the later indicating stronger absorption properties than that of organic carbon [WCP, 1986]. The refractive index of n = 1.54, k = 0.045 at 550 nm for biomass burning from aircraft measurements [Johnson *et. al.*, 2008]. This signified a uniform mixture between biomass burning aerosols and mineral dust loading over West Africa. Determination of refractive indices of dust aerosols based on the haematite model was found as n = 1.512 and k = 0.00092 across most of the solar spectrum (300-2000 nm) [Balkanski *et. al.*, 2007]. This is a slight adjustment which suggested refractive indices of n = 1.53, and k = 0.0004 from different flights targeting moderate to strong dust events [Osborne *et. al.*, 2008].

A cloudless atmosphere has an asymmetric factor (g) ranging from 0.1 (in very clean conditions) to 0.75 in polluted ones [Zege *et. al.*, 1991]. At Armilla (Spain) [Alados-Arboleda *et. al.*, 2004], asymmetric factor (g) at λ=368 nm varies from 0.719 to 0.754, with a mean value of 0.740±0.009. g at λ=500 nm presents a broader range of 0.664-0.742, with a mean value of 0.700±0.017. At λ=675 nm, g takes on values between 0.614 and 0.720, with a mean of 0.667±0.029. Variation in this parameter at λ=778 nm is limited to a change between 0.617-0.711, with a mean value of 0.658±0.027. These series of g values are typical of locations with moderate contamination [D'almeida *et. al.*, 1991; Hess *et. al.*, 1998]. g value from air craft measurement at λ=500 nm was found to be 0.69, which compared well with AERONET values of 0.66 and 0.70 for versions 1 and 2 data respectively in Banizoumbou and Niamey, showing moderate pollution by both biomass and dust loading aerosols [Johnson *et. al.*, 2009].

Asymmetric factor (g) values at λ=500 nm range between 0.61-0.75 for North Carolina that is dominated by purely forward scattering aerosols [Yu *et. al*. 2000]. Other studies obtained g values in the range 0.63-0.76 at λ=312 nm at the same site [Wenny *et. al*., 1998]. It was also, for instance reported that g values at λ=300 nm for Pärnu (Estonia), ranging between 0.76-0.80 [Kikas *et. al*., 2001]. This indicated the dominance of forward scattering aerosols over the study site. Analysis by Lacis and Mishchenko (1995) indicate that for aerosols of different chemical compositions, i.e. sulphate particles, marine aerosols and small dust particles, g vary between 0.65 and 0.80. We note a difference between these values with those obtained over Castilla y León (Spain) that had g values at λ=500 nm between 0.45-0.75, depicting a moderate contamination of the atmosphere by aerosol particles [Cachorro *et. al*., 2000].

2.3 Physico-chemical Properties

The physico-chemical properties of aerosols determined in this work are aerosol number densities and chemical composition. Studies by Mönkkönen *et. al*., (2005) also indicated an outdoor 24 hour mean number concentration over Nagpur in India between 1.5×10^5 particles/cm^3 and 2.8×10^5 particles/cm^3. It was noted that the number concentration of aerosol particles was sensitive to changes in temperature and humidity. Aerosol particles in the size range 0.3-0.5μm were determined in the evening over Roorkee, India, nine meters above sea level [Sharma *et. al.,* 2003]. It was noted that aerosol concentration varies from about 4×10^4 to 2×10^5 particles/litre in the month of April; with most particles remaining under the upper size range of 10^5 particles/litre, obtained using passive remote sensing. An average number concentration of aerosol particles in (λ=3-500 nm) over Pittsburgh, Russia, is 22000 cm^{-3} having an average mode size of 40 nm, obtained using two scanning mobility particle size systems (TSI 3936L10 and TSI3936N25) [Stanier *et. al.,* 2004]. Other studies done elsewhere in Finland and Estonia [Kikas *et. al.,* 1996] and England [Harison *et. al.*, 1999] reveal a 24 hour average number concentration (λ=10-500 nm) at continental sites that range from 5000-25000 particles/cm^3.

The total aerosol number density in winter (as measured by aerosol particle counter) over Kharagpur, India, varied in the range 2.3×10^8 - 3.5×10^9 m^{-3} with consistent systematic diurnal pattern [Nair *et. al.,* 2009]. It was noted that during hazy period, the concentration of submicron

particles is higher as compared to the non-hazy period which was attributed to enhanced anthropogenic aerosol concentration. Studies over three sites in Finland indicate aerosol number densities range between 2000-17000 cm^{-3} [Laakso *et. al.*, 2003]. It was also noted from the same study that aerosol number density was high in summer and lowest in winter thus depicting seasonal variation.

The chemical characteristics of aerosol particles are determined by anthropogenic activities dominating the site of study, mode of aerosol formation and geographical origin of the dominant aerosol particles. Studies on chemical nature of aerosol particles as collected over the tropical northern Atlantic Ocean during the month of April 1996 onboard the R/V Seward Johnson indicated that mineral dust of a typical shale composition and Saharan origin while Calcite accounted for 3.0 % and 7.9 % of the mineral aerosol during the first and second halves of the cruise, respectively [Johansen *et. al.*, 2000]. It was also reported that ambient aerosol samples collected from Mangalore region in the southwest coast of India shows an abundance pattern that is dominated by HCO_3^-, SO_4^{2-}, Na^+, Cl^-, with minor contribution from NO_3^-, Ca^{2+}, NH_4^+, K^+ and Mg^{2+}, indicating contribution from not only sea salt, but also from anthropogenic and dust sources; with pronounced seasonal variability [Hedge *et. al.*, 2007].

Weekday and weekend ambient aerosol samples over the city centre of Cairo, Ramsis, were collected during the summer season (2006) and analyzed for water-soluble ionic species as reported by Khoder and Hassan (2008). The average concentrations of the total suspended particulate matter (TSP) and their water-soluble components were higher during weekdays than on weekends. This indicated that a decreased traffic density on weekends leads to a decrease in the levels of the TSP and their water-soluble ionic species. The average concentrations of the TSP were 454 μg m^{-3} on weekdays and 298 μg m^{-3} on weekends. The weekday/weekend concentration ratios were 1.52 for TSP, 1.27 for SO^{2-}_4, 1.64 for Cl^-, 1.54 for NO^-_3, 1.17 for NH^+_4, 1.67 for Ca^{2+}, 1.83 for Na^+, 1.75 for K^+ and 1.73 for Mg^{2+}.

2.4 Radiative Forcing Effects

Radiative forcing is the change in the net radiation either at the top of the atmosphere or Earth's surface due to secular variations in the concentrations of radiative active species e.g. aerosols. Impact of aerosols on climate depends on the radiative impacts of aerosols. The annual mean direct radiative forcing for five distinct aerosols is given in the Table 2.2 below.

Table 2.2: Annual mean direct radiative forcing [Source: IPCC, 2001].

Aerosol species	Mean Radiative Forcing (W/m^2)	Range (W/m^2)
Sulfates	-0.40	-0.20 to -0.80
Biomass Burning	-0.20	-0.70 to -0.60
Fossil fuel Organic Carbon	-0.10	-0.03 to -0.30
Fossil fuel Black Carbon	+0.20	+0.10 to +0.40
Mineral dust	_	-0.60 to +0.40

The indirect effects of aerosols have implications through the clouds. For a constant liquid content, an enhancement in the cloud droplet number (by aerosols acting as Cloud Condensation Nuclei (CCN)) leads to an increase in cloud albedo. This is the first indirect effect, which is also known as Twomey effect [Twomey, 1991]. The global mean radiative forcing due to first indirect effect ranges from 0 to -2 W/m^2 [IPCC, 2001]. On the other hand, the total aerosol radiative forcing as derived from models and observations is estimated to be -0.5 [±0.4] W/m^2 while radiative forcing due to the cloud albedo effect in the context of liquid water and clouds is estimated to be -0.7 [-1.1, +0.4] W/m^2 [IPCC, 2007]. The chemical compositions of aerosol particles determine whether they are positive or negative radiative forcing agents. The TSI at the Earth's orbit can be calculated knowing the sun's radius in astronomical units and photospheric temperature; it is approximately 1367 W/m^2 with satellite observations indicating an average value of 1367±4 W/m^2.

The atmosphere is found to be heated by aerosols as much as 25 W/m^2 with highest values over areas characterized by strong absorbing mineral particles and high surface albedo (e.g. Sahara)

[Hatzianastassiou *et. al.,* 2004]. The downward solar radiation at the surface is drastically reduced due to the presence of aerosols by up to 30 W/m^2 [Hatzianastassiou *et. al*., 2004], the largest decrease is found over regions with high τ values. An increase in relative humidity increases the outgoing solar radiation over oceans through increased aerosol scattering from about 1 W/m^2 to 2 W/m^2 [Hatzianastassiou *et. al.*, 2004].

For sulfate aerosols, most of the recent estimates yield a cooling below 0.5 W/m^2 on a global scale due to the scattering of the incoming solar radiation [Haywood *et. al*., 1997]. It is also estimated that a warming of about 0.2 W/m^2 results from a mixture of both sulfates and soot aerosols [Hansen *et. al.,* 1997; Haywood *et. al.,* 1997]. The radiative forcing due to sulfate aerosols is -0.32 W/m^2 while that of fossil fuel soot aerosols is 0.16 W/m^2 [Myhre *et. al.,* 1998]. Calculated radiative forcing due to external (aerosol particles having two or more dissimilar particles chemically) and internal (aerosol particles containing chemically similar particles) mixture of sulfate and soot aerosols amounts to about -0.18 W/m^2 and -0.02 W/m^2 respectively [Haywood *et. al*., 1997]. On the other hand, radiative forcing due to mixture of sulfate and soot as an external mixture was estimated as -0.16 W/m^2 while an internal mixture for the same amounted to 0.10 W/m^2 [Myhre *et. al.,* 1998]. Radiative transfer modeling suggested a 130-160 W/m^2 instantaneous reduction of downwelling solar radiation by aerosol columns (15-18 % of the total flux) [Johnson *et. al.,* 2009].

The role of atmospheric aerosol particles be it direct or indirect is viable in understanding their influence on climate. There is a need in improving the knowledge of aerosol effects which advances the development of both analytical and computational methodological techniques that furnish data and information for climate forecasting, ambient air quality, regulatory environmetrics and human health studies over the region of study. These studies can be accomplished by aid of aerosol optical properties derived from either active or passive remote sensing techniques and are known to vary with meteorological parameters. The multivariate nature of these aerosol optical properties can be studied using appropriate chemometric techniques so as to help in understanding the regions patterns of climate change among other aerosol influences.

CHAPTER 3

THEORETICAL BACKGROUND

3.0 Introduction

Atmospheric aerosols affect the incoming solar radiation through scattering and absorption. When small in their size, aerosols act as cloud condensation nuclei thus perturbing the radiation budget and also influencing visibility of the Earth-atmosphere system. They also act as sites of chemical reactions, which heavily depends on their size. Aerosol properties are highly inhomogeneous both in space and time since they are produced and subjected to various atmospheric processes such as coagulation, condensation and cloud cycling. Their physico-chemical properties (surface, shape, size, size distribution, altitude distribution and chemical composition) show large variations globally.

3.1 Classification of Aerosols

Atmospheric aerosols can be classified geographically into maritime, continental and background aerosols. They can also be classified based on particle radius into Aitken (0.001-0.1 μm) which act as Cloud Condensation Nuclei (CCN) that aid in the formation of various types of clouds, large (0.1-1 μm), and giant (> 1 μm) particles. Since production mechanisms and particle radius yield different modes to particle size distributions, aerosols can also be classified into nucleation mode (ultrafine) (0.001-0.1 μm), accumulation mode (fine) (0.1-1 μm), and coarse mode (> 1 μm) [Whitby, 1978]. Nucleation mode is as a result of low volatile gas-phase reaction products; accumulation mode is by coagulation and condensation processes, while the coarse mode is by mechanical processes. Aerosols in the nucleation mode are important in regulating atmospheric conductivity and cloud formation while those in the accumulation mode take part in the formation of fog and mist, thus affecting visibility and interaction with solar radiation. The coarse mode aerosols primarily affect cloud microphysics.

3.2 Atmospheric Chemistry

The Earth's atmosphere is vertically stratified according to temperature profile, with the troposphere and stratosphere closest to the surface respectively. The troposphere (varies up to 15 km at the equator) while the stratosphere (varies from about10 km to 50 km). Trace species concentrations in these strata are determined by different sources and sinks with their interactions with both the biosphere and hydrosphere playing a key role. They can be released naturally through biological emissions from organisms, biomass burning and volcanoes or as a result of burning fossil fuels, agriculture and also through photochemical reactions from other trace gases. Their elimination is partly through chemical reactions, wet removal, dry deposition and assimilation into organisms.

3.2.1 Sources and Role of Tropospheric Ozone

Tropospheric ozone has two sources namely stratospheric-tropospheric exchange (STE) where ozone is formed in the stratosphere through photolysis from oxygen (O_2) then transported to the troposphere. Photolysis of O_2 is only possible in the stratosphere since it requires short wave radiation ($\lambda \leq 242$ nm) which is effectively absorbed in the stratosphere by ozone. Secondly, the reaction of O_2 and O, where atomic oxygen results from photolysis of NO_2:

$$NO_2 + h\upsilon \rightarrow NO + O \qquad (3.1a)$$

$$O + O_2 + M \rightarrow O_3 + M \qquad (3.1b)$$

with the absorbed radiation being of wavelength ($\lambda \leq 420$ nm) and M representing another molecule carrying away excess energy. Ozone plays an important role in the chemistry of the atmosphere through other processes involving NO_x i.e. NO and NO_2, carbon monoxide (CO), hydrocarbons (HCs) and Non Methane Hydrocarbons (NMHCs) in combination with hydroxyl radical (OH) in the presence of photon energy from sunlight ($h\upsilon$). The major oxidant behind many atmospheric reactions is the hydroxyl radical (OH), which is formed from O_3 during day time through photolysis. A discussion of more complex processes governing ozone concentrations in both troposphere and stratosphere may be found elsewhere [Brimblecombe, 1996].

The rise in tropospheric ozone and greenhouse gas concentrations especially in urban and industrial regions is a direct result of increased emissions of its precursors from anthropogenic sources e.g. fossil fuel burning in traffic, industrial emissions and biomass burning. Emissions of primary pollutants (SO_2, NO_x and CO_x) are not sufficiently ventilated in the absence of wind. Strong solar radiation not only leads to photochemical formation of secondary pollutants (most prominent O_3) but it also accelerates dust loading that absorbs most of the incoming and terrestrial solar radiation from the Earth's surface.

3.3 Aerosol Size Distribution

The size distribution of aerosols $n_c(r)$ can be expressed in terms of columns as [Alados-Arboleda *et. al*., 2003].

$$n_c(r) = \frac{\partial N_c}{\partial \log(r)} \tag{3.2}$$

where $n_c(r)$ is the columnar size distribution (number of aerosol particles per unit area per unit log-radius interval in a given vertical column through the atmosphere), N_c is the columnar particle number density and r is the aerosol particle radius. Aerosol scattering equation 3.3 expresses the dependence of spectral variation of aerosol optical depth (τ) on the aerosol size distribution:

$$\tau(\lambda) = \int_{r_a}^{r_b} \pi r^2 Q_{Ext}(r, \lambda, m) n_c(r) dr \tag{3.3}$$

where $Q_{Ext}(r, \lambda, m)$ is the Mie extinction efficiency parameter, which is a function of particle radius r, wavelength λ and complex refractive index m. The lower and upper limits of integration, r_a and r_b are defined by considering the size of particles that contribute significantly to the integrant of the above equation and their values always depend on the interval of λ from the available aerosol optical depth $\tau(\lambda)$. $Q_{Ext}(r, \lambda, m)$ is an asset in obtaining both the scattering and absorption characteristics of aerosols as demonstrated by Bolle (1977) in equation (3.4) below:

$$\delta_e = Q_{Ext}(r, \lambda, m) \frac{\pi d^2}{4} \tag{3.4}$$

δ_e : extinction cross-section.

d: diameter of the aerosol particles.

the relationship of δ_e with τ can be taken as:

$$\tau = N\,\delta_e \qquad (3.5)$$

where N is the aerosol number density.

3.4. Principle of Sun Photometry

3.4.1 Introduction

The principle of measuring direct solar irradiance by sun photometer is demonstrated in Figure 3.1. This principle depends on the wavelength of sunlight absorbed and scattered along a given path through the atmosphere. Measured spectrophotometric voltage signal V at the ground to the undisturbed (entry solar radiated) signal V_o at the top of the atmosphere gives information of τ by help of Beer-Lambert-Bouguer law (equation 3.7).

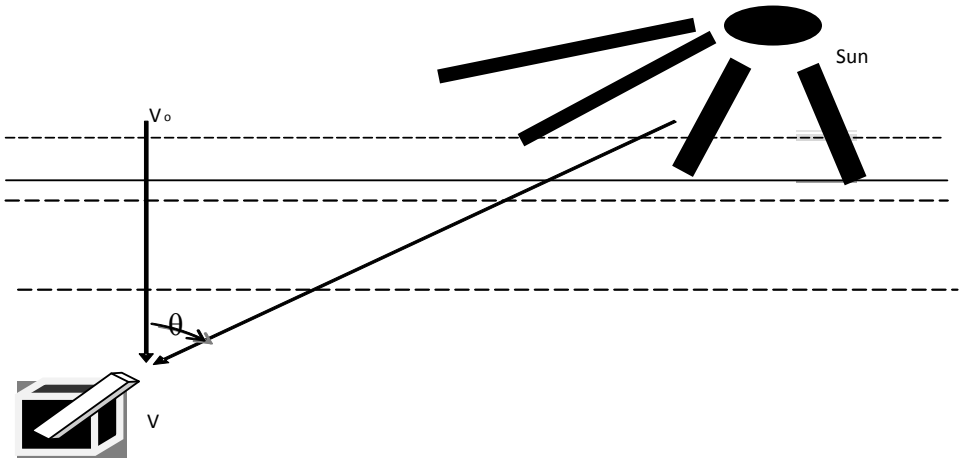

Figure 3.1: Principle of sun photometry.

3.4.2 Detailed Description of the Cimel Sun-photometer

3.4.2.1 List of Components

The Cimel sun-photometer (CSPHOT) consists of (1) the instrument itself (made up of the sensor head and scanning motors and robot arm); (2) a control box (provides software for controlling predetermined scanning and sampling strategies, for acquiring data, and for formatting remote satellite-based transmissions and batteries); and (3) a radio antenna (for transmitting data to a GOES satellite). The instrument is made by Cimel Electronique of France; the GOES transmitter module (GTM) and antenna are made by Vitel Corporation (USA)(Figure 3.2).

3.4.2.2 System Configuration and Measurement Methods

The instrument consists of the main stem containing the azimuth motor, on the top of the motor is attached a robot arm consisting of the zenith motor on one side and the sensor head on the other side. The collimators are attached to the sensor head. Inside the sensor head are two silicon detectors, one for each of the collimators. A filter wheel is placed in between the collimator windows and the detectors, inside the sensor head. The wheel consists of eight narrowband interference filters (at 340 nm, 378 nm, 440 nm, 499 nm, 613 nm, 870 nm, 940 nm and 1020 nm) mounted along the circumference. The two collimators have the same field of view (1.2^0) but differ in the size of apertures. They are physically part of a single unit that is attached to the sensor head by a long screw tightened down to prevent light and water leakage. The larger aperture collimator, 10 times as large as the sun-viewing collimator provides the necessary dynamic range to observe the sky. Three cables (a thick cable from the sensor head to the control box, and two battery power cables, one each to the motors) are attached to the instrument. The main stem is connected to a base plate consisting of mounting holes to ensure the instrument is mounted on a level surface. A schematic diagram of CSPHOT system and mounting configuration together with instruments parts are outlined in Figure 3.2a and b.

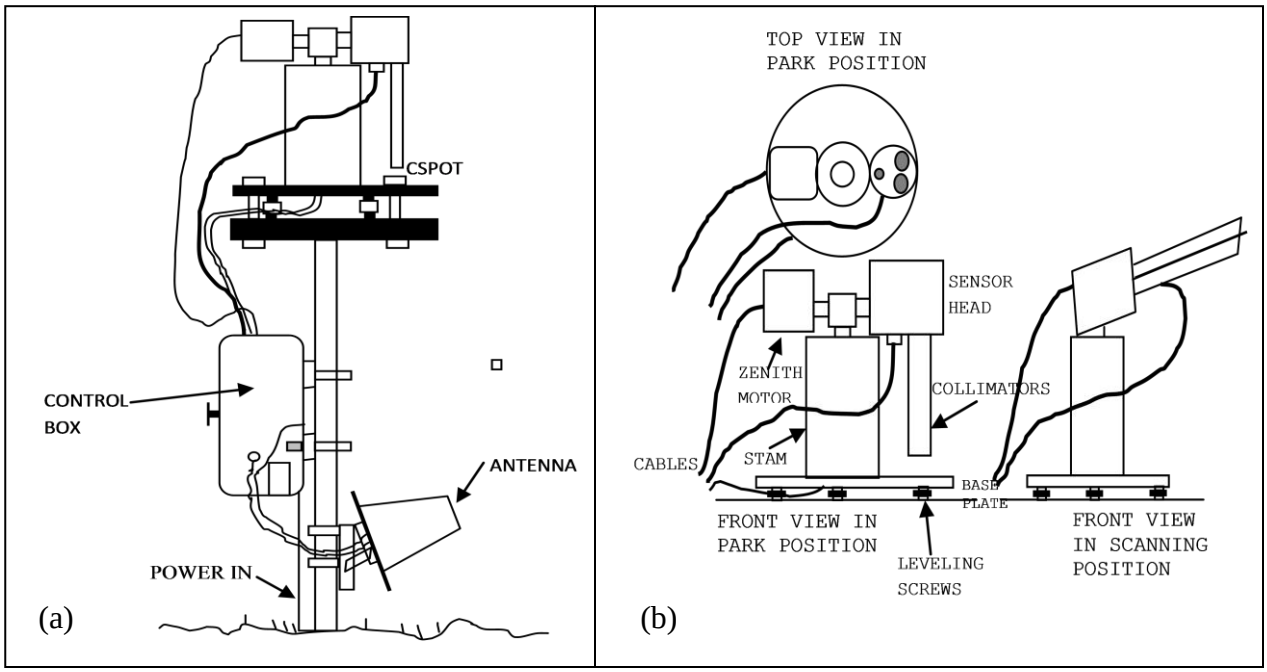

Figure 3.2: (a) Schematic diagram of CSPHOT system and mounting configuration and (b) instruments parts and operation.

3.4.2.3 Control Boxes

The Cimel control box consists of a control module, a rectangular shaped white box that actually controls the scan and measurement sequence of CSPHOT. It has an internal battery that services only the software portion of the instrument. The box also stores data that can be queried and transferred upon demand by the GOES Transmission Module (GTM). The GTM is housed in the control box and physically consists of two parts: the GTM control box that schedules and formats data for transmission, and an amplifier box that boosts the signal for transmittal through the antenna. The control box also includes a battery pack that supplies power to the CSPHOT control box and the GTM. A separate battery charger provides the necessary power from the input mains.

3.4.2.4 Antenna

The antenna is connected to the GTM amplifier through a 6-foot, heavy-duty coaxial cable. The antenna points South-South-East at the site to enable transmission to the GOES east satellite. The antenna transmits data every hour at a predetermined time and takes up to a maximum of 2 minutes at a transmission frequency of 401.76 MHz. The password code and duration and time of transmission are all set in the GTM control box.

3.4.2.5 Location (Siting)

The instrument is located at a height of about 5 feet from the surface to minimize accidental obstruction of the field of view of the collimators. The location allows an unobstructed view of the sky above 5^0 of elevation, especially in the general region of sunset and sunrise at the site. All the cables interconnecting the above components pass through rainproof silicone seals in their respective boxes. A wet sensor, connected to the instrument control box, effectively shuts down the scanning by the sensor head during precipitation. The fail safe pointing for the sensor head is the "down" position with the collimators pointing down toward the base.

3.5. Calibration of Sun-photometer with the Langley Method

In the Langley calibration method, a sequence of measurements are taken with the sun photometer for several hours while the solar zenith angle (SZA) or the optical air mass (M) is either decreasing (morning) or increasing (afternoon) continuously. τ should approximately remain constant throughout each measurement session (morning or afternoon). Thus, the Langley calibrations are done at high altitude locations. This calibration method is based on the principle of linear relationships produced from logarithmic transformation of equation 3.6. Taking the natural logarithm of both sides of equation 3.7, one obtains:

$$\ln(V_\lambda) = \ln(V_{o\lambda} D^{-2}) - \tau_\lambda M \qquad (3.6)$$

Equation 3.6 is a linear equation with the slope $-\tau_\lambda$ and intercept $\ln\left(V_{o\lambda}D^{-2}\right)$ whose parameters are as defined in equation 3.7 and D is the earth-sun distance in astronomical units. To generate Langley plots for each wavelength λ, using the data acquired during each measurement session, $\ln(V_\lambda)$ is plotted against M. Based on equation 3.6, a linear least squares fit to the straight part of the Langley plot for each wavelength λ produces the ordinate intercept $\ln\left(V_{o\lambda}D^{-2}\right)$ from whose exponential the calibration coefficient $V_{o\lambda}$ is evaluated [Ichoku *et. al*., 2002].

3.6. Instrumentation (Sun Photometer)

AERONET sun photometer measures direct solar irradiance by pointing the collimator towards the approximate position of the sun (provided it is aligned properly), this is done at eight channels with peak wavelength (λ) of 340 nm, 380 nm, 440 nm, 500 nm, 675 nm, 870 nm, 940 nm and 1020 nm in which direct sun measurements with a 1.2^o full field of view are made every 15 minutes. Direct sun measurements take 8s to scan the entire 8 wavelengths, with a motor driven filter wheel positioning each filter in front of the detector. The solar extinction measurements are then used to compute the aerosol optical depth (τ) at each wavelength except for 940 nm channel, which is used for retrieving precipitable water. The τ is derived based on the Beer-Lambert-Bouguer law:

$$V_\lambda = V_{O\lambda} D^{-2} \exp(-\tau_\lambda M) \qquad (3.7)$$

where for each channel (wavelength)

V_λ- The signal measured by the instrument at a wavelength λ.

$V_{O\lambda}$ – The extraterrestrial signal at wavelength λ.

D– Earth-Sun distance in astronomical units at the time of the observation.

M – The optical air mass.

τ_λ – Total optical depth at a particular wavelength ($\tau_\lambda = \tau_{a\lambda} + \tau_{R\lambda} + \tau_{o3\lambda}$).

$\tau_{a\lambda}$ – Aerosol optical depth at a wavelength λ.

$\tau_{R\lambda}$ - Rayleigh (air) optical depth at a wavelength λ.

$\tau_{o3\lambda}$ – Ozone optical depth at a wavelength λ.

The filters used in this instrument are ion-assisted deposition interference filters with band pass (full width at half maximum) of the 340 nm channel at 2 nm and the 380 nm filter at 4 nm, while the band pass of all the other channels is 10 nm. Since there exists a nonlinear contribution from water vapor in the channel 940 nm the equivalent equation for this channel is given by [Reagan *et. al*., 1986]:

$$V_W = V_{OW} D^{-2} \exp(-\tau_W M - h(WM)^b) \quad (3.8)$$

where V_W, V_{OW}, D, τ_W and M remain as defined in equation (3.7), except the subscript W is used to show that 940 nm is the water vapor absorption channel with h and b being the constants to be derived from the 940 nm filter. The Raleigh and ozone optical thickness, $\tau_{R\lambda}$ and $\tau_{o3\lambda}$ may be obtained from atmospheric models [Ichoku *et. al*., 2002].

3.7. Aerosol Optical Properties

Solar radiation incident on the Earth's surface undergoes reflection, refraction, absorption and scattering. Scattering involves a particle in the path of radiation absorbing and re–radiating the same radiation in all directions. On the hand, absorption involves transfer of radiation energy to the molecules of the aerosol particles, thus increasing their internal energy and causing heating of the particle and eventually the surrounding medium; the sum of scattering and absorption gives an estimate of extinction.

For problems involving radiative interaction of atmospheric aerosols, solutions of the radiative transfer equation are required. This calls for understanding several aerosol parameters associated with radiative interaction of aerosols such as extinction cross section and aerosol optical properties viz. aerosol optical depth (τ), single scattering albedo (ω), angstrom exponent (α), asymmetric factor (g), complex refractive index including both real (n) and imaginary (k) parts. These optical properties change depending on whether the aerosols are externally or internally mixed. Some of optical properties are described below.

3.7.1 Aerosol Optical Depth (τ)

Aerosol optical depth (τ) is the fraction of solar radiation that is not scattered or absorbed on its path in the atmosphere and is a measure of atmospheric turbidity. The spectral dependence of aerosol optical thickness in the visible region is often approximated by a power law relation [Angstrom, 1964].

$$\tau(\lambda) = \tau(\lambda o) \left(\frac{\lambda}{\lambda_o} \right) \exp(-\alpha) \qquad (3.9)$$

where τ, λ, and λ_o are aerosol optical depth and the two sets of wavelength channels necessary to obtain angstrom exponent (α) that reveals the optical state of the atmosphere.

3.7.2 Single Scattering Albedo (ω)

The ratio of scattering to extinction optical depths is called single scattering albedo (ω). It is given as

$$\omega = \frac{\tau_{sca}}{\tau_{ext}} = \left[\frac{\tau_{sca}}{\tau_{sca} + \tau_{abs}} \right] \approx 1 - \left[\frac{\tau_{abs}}{\tau_{ext}} \right] \qquad (3.10)$$

where τ_{sca}, τ_{abs}, τ_{ext} are the scattering, absorption and extinction aerosol optical depth. Typically, ω varies from 0-1 with 0 corresponding to a perfectly absorbing aerosol while 1 corresponds to a pure scattering aerosol. A change in ω from 0.9-0.8 of the underlying surface and latitude of the aerosols can change the sign of direct effect [Hansen *et. al.,* 1997]. For sulfate dominated aerosols, $\omega \approx 1$, thus, they act as scatterers of solar radiation leading to net cooling of the earth surface. For soot, ω is very small ≈ 0.2, and hence a large amount of radiation is absorbed leading to local heating. In general, aerosols exist as a mixture of absorbing and non-absorbing material and hence ω lies between 0.8 (extremely polluted) and 1 in the case of pure scattering aerosols.

3.7.3 Angstrom Exponent (α)

Angstrom exponent (α) is determined from the spectral dependence of the measured τ. It constitutes a good indicator of aerosol size and its variations [Angstrom, 1929]. Angstrom exponent (α) can also be determined empirically according to:

$$\tau = \beta\lambda^{-\alpha} \tag{3.11}$$

where λ is the wavelength in microns corresponding to τ values and β is the Angstrom's turbidity coefficient which equals to τ at λ=1 μm. This parameter can also be obtained by rearranging equation 3.9 above to obtain:

$$\alpha = -\frac{\ln\left(\frac{\tau(\lambda)}{\tau(\lambda_o)}\right)}{\ln\left(\frac{\lambda}{\lambda_o}\right)} \tag{3.12}$$

3.7.4 Asymmetric Factor (g)

The asymmetric factor (g) describes the shape of the phase function. It can be used to characterize the phase function independent of scattering angle. It is given by the first moment of the phase function and is the average of the cosine of the scattering angle for scattered radiation, given by,

$$g(\lambda) = \frac{\int \cos\theta p(\theta) d(\cos\theta)}{\int p(\theta) d(\cos\theta)} \tag{3.13}$$

where θ is the scattering angle, $p(\theta)$ is the phase function and $g(\lambda)$ is a measure of deviation of the scatterer from being isotropic; it describes how much forward/backward scattering dominates. Theoretically $g(\lambda)$ can vary between -1 and +1. For particles with isotropic scattering properties e.g. Rayleigh scatterer, the average intensity in the forward and backward direction are equal and hence $g(\lambda) = 0$. When more solar radiation is scattered in the forward direction $g(\lambda) > 1$ and for a pure backscattering $g(\lambda) = -1$. For the symmetric nature of cloudless atmosphere,

$g(\lambda)$ ranges between 0.1 (for very clean) and 0.75 (for polluted) atmospheres. Cloudy atmospheres have $g(\lambda)$ values between 0.8-0.9 [Zege *et. al.,* 1991]. The relationship connecting the asymmetric factor and phase function is given by

$$p(\theta) = \frac{1 - [g(\lambda)]^2}{\left[1 + [g(\lambda)]^2 - 2g(\lambda)\cos\theta\right]^{\frac{3}{2}}} \tag{3.14}$$

3.7.5 Complex Refractive Index

The refractive index m, of aerosols is an important parameter influencing their radiative effects [D'almeida *et. al*., 1991]. It is primarily determined by the chemical composition of the aerosol and hence it exhibits large spatial and temporal variations. It is wavelength-dependent and generally is a complex number expressed as,

$$m = n - ik \tag{3.15}$$

where n is the real part and k is the imaginary part. The real part determines the scattering properties and the imaginary part determines the absorption characteristics.

3.8 Multivariate Chemometric Techniques

Chemometrics is an interdisciplinary field that involves the use of mathematical models, statistical principles and other logic-based methods to design or select optimal measurement procedures and experiments. The complex nature of the environment as a result of the inherent variability, correlations as well as latent patterns among measured data limits the understanding of the atmospheric distribution of aerosols as obtained from univariate analysis. Because of this, multivariate techniques are necessary since they are capable of handling a group of variables simultaneously. They are also capable of capturing information about correlated trends in a given data. Further more; applying univariate tests repeatedly increases the likelihood of an observation occurring by chance (the false-positive result). Many multivariate chemometric techniques exist for performing environmental analysis and other logic-based decisions. In this work, Principal Component Analysis (PCA), Partial Least Squares Discriminant Analysis (PLS-

DA), Principal Component Regression (PCR) and Hierarchical Cluster Analysis (HCA) were used in order to study the temporal and spatial characteristics, correlations and patterns in the aerosol optical properties.

3.8.1 Principal Component Analysis (PCA)

PCA refers to a method of data analysis for building linear multivariate models of complex data sets. The linear multivariate PCA models are developed using orthogonal basis vectors (eigenvectors) usually called the Principle Components (PC). PCA aims at reducing the dimensionality of complex problems and minimizing the effects of measurement error. It is possible to build an empirical mathematical model of data as described in the equation below where T_k is a $n\,x\,k$ matrix of Principle Component scores and V_k is the $m\,x\,k$ matrix of eigenvectors.

$$A = T_k \; V_k^T + \varepsilon \tag{3.16}$$

The eigenvectors in V_k can be used to form a set of orthonormal raw basis vectors for A. The eigenvectors are also called loadings and ε is the residual. The columns of T_k are called scores and are mutually orthogonal but not normalized. They can be used to form a set of column basis vector of A. For each independent source of variation in the data, a single PC (eigenvector) is expected in the model. The first PC explains as much as possible of the total variance of the data in matrix A. The second component explains as much as possible of the remaining variance and so on [Hedwig *et. al.*, 1990]. The schematic diagram of equation 3.16 is given as:

$$\begin{bmatrix} \ldots & \ldots & \ldots & \ldots & \ldots \\ \ldots & \ldots & \ldots & \ldots & \ldots \\ \ldots & \ldots & A & \ldots & \ldots \\ \ldots & \ldots & \ldots & \ldots & \ldots \\ \ldots & \ldots & \ldots & \ldots & \ldots \end{bmatrix} = \begin{bmatrix} \ldots \\ \ldots \\ \ldots \\ T_k \\ \ldots \\ \ldots \\ \ldots \end{bmatrix} \begin{bmatrix} \ldots & \ldots & \ldots & \ldots & \ldots & \ldots & \ldots & \ldots & \ldots \\ \ldots & \ldots & \ldots & V_k^T & \ldots & \ldots & \ldots & \ldots & \ldots \\ \ldots & \ldots & \ldots & \ldots & \ldots & \ldots & \ldots & \ldots & \ldots \end{bmatrix}$$

3.8.2 Partial Least Squares Discriminant Analysis (PLS-DA)

Partial Least Squares (PLS) is a regression tool that is able to project latent variables that represent useful information contained in the original data. Relations between the input and response variables are then developed by means of regression between the latent variables, where linear, nonlinear, or even artificial intelligence techniques such as neural networks can be applied. The algorithm assumes that the available data are grouped in two matrices X and Y of dimension $(k \times m)$, $(k \times r)$ respectively, where k is the number of samples, m is the number of input variables, and r is the number of output variables. The decomposition of input and output data matrices X and Y into bilinear terms takes place following equation 3.17a and b.

$$X = \sum_{i=1}^{a} t_i p_i^T + E \quad (3.17a)$$

$$Y = \sum_{i=1}^{a} u_i \, q_i^T + F \quad (3.17b)$$

where t_i and u_i are input and output scores respectively, p_i and q_i are the loading vectors while E and F are the matrix residuals. PLS-DA finds its basics in PLS that is fully described by Alexandridis *et. al.* (2004). The principle of PLS-DA is fairly simple i.e. for each class, we have:

$$\hat{c} = T.q \quad (3.17c)$$

where T are the PLS-scores obtained from the original data, q is the length equaling the number of significant PLS components and ĉ is a class membership function obtained by PLS regression from the original vector A whose elements have values of 1 for members and 0 otherwise.

3.8.3 Principal Component Regression (PCR)

PCR is typically used for linear regression models where the number of independent variables p is very large or where the regressors are highly correlated. This model can be extended to the case where we have more than one response variable in which p-variate predictors $x_i = (x_{i1}, \ldots . . x_{ip})^T$ and q-variate responses $y_i = (y_{i1}, \ldots \ldots y_{iq})^T$ are same. The multivariate (multiple) regression model is given by

$$y_i = \beta_0 + B^T x_i + \varepsilon_i \quad (3.18)$$

where B is the $p \times q$ slope matrix, β_0 is the q-dimensional intercept vector. ε_i is the error that is assumed to be independent and identically distributed with zero mean and constant variance [Gemperline, 2006].

3.8.4 Hierarchical Cluster Analysis (HCA)

Exploratory data analysis techniques are often quite helpful in elucidating the complex nature of multivariate relationships. The HCA method attempts to find sample groupings or clusters within data using criteria developed from the data itself hence the term cluster analysis. It is based on the principle that distances between pairs of points in the measurement space are inversely related to their degree of similarity as shown in equation 3.19.

$$S_{ik} = 1 - \frac{d_{ik}}{d_{max}} \quad (3.19)$$

where S_{ik} is the measure of similarity between samples i and k, d_{ik} is the distance between samples i and k and d_{max} is the distance between the most dissimilar samples which is also the largest distance in the data set [Hedwig *et. al.*, 1990].

3.9 Radiative Characteristics of Aerosols

Selected aerosol radiative characteristics namely spectral irradiance, integrated fluxes (total spectral irradiance, TSI) and reflectance were considered in this work as discussed in the following subsections. Spectral irradiance $E_o(z, \lambda)$, is the radiant energy flux per unit time in a given wavelength interval. The irradiance is obtained by integrating the radiance, which is the radiative power per unit solid angle in a particular direction, weighted with the cosine of the viewing zenith angle, $\mu = cos\theta$ over all viewing directions in the hemisphere of 2π steradians. Spectral irradiance is a function of wavelength with the units $Wm^{-2}nm^{-1}$; its integration corresponds to the solar integrated fluxes (TSI or global irradiance) over the entire spectrum arriving at the top the terrestrial atmosphere with units Wm^{-2}. The change in solar activity of the

atmosphere causes a variation in the TSI which is related to the spectral irradiance ($E_o(z,\lambda)$) as shown in the equation below:

$$TSI = \int_0^\infty E_o(z,\lambda)d\lambda dz \quad (3.20)$$

where z and λ represent the height and wavelength respectively while the limits of integration can take on any desired wavelength range.

3.10 Radiative Transfer Modeling

3.10.1 Brief Description of the COART model

Coupled Discrete Ordinate Radiative Transfer (CDISORT) is used as a solver of the radiative transfer problem by COART model (http://www.cave.larc.nasa.gov/cave/). CDISORT accounts for the change in refractive index at the layers interface. COART considers the atmosphere and ocean as one coupled system and treats the ocean strata just as additional atmospheric layers with different optical properties. Similar to the atmosphere, the ocean can also be subdivided into an arbitrary number of layers required to resolve the vertical variations of water properties. COART models the absorption and scattering process in the atmosphere and ocean explicitly. This includes the scattering and absorption by molecules, aerosols and clouds in the atmosphere (but with the latter ignored in this work) and by liquid water molecules, dissolved and particulate matter in the ocean.

COART calculates radiances and irradiances at any level of the atmosphere and ocean in both narrowband and broadband schemes. For the narrowband spectra scheme, users can specify both the band (wavelength) limits and computational resolution arbitrarily. In this scheme, COART employs the LOWTRAN 7 band model (spectral resolution of 20 cm^{-1}) and the molecular absorption database for the atmosphere. This corresponds to a wavelength resolution of approximately 0.5 nm at 500 nm and 8 nm at 2000 nm. For efficient broadband calculations of radiance and irradiance, COART divides the solar spectrum (0.2-4.0 μm) into 26 fixed wavelength intervals; in each spectral interval, the k-distribution technique parameterizes molecular absorption in the atmosphere using the HITRAN 2000 database [Kato *et. al.,* 1999]. In

this work it was assumed that the depth into the ocean is zero so as to let COART be used for the atmosphere–land system hence all parameters in the equations that seem to be relevant only in the case of an ocean are all ignored by COART so as to assume an atmosphere-land system with the land being flat.

3.10.2 Radiative Transfer Equation (RTE)

The basic equation describing the radiative field through a plane-parallel medium is given by [Zhonghai *et. al.*, 1994; Zhonghai *et. al.*, 2006].

$$\mu \frac{dI(\tau,\mu,\Phi)}{d\tau} = I(\tau,\mu,\Phi) - S(\tau,\mu,\Phi) \quad (3.21)$$

where $I(\tau,\mu,\Phi)$ is the specific intensity (radiance) at a vertical optical depth τ (measured downward from the upper boundary) in the direction (μ,Φ) (μ is the cosine of the polar angle which is positive to the upward normal and Φ is the azimuthal angle). The source function $S(\tau,\mu,\Phi)$ is

$$S(\tau,\mu,\Phi) = \frac{\omega(\tau)}{4\pi}\int_0^{2\pi} d\Phi' \int_{-1}^{1} P(\tau,\mu,\Phi,\mu',\Phi')I(\tau,\mu',\Phi')d\mu' + Q(\tau,\mu,\Phi) \quad (3.22)$$

where $\omega(\tau)$ is the scattering albedo, $P(\tau,\mu,\Phi,\mu',\Phi')$ is the phase function and $Q(\tau,\mu,\Phi)$ represents the actual internal source. Both μ' and Φ' are the cosine of the polar angle and azimuthal angle of subsequent scattered or absorbed solar radiation. The solar beam source in the atmosphere can be expressed as

$$Q_{air}(\tau,\mu,\Phi) = \frac{\omega(\tau)}{4\pi} F_o P(\tau,\mu,\Phi) - \mu_o,\Phi_o) \exp\left({}^{-\tau}/_{\mu_o}\right) + \frac{\omega(\tau)}{4\pi} F_o R(-\mu_o,n) P(\tau,\mu,\Phi,\mu_o,\Phi_o) \exp\left[-\frac{2\tau_a-\tau}{\mu_o}\right] \quad (3.23)$$

where μ_o is the cosine of the solar zenith angle and is positive, Φ_o is the azimuthal angle for incident solar beam, and F_o is the solar beam intensity at the top of the atmosphere. Here n is the index of refraction of the land surface relative to the atmosphere and τ_a is the total optical depth of the atmosphere. The first term in equation (3.23) represents the contribution from the

downward, incident beam source while the second term represents the contribution from the upward beam source reflected at the atmosphere-ocean interface because of the Fresnel reflection caused by the change in the refractive index between air and sea water. $R(-\mu_o, n)$ is the ocean surface reflectance for the solar beam. For the purpose of simplification, several assumptions were made in this work to obtain a solution with a high degree of generality that can be used for solving real problems. Below are the assumptions under which COART model solves the radiative transfer equation.

i. Only solar radiation is considered since it is strongly affected by the change in the refractive index due to aerosols and exhibits a much different transfer process in the coupled system. The emission is neglected for us to obtain a homogeneous solution.
ii. The specific intensity (radiance) is assumed to undergo anisotropic scattering and absorption of radiation in the coupled system.
iii. The land surface is assumed to be flat so as to neglect other radiative effects caused by the roughness of the surface by setting the wind speed to 0 m/s. A depth of 0 m assumes a land case with a vegetation cover of chlorophyll content of 0.2 mg/m^3.
iv. The atmosphere-land system has uniform optical properties since the system is not vertically stratified (single layered).
v. Atmospheric perturbations are as a result of aerosols only with other atmospheric species well taken care of by correcting their influences from those of the optical properties used.
vi. The Radiative Transfer Equation is solved in a plane-parallel geometry.
vii. The reflectance values obtained in this case are a combination of both surface and aerosol contribution that is similar to the case when determined by other standard methods.

By applying the above assumptions in solving equation 3.21 together with appropriate quadrature and the discrete ordinate method as a solver, a general solution for the radiative transfer equation (RTE) that is suitable for the single layer coupled system can be obtained [Zhonghai *et. al.*, 1994]. The general solution is the sum of both the homogeneous and particular solutions of equation 3.21 with the boundary conditions applied according to the COART model.

3.10.3 Radiative Forcing Concept

Radiative Forcing (RF) as defined by Ramaswamy *et. al.* (2001) is the change in net (down minus up) irradiance (solar plus long-wave; in W/m^2) at the tropopause after allowing for stratospheric temperatures to re-adjust to a radiative equilibrium, but with the surface and tropospheric temperatures and state held at the unperturbed values. A change in the net irradiance at the tropopause is of first order, a good indicator of the equilibrium global mean surface temperature change (ΔT_s). ΔT_s is related to the RF by equation 3.24 defined as:

$$\Delta T_s = \Omega . RF \quad \text{.....3.24}$$

where Ω is the climate sensitive parameter (integrated fluxes) over the study sites. $\Delta T_s = -3℃$ as estimated in the Fourth Assessment Report of the Intergovernmental Panel on Climate Change (IPCC, 2007). RF is expressed in terms of $℃/Wm^{-2}$ or K/Wm^{-2} where K is Kelvin.

CHAPTER 4

MATERIALS AND METHODS

4.0 Introduction

This chapter details the materials and methods by which various optical properties of aerosols were retrieved from already calibrated (Langley method) AERONET sun photometer measurements and how the data was used in this work. These instruments are standardized according to AERONET protocol with each being replaced every year by an identical sun photometer [Toledano *et. al.,* 2007]. Temporal and spatial characteristics of aerosol optical depth (τ) and angstrom parameter (α) were analyzed using the multivariate chemometric techniques described in Section 3.8. Aerosol number densities and extinction cross-section as well as radiative characteristics viz spectral irradiance, integrated fluxes and reflectance at varying optical air mass for 12 km and 0 km above sea level were determined from the measured aerosol optical properties. The 12 km atmospheric level was most preferred since is an average tropospheric layer in the tropics known to be dominated by atmospheric aerosols [IPCC, 2001].

Meteorological data (i.e. weekly total rainfall, weekly temperature and relative humidity at 06Z) was obtained from the Kenya Meteorological Department from meteorological stations nearest the specific AERONET site. For Malindi, the data was obtained from Malindi meteorological station in 2008 while that of Mbita was obtained from the Rusinga island kaswanga meteorological station in 2007. Nairobi's meteorological data was an average of four meteorological stations namely Dagoretti corner, Jomo Kenyatta International Airport (J.K.I.A), Wilson airport and Kabete Agromet meteorological stations from 2006 to 2008.

4.1 Description of Study Sites

The three sites at which this study was undertaken are: Malindi (2S, 40E) representing a maritime region since is close to the Indian Ocean (elevation 12 m); Mbita (0S, 34E) representing a rural site dominated by agricultural and biomass burning (elevation 1125 m) and Nairobi (an industrial city site) (1S, 36E) (elevation 1650 m). Nairobi's sun photometer

proximity to the industrial area allows for systematic monitoring of aerosols and pollution in this fast and expanding metropolis in East Africa. These sites are shown in Figure 4.1.

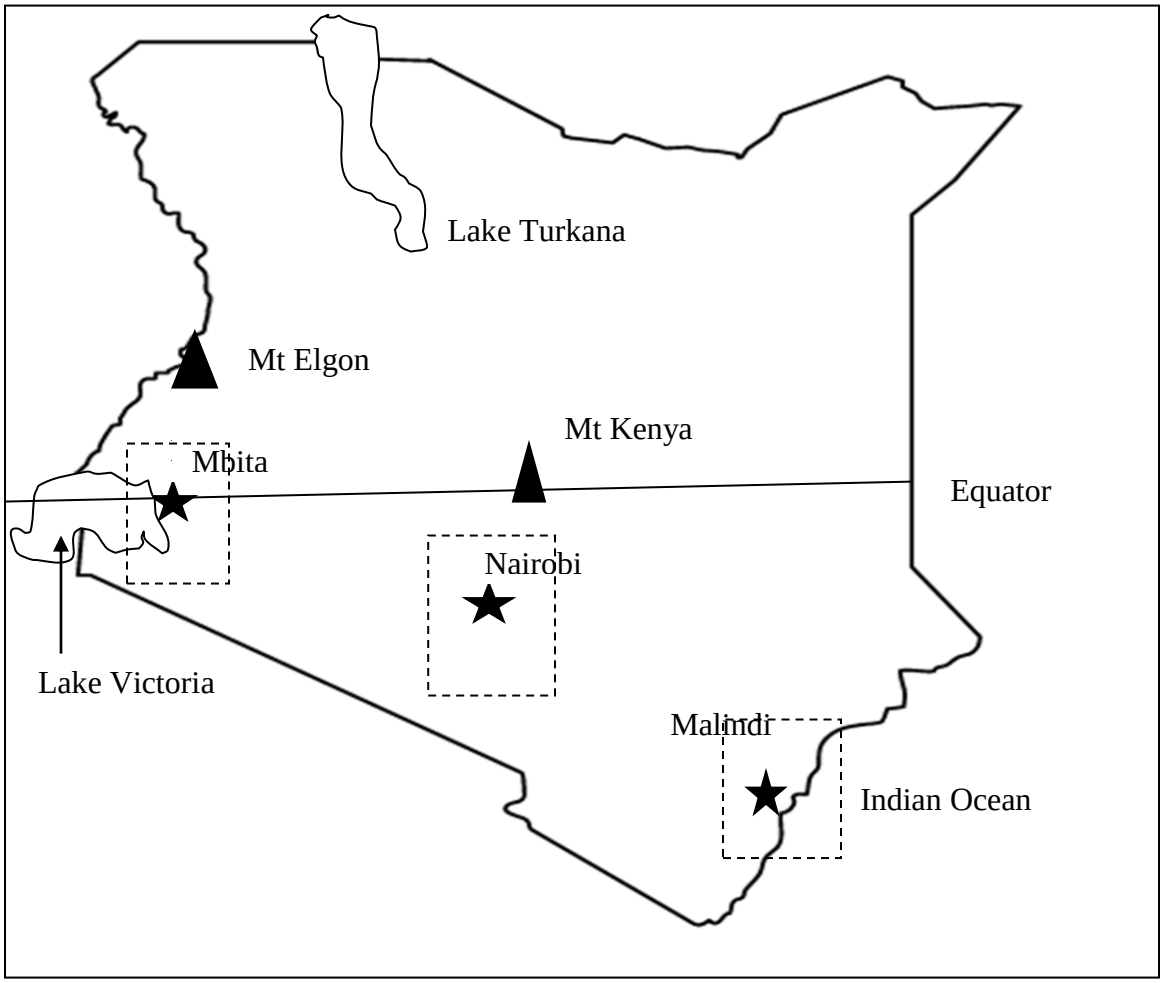

Figure 4.1: Map indicating the three AERONET sites of study in Kenya

4.2 Determination of Aerosol Optical Properties

The aerosol optical depth (τ) is derived based on the Beer-Lambert-Bouguer law as described by equation 3.7. A schematic of τ retrieval from direct beam sun spectrophotometric measurements is as outlined in Figure 4.2. τ is a basic optical property from which almost all other optical properties can be derived from as detailed in section 3.7. The spectral variation in τ is as described in equation 3.9 with single scattering albedo (ω) and angstrom exponent (α) derived

according to equations 3.10 and 3.15 respectively. Asymmetric factor (g) and complex refractive index were derived as shown in equations 3.11 and 3.13 respectively. Extinction cross section and aerosol number density were derived following equations 3.3 and 3.4 respectively.

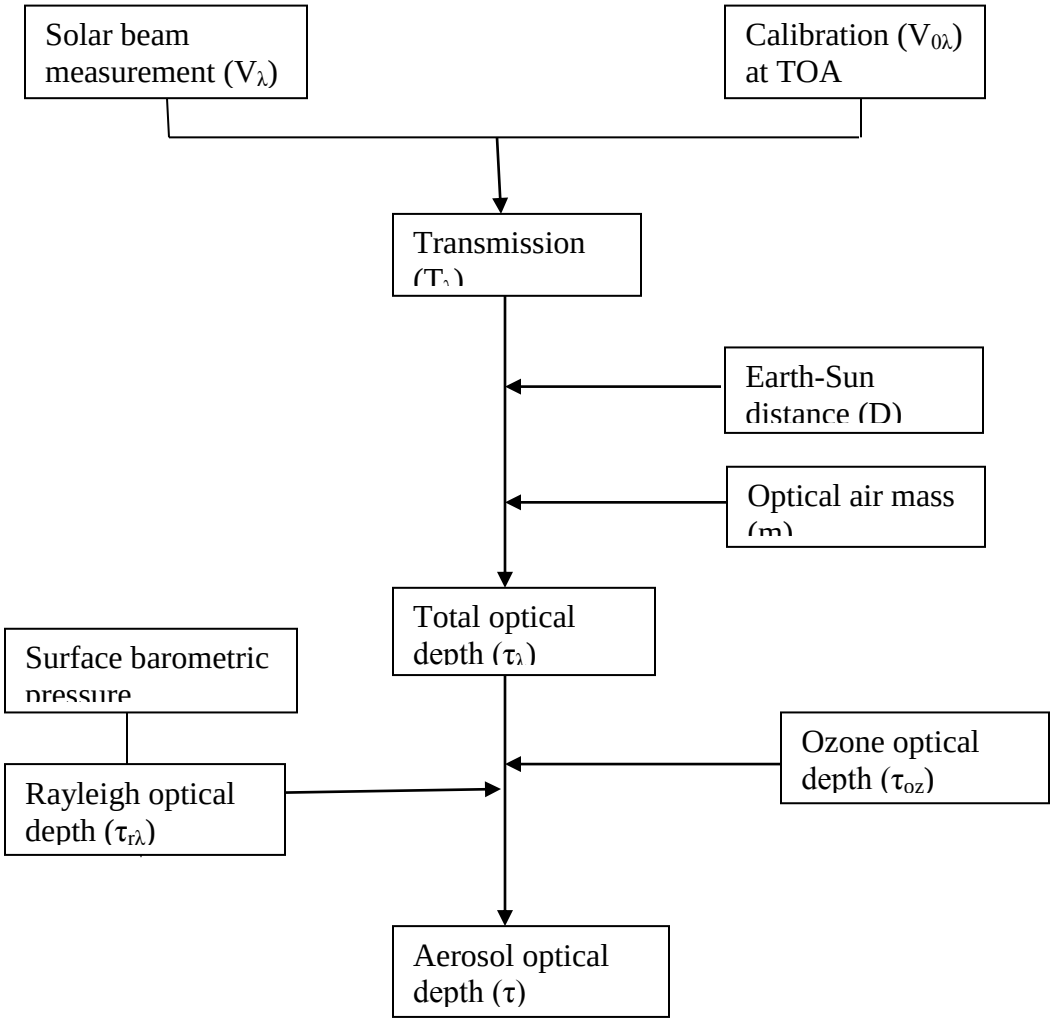

Figure 4.2: Schematic of aerosol optical depth retrieval from direct beam measurements

Solar beam falls on a diffraction grating inside the spectrophotometer which splits the solar beam into spectral components. These spatially split components of the solar beam are then projected onto the charged coupled device (CCD) detector that is connected to a computer. The CCD detector converts the measured data into an electrical charge whose intensity is related to the color in the spectrum and recorded in terms of voltage. Beer-Lambert-Bouguer law is used in computing τ from both measured (V_λ) and calibration constant ($V_{0\lambda}$) with details in Figure 4.2.

4.3 Data Formatting and Chemometric Computational Procedures

τ and α all time data were first pretreated by multiplying the respective values with the cosine of the solar zenith angle (SZA) for each wavelength at which it was measured. This was meant to convert all the measured values of the stated optical properties to a zero SZA measurements. Both raw τ and α datasets were separated into time intervals determined as Early Morning (7-8:59 AM), Late Morning (9-10:59 AM), Early Afternoon (11-12:59 PM) and Late Afternoon (1-3:30 PM). Weekly average values for τ and α were computed. They were then arranged in rows that represented sample space (aerosol number density) in a particular atmospheric wavelength channel while columns represented time intervals.

In order to analyze these data by multivariate chemometric techniques (PCA, PLS-DA and PCR) re-formatting was done to have both τ and α weekly average representing the samples while the time intervals were treated as variables since they were positively correlated with solar intensity. Mean centering was performed on the τ and α weekly average data through calculating the average data vector of all 48 rows in a data set and subtracting it point by point from each vector before multivariate chemometric techniques were applied to study their temporal variations. This process not only improves the precession of estimates from ill-conditioned and collinear data but it also enhances the interpretive process of visualizing the data. Temporal variations in τ weekly average values for each site were validated using PLS-DA while that of α were validated using both PLS-DA and PCR. The procedures used in both PLS-DA and PCR techniques were as follows:

- Inserting or appending a category variable in the data table arranged as described in PCA with the category variable having as many levels as the classes by defining one sample set for each class followed by building a category variable based on the sample sets.
- The category variable was then split into indicator variables that are taken to be the Y-variables (Early and Late morning time intervals) in the PLS model. A new variable set containing indicator variables only was created followed by performing a regression with PLS1 model used since only two classes were used i.e. 0 and 1.

- An option of either PLS1 or PCR was selected in the Camo Unscrambler 9.7 software to use PLS-DA and PCR respectively.

Spatial variations (Mbita, Nairobi and Malindi) in the measured/retrieved aerosol optical properties viz aerosol optical depth and angstrom exponent were studied using Hierarchical Cluster Analysis (HCA) on a data set using the Statistics Toolbox functions in MATLAB; the following procedure was used:

- Finding the similarity or dissimilarity between every pair of objects in the data set using the pdist function that calculates the Euclidean distance between them.
- Grouping the objects into a binary, hierarchical cluster tree by help of the linkage function that uses the distance information from above to determine the proximity of objects to each other.
- Determining where to cut the hierarchical tree into clusters using the cluster function that prunes the branches off the bottom of the hierarchical tree, and assigning all the objects below each cut to a single cluster.
- The clusters obtained are thereby represented in the form of dendrograms using the dendrogram function in the MATLAB toolbox.
- The MATLAB algorithm used in case of HCA was as described below:

```
load FILE NAME.txt
m=FILE NAME;
k=pdist (m);
n=linkage (k);
p=0;
z=dendrogram (n,p)
```

k=pdist (m) computes the Euclidean distance between pairs of objects in a 48 by 4 data matrix m while n=linkage (k) creates a hierarchical cluster tree using a Single Linkage Algorithm while z=dendrogram (n, p) generates a dendrogram with not more than p leaf nodes by collapsing lower branches of the tree; to display the complete tree, we set p=0 as indicated in the algorithm.

Validation of AERONET τ and α at 500 nm and 440-675 nm respectively was done using MODIS i.e. on both Terra and Aqua satellites data. MODIS measurements for both τ and α were at 550 nm and 470-660 nm wavelength channels respectively. This was achieved through a web-

based application developed by GES DISC known as GIOVANNI MOVAS [Badarinath *et. al.*, 2009]. MODIS Terra and Aqua monthly level-3 data for both τ and α for 1×1 degree resolution product in the area of interest i.e. Nairobi (36W 37E, -1S 0N), Mbita (34W 35E, -1S 0N) and Malindi (40W 41E, -3S -2N) was used. The data was averaged annually and compared with that retrieved from AERONET annually averaged data at zero SZA at the specified wavelengths. The dashed MODIS grid boxes for three locations are indicated Figure 4.1.

4.4 Determination of Radiative Characteristics

The radiative characteristics, in this case spectral irradiance, integrated fluxes, and reflectance of atmospheric aerosols were determined using the COART model over the study sites. This was done in accordance with the assumptions and boundary conditions discussed in Section 3.10.2. The radiative characteristics were evaluated at 12 km and 0 km above sea level (except for reflectance) with SZAs ranging from 0 to 80 degrees. The 12 km atmospheric altitude was considered since it is the standard height at which air craft emissions into the atmosphere is prevalent. Also, the tropopause has its average altitude value at this point in which aerosol concentration is believed to be highest as assumed by many radiative transfer models [IPCC, 2001]. Determination of the radiative characteristics of the atmosphere under specific site of study is on assumption that the respective atmosphere is composed purely of aerosols whose optical properties have been determined by Cimel sun photometers from the AERONET network.

4.4.1 Solution of Radiative Transfer Equation (RTE)

A solution of the basic Radiative Transfer Equation (RTE) 3.21 used by the COART model is obtained under different assumptions discussed in Section 3.10.2. The radiative characteristics viz spectral irradiance, integrated fluxes and reflectance reported in this work were determined and discussed. Implementation of equation 3.24 made it possible to estimate the level of radiative forcing of the atmosphere for the sites under study.

CHAPTER 5

RESULTS AND DISCUSSION

5.0 Introduction

Studies on aerosol characteristics i.e. physical, chemical or optical as determined by either active (involves transmitting energy into the environment, allowing that energy to reflect off the surrounding environment, and then recollecting the energy using a sensors) or passive (the energy collected is provided by the environment from which data is collected) remote sensing techniques enhance the understanding of aerosol influence on climate, ambient air quality, health e.t.c over the region of interest. A passive remote sensing technique was not only preferred because of its availability, but also as a result of its reliability in terms of consistence in obtaining aerosol optical properties. The continuous process of obtaining aerosol optical properties aided studies in both temporal and spatial characteristics of aerosol particles in the atmosphere over a given site that are known to be highly inhomogeneous.

Univariate investigations on the dependence of aerosol optical depth (τ) (at zero SZA) with respect to weekly total rainfall and temperature was achieved by plotting weekly averages of ($\tau \times 100$), weekly total rainfall and temperature against week of the year as shown in Figures 5.1-5.3. This dependence was investigated at λ=340 nm (UV), 675 nm (Vis) and 1020 nm (IR) over the study sites (except for Malindi which did not have data at λ=340 nm and was replaced by λ=440 nm). The τ values were multiplied by hundred to enhance visualization and proper scaling for all the parameters. Figures 5.1-5.3 below show the variations in τ over the study sites in relation to rainfall and temperature. Weekly averages were preferred since they could form enough data desired by appropriate chemometric techniques used in the study.

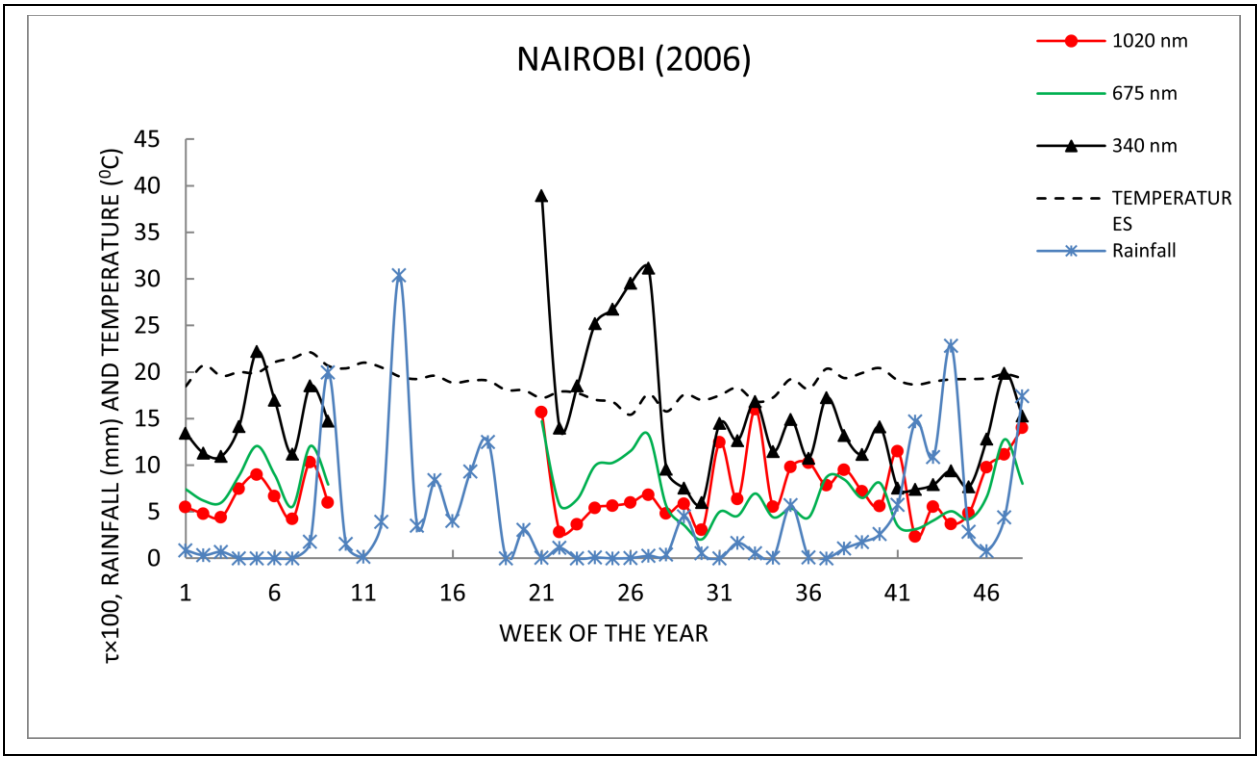

Figure 5.1: Dependence of (τ×100) on rainfall and temperature over Nairobi (2006)

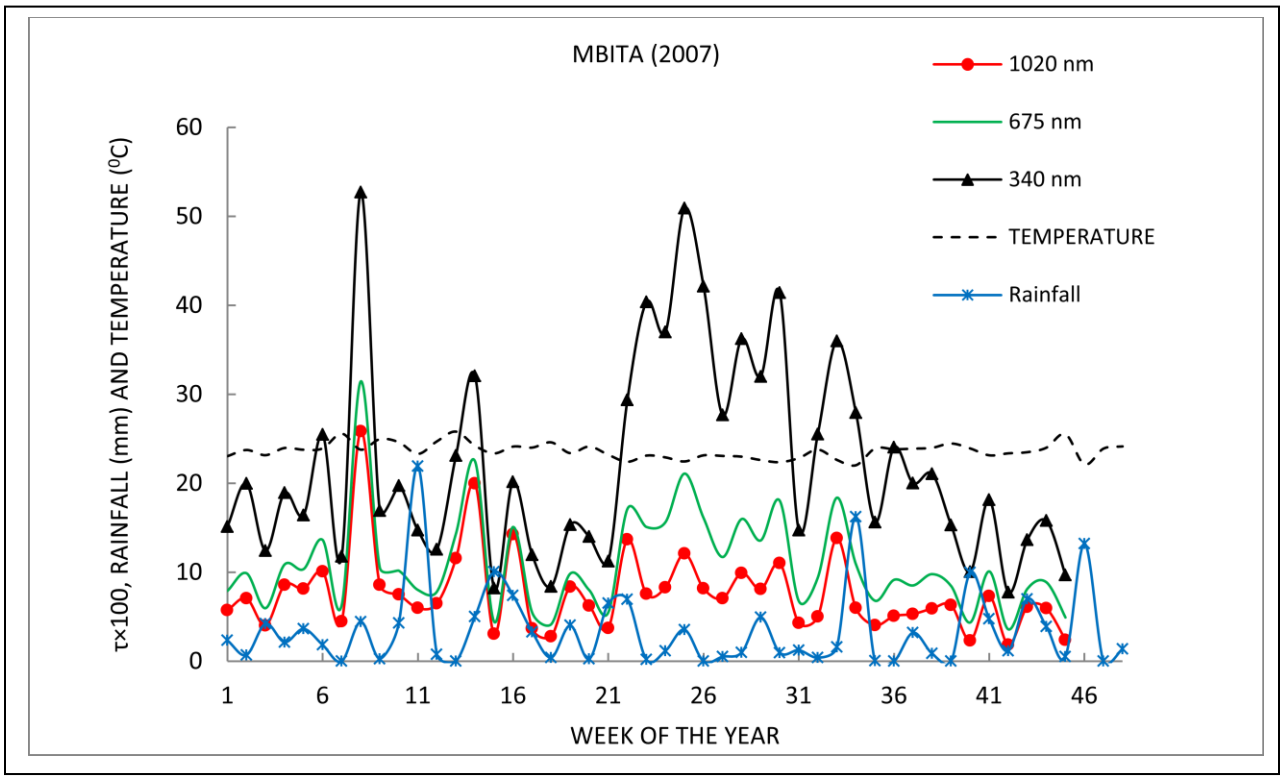

Figure 5.2: Dependence of (τ×100) on rainfall and temperature over Mbita (2007)

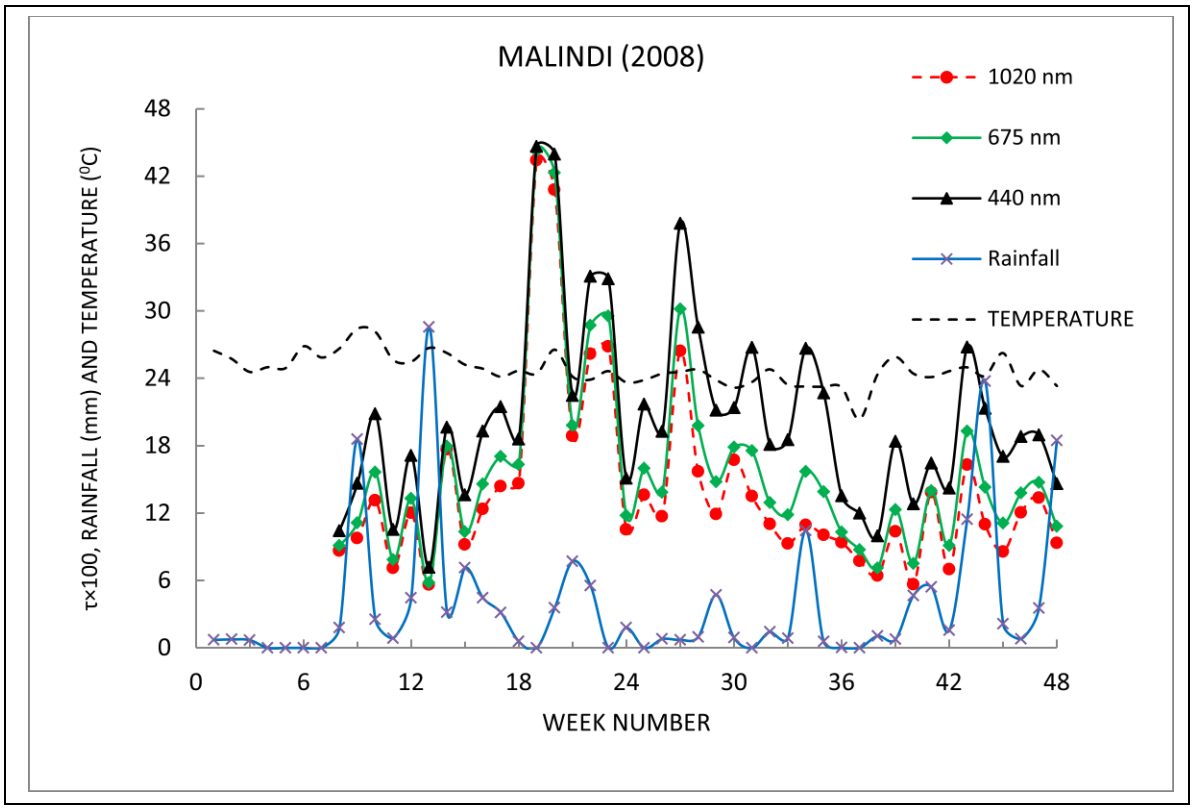

Figure 5.3: Dependence of (τ×100) on rainfall and temperature over Malindi (2008)

As noted in Figure 5.1, general variation in τ (which corresponds to aerosol burden in the atmosphere) with respect to rainfall is both site, and aerosol particle size independent. An increase in rainfall is accompanied by a corresponding decrease in atmospheric aerosol burden and vice versa. The decrease may be attributed to the wet deposition of aerosol particles. The efficiency of deposition is independent of aerosol particle size. During dry spells (W22-W27: W= week), an increase in aerosol burden across all aerosol particle sizes is noted and this may correspond to mineral dust lifting into the atmosphere and reduced aerosol removal processes e.g. dry deposition (which does not remove aerosol particles from the atmosphere as effectively as wet deposition). It can be concluded that coupled influences of rainfall and temperature alter aerosol densities; in the Nairobi atmosphere the bigger influence is in the fine fraction and it occurs during the cold (W22-W30) as compared to warm spells. The influence of relative humidity (see Table 7.2: Appendix) on aerosol burden dominate in both fine and coarse aerosol particles through coagulation and condensation processes. These aerosol removal processes lower aerosol burden in these size fractions as observed between (W30-W45) in Figure 5.1.

Variations in τ trends with respect to both rainfall and temperature are dependent on the year of interest. This is as a result of varying aerosol generation and removal mechanisms that change significantly each year.

Variation in aerosol atmospheric burden over Mbita with respect to rainfall is also aerosol particle size independent (Figure 5.2). The onset of Long Rains (W9) over Mbita, a rural site, is characterized by heavy biomass burning due to farm preparation for agricultural activities which enriches the atmosphere gradually with smoke particles. The hygroscopic properties of these smoke particles enhance their size transformations thus increasing the atmospheric aerosol burden in both visible and near IR aerosol size regimes as observed particularly in week eight (W9). Maturing plants enhance biogenic aerosols e.g. pollen between W23-W32. There is an observable decline in atmospheric aerosol burden across all investigated sizes over Mbita between W36-W46 corresponding to the months of October-December 2007. This may be attributed to fewer aerosol generational processes in the rural region after harvesting of crops when most land lies fallow for the next planting season.

Malindi reveals similar observations concerning rainfall influences on τ with respect to particle size. Aerosol optical depth (τ) is the same for all particle sizes between W18-W21. During this time interval, the site experienced no rainfall; this enhances mineral dust loading that promotes aerosol burden in almost equal proportions in the atmosphere. From Figure 5.3, we note a drop in τ across all aerosol particle sizes between (W35-W39, W45), this is accompanied with no rain and the lowest temperature in the same time interval over the site. The drop in τ suggests the effect of temperature on atmospheric aerosol burden is through mineral dust loading over the site.

An attempted to explain some of the observations from Figure 5.1-5.3 on the influence of both weekly total rainfall and temperature on τ wasn't comprehensive and explicit enough. This is because of the inherent extreme variability of the atmospheric aerosol and the multivariate nature of environmental processes and phenomena, hence, multivariate techniques are preferred. Multivariate techniques can broadly be classified as supervised and unsupervised [Gemperline, 2006]. The latter comprises of such methods as Cluster Analysis (CA), Principle Component

Analysis (PCA) and Factor Analysis (FA), e.t.c. while supervised methods include Analysis of Variance (ANOVA), Partial Least Squares (PLS) and Linear Discriminant Analysis (LDA). The last two methods may be linked to provide Partial Least Squares Discriminant Analysis (PLS-DA), etc. Some of these methods were used to reduce data dimensionality (PCA) and to identify hidden classifications and patterns in the retrieved aerosol optical properties (PLS-DA and PCR), tasks which cannot be accomplished by univariate techniques.

Temporal and spatial variability in τ and α was studied by Principle Component Analysis (PCA). Compared to monthly averages, weekly averages of τ and α provide enough data and data resolution desired by these techniques in a given year. These variations were surveyed over Nairobi, Mbita and Malindi for the years 2006, 2007 and 2008 respectively for all the available wavelength channels for each site. Temporal structures in weekly averages of τ and α were studied using PCA, PLS-DA and PCR methods in order to compare and validate each other. The retrieved data were obtained at specified time intervals as Early Morning (7-8:59 AM), Late Morning (9-10:59 AM), Early Afternoon (11-12:59 PM) and Late Afternoon (1-3:30 PM) determined on assumption that the solar intensity is fairly constant during the selected time intervals. Both extinction cross section and aerosol number densities were calculated from aerosol optical depth across all possible wavelengths. Radiative characteristics (i.e. reflectance, spectral irradiance, integrated fluxes) were determined using the COART model at the same wavelengths as above.

In order to realize this, daily τ data were first separated according to the time intervals stated above, followed by determination of weekly averages in the same time intervals starting from the first day of the year for the whole year. The Camo Unscrambler 9.7 software was used with the data matrix organized as variables (columns) corresponding to the above stated time intervals and samples (rows) corresponding to mean-centered τ and α weekly averages. PCA and PLS-DA procedures were realized as outlined in Section 4.3 and validated using the cross validation method. For PLS-DA, both early and late morning data were used as a training set for analyzing the temporal characteristics of τ and α weekly average values for early and late afternoon time intervals at each site, specific year and wavelength.

5.1 Aerosol Optical Depth (τ)

5.1.1 Temporal Characteristics of Aerosol Optical Depth

PCA was used to study the temporal characteristics of τ as a function of aerosol particle sizes; the results are indicated in the score plot in Figures 5.4a-b. Nairobi had 48 weekly average values of τ (zero SZA) for the above specified time ranges in 2006. Three Principle Components (PCs) with a total explained variance of 97 % were extracted explaining the temporal characteristics. PC1 (76 %) represents the rainy period (both Long and Short Rains) while PC2 (14 %) represents non rainy periods and PC3 (07 %) represents relative humidity.

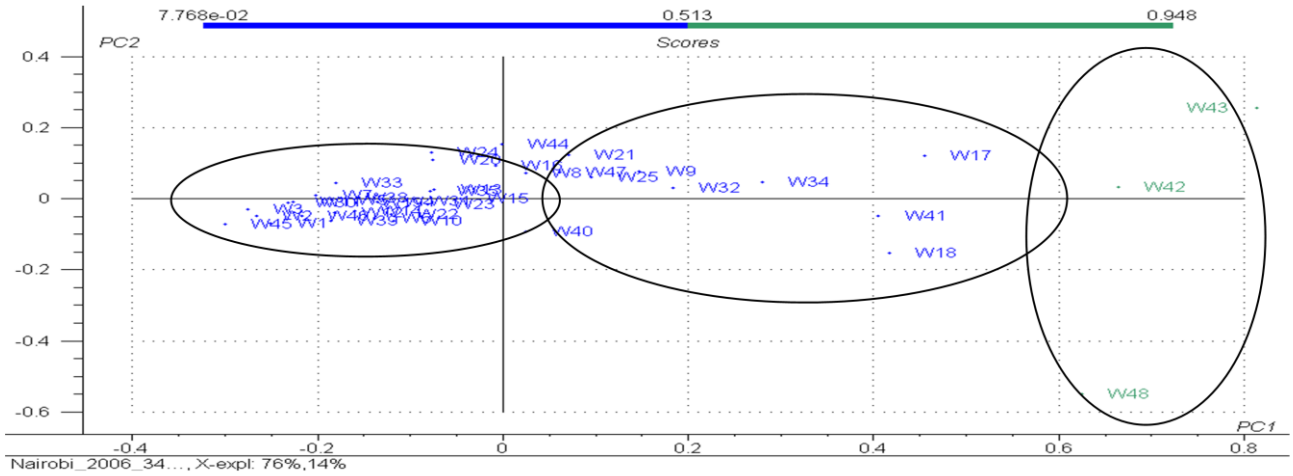

Figure 5.4a: Example of plot of scores for 48 samples in four variables data set at λ=340 nm for Nairobi (2006).

A seasonal classification of τ values as rainy period (blue) and non rainy period (green) based on PC1 and PC2 respectively is revealed by the score plot in Figure 5.4a. Both long and short rains periods are characterized by low τ values (0.07768-0.513) caused by wet deposition of aerosol particles by rainfall washout prevalent between W9-W20 and W40-W48. Aerosol removal via wet deposition as caused by long and short rains is of similar degree as noted in Figure 5.4a in which both short and long rains periods over the site are grouped together. It is noted that Nairobi experiences low temperatures and solar intensities (W21-W31) from June-August i.e. 10.5 ^{0}C against an annual average of 18.92 ^{0}C (Table 7.2); this limits the production of aerosol

particles through photochemical processes which alters aerosol number densities towards realizing low τ values in a manner similar to wet deposition.

Urban development may also cause Nairobi to be an urban heat island hence elevating its temperatures slightly higher than those of the surrounding rural areas. This allows for the transportation of cold air accompanied by aerosol particles from the surrounding regions hence the high τ values particularly in non-rainy periods (W42, W43 and W48). The higher τ values in the same period (0.513-0.948) may also be as a result of high temperatures an average of 19.98 ^{0}C and solar intensities (Table 7.2). This condition accelerates production of aerosol particles through photochemical processes with less removal processes by dry deposition. Relative humidity (RH) (PC3) reveals an explained variance of 07 % in the 340 nm aerosol particle size, 1 % higher than the rest of the particle sizes. This shows that coagulation process on photo-chemically emitted aerosol particles as modulated by industrial emissions dominate aerosol particles in the 340 nm wavelength channel. Figure 5.4b shows the score plot of PC1 against PC3 over Nairobi in 2006 for the 340 nm wavelength channel.

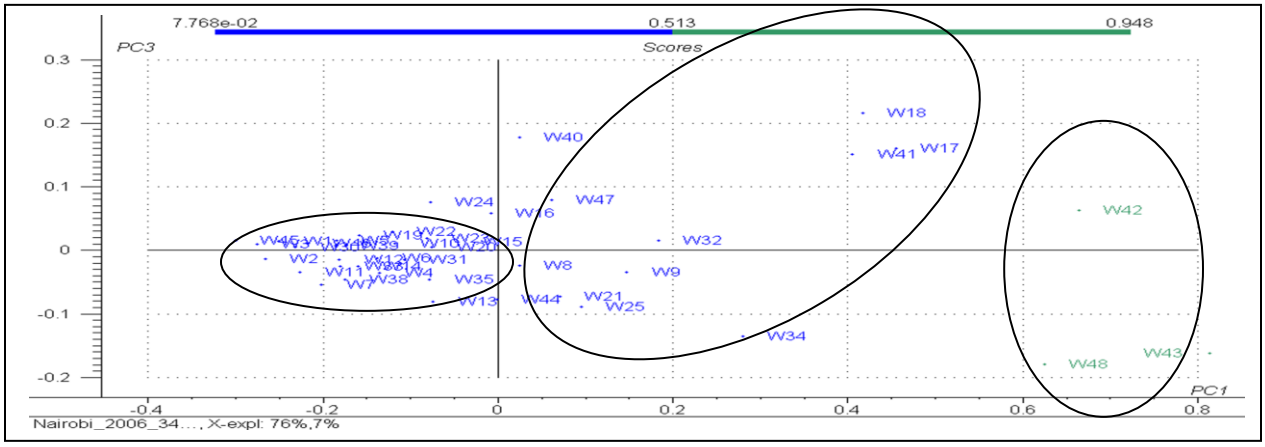

Figure 5.4b: Example of plot of scores for 48 samples in four variables data set at λ=340 nm for Nairobi (2006).

Validation of the above PCA results was realized by performing PLS-DA analysis on the same data as described in Section 5.0. The PLS-DA results reveal a constant X explained variance of 90 % for PC1 at λ=340 nm as indicated in Figure 5.5.

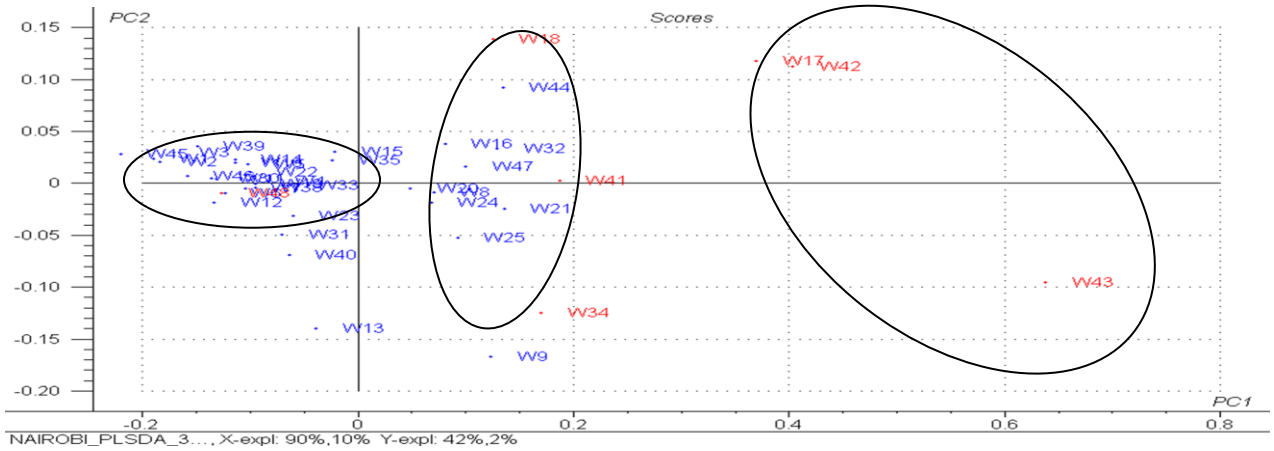

Figure 5.5: Example of plot of scores with X and Y loadings for 48 samples of the PLS-DA model at λ=340 nm over Nairobi (2006).

Discrimination of τ values using the PLS-DA model is indicated by different colors i.e. blue for rainy periods and red for non-rainy periods. This technique reveals similar groups in weekly average τ values to that of PCA as indicated in the score plots of Figure 5.4a. Non-rainy (red) periods as revealed by PLS-DA correspond to W17, W18, W34, W41, W42, W43 and W48. The last three week numbers (W42, W43 and W48) corresponding to that revealed by PCA. The minimal difference in week numbers as revealed by both unsupervised (PCA) and supervised (PLS-DA) techniques is due to minor variations in data pretreatment procedures. It is also note that the grouping in τ values is aerosol particle size independent i.e. aerosol removal processes over the Nairobi atmosphere as influenced by both rainy and non-rainy periods by wet and dry deposition processes respectively has no preference to a particular aerosol size regime as observed in Figures 5.4a, 7.1-7.2.

Mbita's τ classifications also reveal two groups i.e. rainy and non-rainy seasons as shown in Figure 5.6 and Figure 5.7. The rainy period (blue) is characterized by lower τ values (0.074-0.342) also attributable to active wet removal process on aerosol particles in the atmosphere. Non-rainy period (green) comprises of weekly τ values namely W8, W24, W25, W26, W28, W29, W30, W33 and W34 characterized by heavy biomass burning (as a source of energy) and dry deposition process due to gravitational pull that does not efficiently remove aerosol particles in the atmosphere hence the high τ values (0.342-0.6091). The effect of local air circulation between Lake Victoria and Mbita allowing for transportation of cold air accompanied by aerosol

particles from the Lake may also explain high τ values observed during the non-rainy period. It was also note that the effect of both rainy and non-rainy seasons on τ values is aerosol particle size dependent as shown from Figures 5.6, 7.3-7.4.

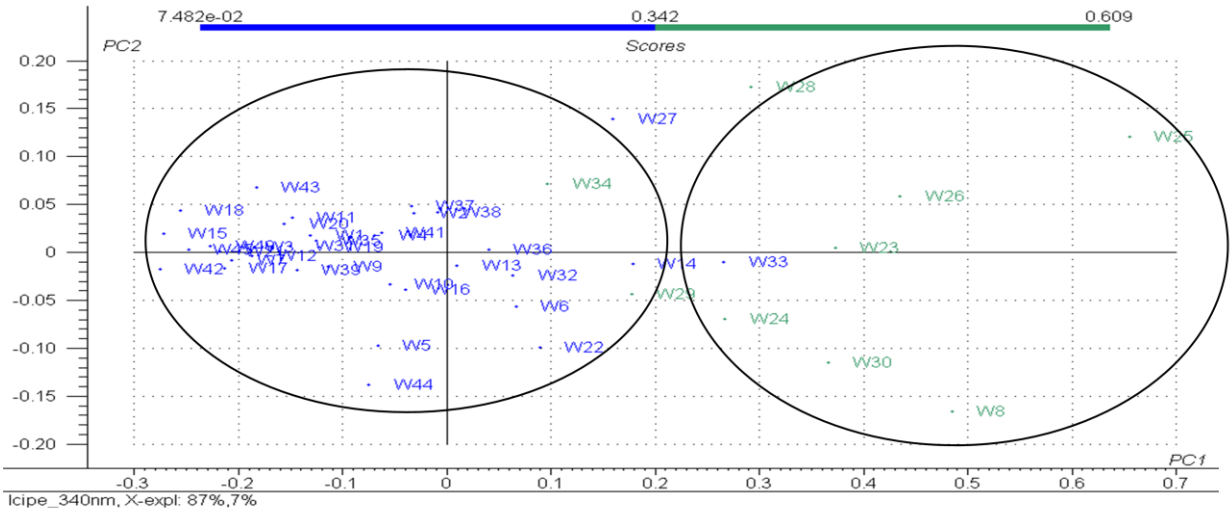

Figure 5.6: Example of plot of scores for 48 samples in four variables data set at λ=340 nm for Mbita (2007).

The dependence of aerosol particle size distribution on both rainy and non-rainy seasons over the site seems to be altered by relative humidity. It was noted that common weekly τ averages (W8, W25 and W30) in the dry season for all aerosol particle sizes i.e. 340 nm, 675 nm and 1020 nm are characterized by higher temperature (24.78 ℃), low relative humidity (47.5 %) and lack of rains over the site (Table 7.2). These high temperatures may accelerate dust lifting while low rainfall (4.50 mm) enhances aerosol size transformations of the biomass burning aerosol particles.

The two techniques used are in agreement since they reveal almost similar week numbers for both rainy and non-rainy periods as shown in Figures 5.6-5.7. The influence of relative humidity (PC3) is less by 3 % when compared to that of Nairobi in the 340 nm wavelength channel. This is because Mbita is a rural site that is relatively free from anthropogenic influences, hence the low explained variance. On the other hand, it was noted that the explained variance for PC3

increase to about 07 % in the 675 nm, 870 nm and 1020 nm wavelength channels suggesting the dominance of dust lifting as influenced by relative humidity.

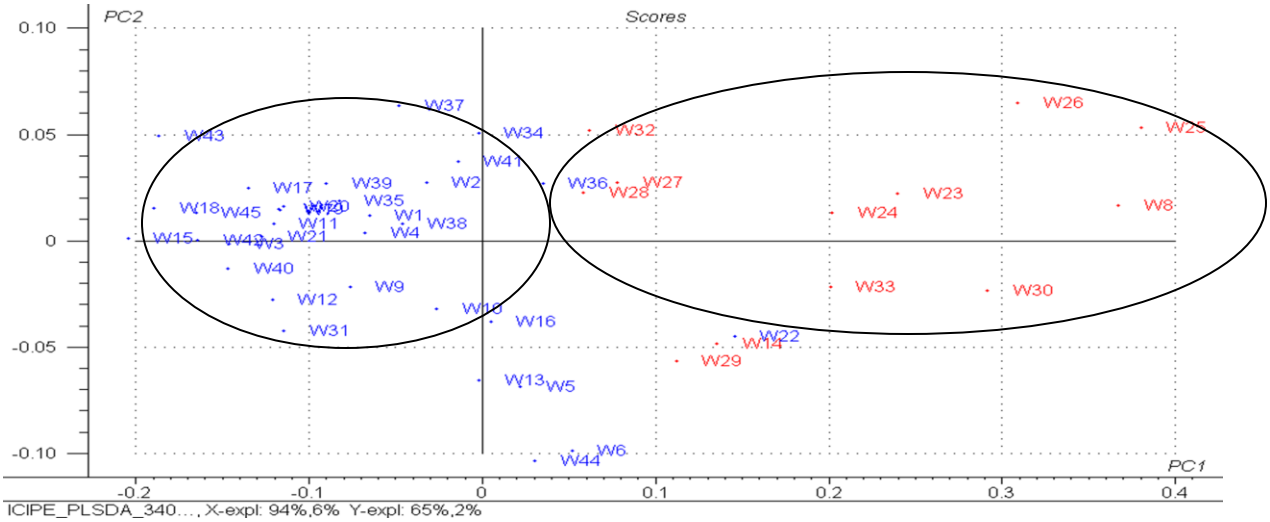

Figure 5.7: Example of plot of scores with X and Y loadings for 48 samples of the PLS-DA model at λ=340 nm over Mbita (2007).

Rainy period (blue) in both Figures 5.8-5.9 and non-rainy period (red and green in Figures 5.8-5.9 respectively) are the two significant seasons that regulate weekly τ average values over Malindi. Short and Long rains seasons over the site are responsible for wet deposition of aerosol particles that also explain the lower τ values (0.0357-0.241) during the rainy period as indicated in Figures 5.8-5.9 for PCA and PLS-DA respectively. Non-rainy period (W20, W21, W22, W23, W25, W26, W27, W29, W30 and W31) weekly τ values correspond to months of June-August. This period is characterized by high τ values (0.244-0.452) since dry deposition does not effectively remove aerosol particles from the atmosphere. Higher temperatures (from Table 7.2) over Malindi may also enhance local air circulation that allows for the transportation of both sea spray and sea salt aerosol particles from the Indian Ocean which explains the observable high τ values during the non-rainy period.

It was also deduced that both PCA and PLS-DA are in agreement over the seasonal changes in τ i.e. atmospheric aerosol densities in terms of the effect of rainfall distribution and solar intensity over the year for sites under consideration. Other than modulation by meteorological parameters

only, both rain distribution and solar intensities determine aerosol mode of generation, distribution and long distance transport in the atmosphere.

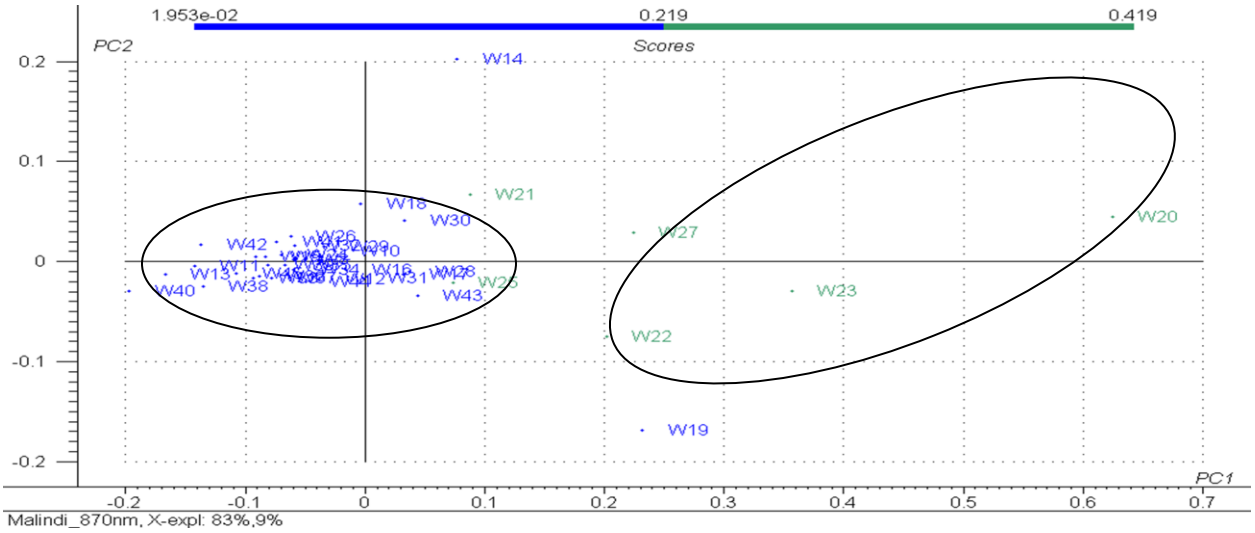

Figure 5.8: Example of plot of scores for 48 samples in four variables data set at λ=440 nm for Malindi (2008).

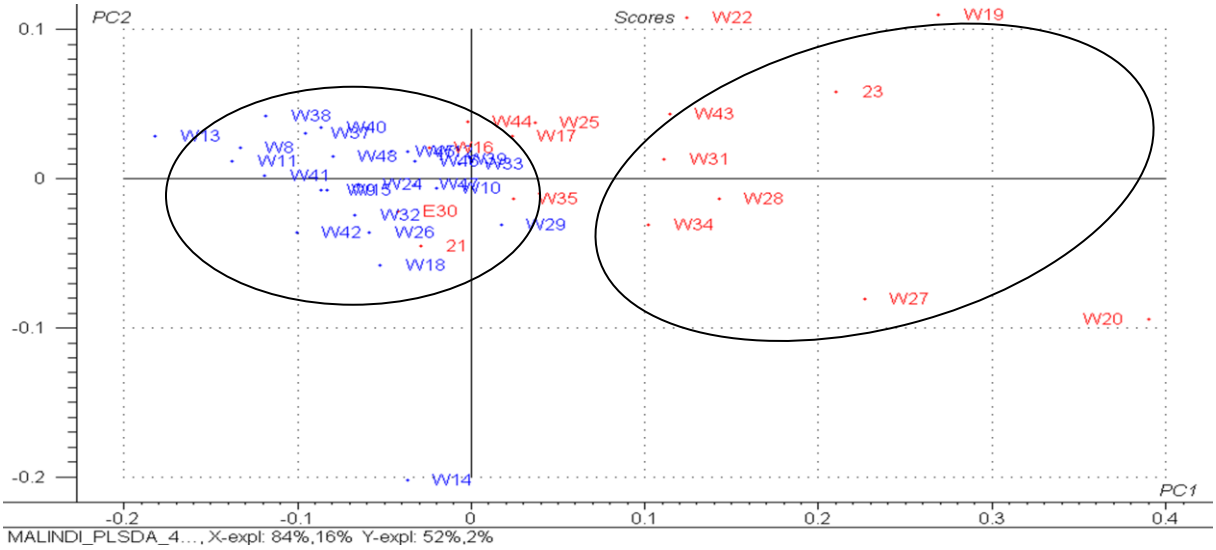

Figure 5.9: Example of plot of scores with X and Y loadings for 48 samples of the PLS-DA model at λ=440 nm over Malindi (2008).

A summary of similarities and differences in the observed temporal characteristics of atmospheric aerosols for each site was determined by both PCA and PLS-DA across all possible wavelength channels as given in Table 5.1.

Table 5.1: Comparison of temporal characteristics in τ values as obtained by PCA and PLS-DA at different sites and aerosol particle sizes.

Site	Method	Explained variance (PC1 and PC2 respectively) (%)						
		λ=340 nm	λ=380 nm	λ=440 nm	λ=500 nm	λ=675 nm	λ=870 nm	λ=1020 nm
Nairobi (2006)	PCA	76 14	77 14	77 14	77 14	78 14	77 15	77 16
	PLS-DA	90 10	90 10	90 10	90 10	91 09	90 10	90 10
Mbita (2007)	PCA	87 07	87 08	85 09	83 10	77 19	76 19	76 19
	PLS-DA	94 06	93 07	92 08	91 09	90 10	91 09	91 09
Malindi (2008)	PCA			81 08		83 08	83 09	83 09
	PLS-DA			84 16		85 15	84 16	84 16

Table 5.1 reveals the clear particle size independent influence of season via rainfall density on weekly τ average values over the study sites. For Nairobi and Malindi, the influence appears to be aerosol particle size independent as revealed by both PCA and PLS-DA. Low τ values are typical during the rainy season, which may be likened to wet removal process of aerosol particles hence the significant explained variance in PC1 on the study sites. Influences of non-rainy season on τ are characterized by dry deposition process on aerosol particles (which does not remove aerosol particles from the atmosphere), together with other active aerosol generation processes such as photochemical processes (UV-size) and dust loading (IR-size). These processes explain the observable high τ values across all aerosol particles sizes and sites. The influence of rainfall distribution over the sites of study dominates aerosol removal processes through wet deposition (Table 5.1).

In Nairobi, wet deposition of aerosol particles in the 675 nm wavelength channel is higher by 1 % as compared to the rest of channels (Table 5.1 for both PCA and PLS-DA). This suggests a slightly higher concentration of atmospheric aerosol in this channel that may be due to both vehicular and industrial emissions. Vehicular emissions due to high traffic densities over Nairobi promote both black and organic carbon aerosol particles that are known to absorb the incoming solar radiation and then heat up the atmosphere. Industrial emissions dominated by both sulfates and nitrates too undergo photochemical processes that increase the concentration of aerosol particles known to scatter the incoming solar radiation hence cooling the atmosphere. High concentration of these aerosol particles in the atmosphere experience significant wet deposition process, which explains the slightly higher explained variance (by 1 %) as compared to the rest of the wavelength channels.

Wet deposition of aerosol particles over Mbita dominates in the 340 nm, 380 nm, 440 nm and 500 nm wavelength channels and it decreases for 675 nm, 870 nm and 1020 nm channels. Biomass burning activities as a source of energy and farmland clearing, which is present in this area, promote smoke particles that absorb the incoming solar radiation heating up the atmosphere. Due to their hygroscopic properties, smoke particles absorb water causing them to evolve in their sizes [Eck *et. al.,* 1998]. Relatively higher concentration of smoke particles experience significant wet deposition explaining the higher explained variance (see Table 5.1) in the 340 nm, 380 nm, 440 nm and 500 nm wavelength channels. Low aerosol concentration in the infra-red aerosol particle size regime may be attributed to the scanty dust loading and biogenic aerosol emissions to the atmosphere over the site and are seasonal dependent. Hence their removal from the atmosphere through wet deposition is proportionately lower. Thus, the low explained variance (Table 5.1) in the 675 nm, 870 nm and 1020 nm wavelength channels.

Uniform wet deposition as well as other processes on atmospheric aerosol particles of different sizes is noted over Malindi as suggested by both PCA and PLS-DA hence there are no dominant aerosol particle sizes. It is notable that both techniques i.e. PCA and PLS-DA are in agreement and successful in studying the temporal characteristics of τ over the study sites. It was deduced that these temporal variations are dependent on rainfall distribution, relative humidity and human activities dominating the site. On the other hand, wet deposition of aerosol particles supersedes

dry deposition process as noted from the various explained variances. Notable differences in the explained variance between PCA and PLS-DA for different aerosol particle sizes can be attributed to the fact that one technique is unsupervised (PCA) while the other is supervised (PLS-DA).

5.1.2 Spatial Characteristics of Aerosol Optical Depth

5.1.2.1 Spatial Variation Between Nairobi and Mbita

Spatial characteristics of weekly τ values for Nairobi and Mbita (October-December 2007) and Nairobi and Malindi (March-May 2008) across all common wavelength channels are displayed in form of dendrograms using HCA. Specification of the time intervals limits the influence of season on the analyzed weekly average τ values since all the three sites experience similar seasonal variations. Comparison of the spatial characteristics in τ between Malindi-Mbita and Nairobi-Mbita-Malindi weren't possible since there were no common time interval data over the sites in any wavelength channel. τ has a geographical variability based on atmospheric aerosol burden since spatial variation between Nairobi-Mbita values in the stated time interval for the 675 nm wavelength channel are separated into two clear clusters in Figure 5.10.

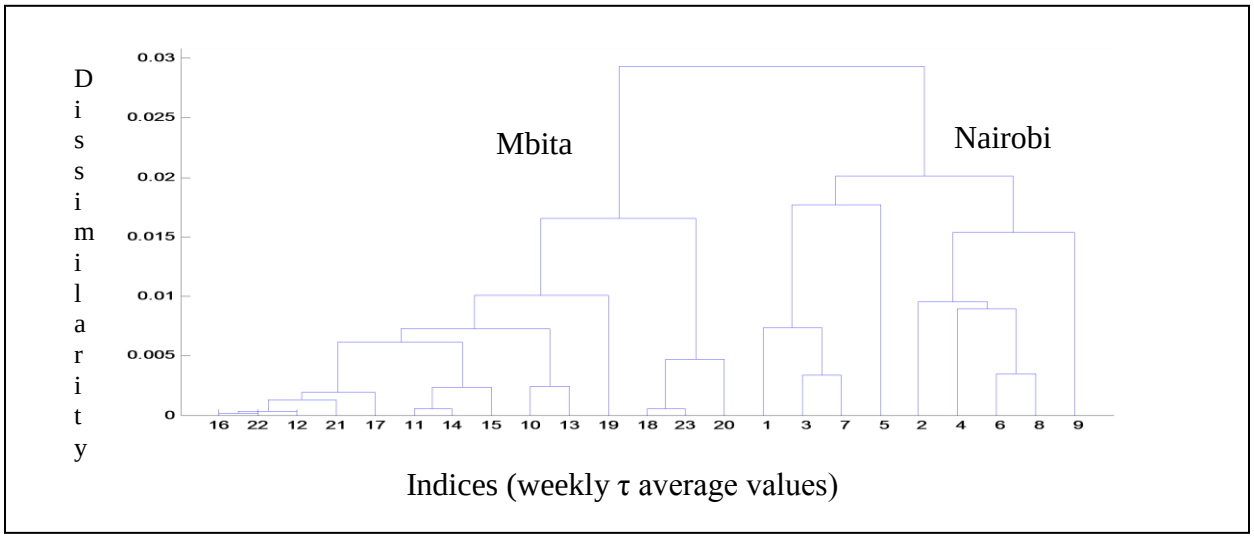

Figure 5.10: Spatial characterization of 23 weekly average τ from Nairobi and Mbita for 675 nm aerosol size fraction (October-December 2007).

HCA using the Euclidean distances was applied utilizing a MATLAB 7.1 algorithm. This produced dendrogram of weekly τ values as shown in Figure 5.10 for the 675 nm wavelength channel. It is evident that there are two groups of τ weekly average values; group one is characterized by indices from 1-9 (corresponding to Nairobi) while group two has indices from 10-23 (corresponding to Mbita). This division is attributed to the difference in aerosol burden (concentration) in this atmospheric channel between Nairobi and Mbita during the studied period. The two sub-clusters over Nairobi i.e. 1-5 and 2-9 respectively correspond to sulfate and nitrate dominated aerosols due to industrial emissions and black and organic carbon aerosols due to vehicular emissions.

Indices 2 and 4 in Figure 5.10 correspond to week number W38 and W40 respectively over Nairobi. RH as modulated by low rainfall (1.05 mm) and higher temperature (19.36℃) for index 2 and low rainfall (2.61 mm) and higher temperature (20.42℃) for index 4 modulates aerosol densities in the size regime through coagulation process of both sulfate and nitrate dominated aerosol particles. Sub-cluster 6-8 corresponds to week W42 and W44 which have a constant relative humidity (71.04 %) as noted in Table 7.2: Appendix. From Figure 5.10, it was noted that Mbita has got two main sub clusters namely 18-20 likened to fresh aerosol smoke particles while sub-cluster 16-19 may be attributed to aerosol smoke particles at different aging process levels [Eck *et. al.,* 1998]. Modulation of sub-clusters over Mbita is noted in Figure 5.10 to be varying with relative humidity as shown in Table 7.2: Appendix.

Dendrograms in Figures 5.10-5.12 for 675 nm, 1020 nm and 440 nm wavelength channels respectively indicate that spatial characteristics in aerosol burden is independent of their particle size. This is because all the two major groups suggested by each aerosol particle size regime are similar to the ones in the 675 nm wavelength channel. Variations in the sub-clusters in each group for each wavelength channel is however as a result of other aerosol particle characteristics e.g. hygroscopicity, chemical composition and their mode of generation which affect aerosol burden, size and distribution in the atmosphere. For instance, Mbita (Figure 5.10) is dominated

by smoke particles characterized by high hygroscopic properties that cause them to evolve in their sizes hence the various sub-clusters while Nairobi has both black and organic carbon aerosol particles from vehicular emissions attributed to high traffic densities, together with sulfate and nitrate dominated aerosol particles that result from photochemical processes due to industrial emissions in the 675 nm aerosol particle size [Haywood *et. al.*, 1997].

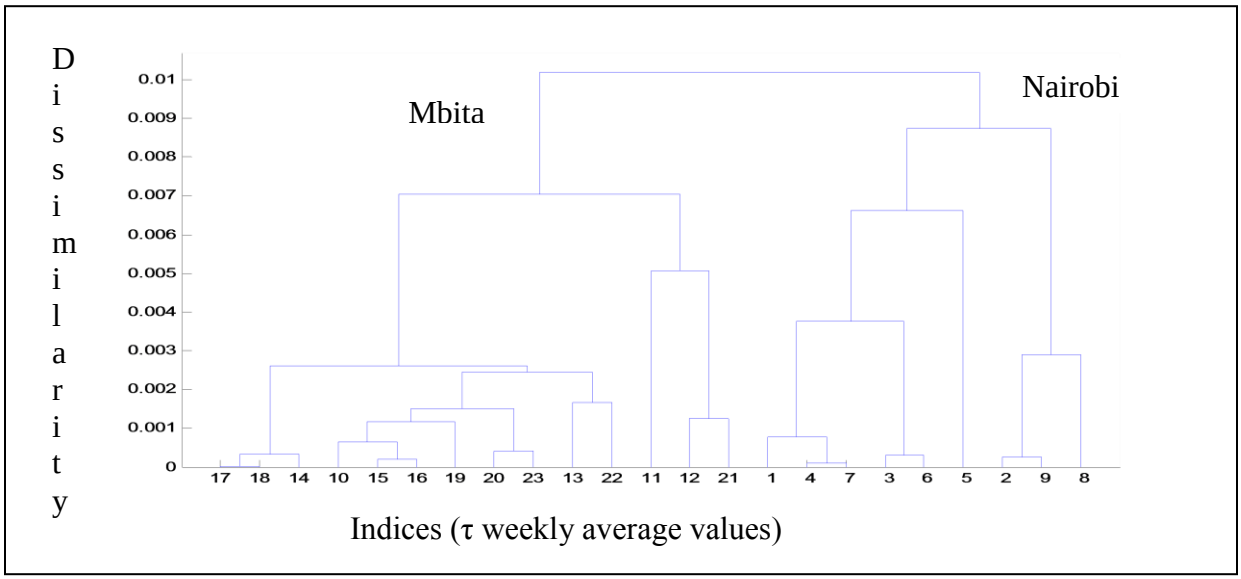

Figure 5.11: Spatial characterization of 23 weekly average τ from Nairobi and Mbita for 1020 nm aerosol size fraction (October-December 2007).

From Figure 5.11, we note that the 1020 nm size aerosol particles dominating Mbita may be attributed to both pollen grains from maturing plants of different types and dust lifting prevalent. Various sub-clusters in the main cluster (17-21) may be due to variation in relative humidity. Sub-cluster 11-21 corresponds to week number W37 and W38 that are known to be dominated by biogenic aerosols from maturing plants and harvesting time over the site. Sub-clusters 10-23, 13-22 and 17-14 can be attributed respectively to dust loading as modulated by RH. The 17-14 sub-cluster corresponds to week number W40, W43 and W44 that seem to be altered by temperature averaged at 23.61℃ (Table 7.2: Appendix) that enhances dust loading. The aging of smoke particles is accompanied by their size transformations in addition to coagulation and condensation processes that might be the reason for sub-cluster 10-22. On the other hand, construction activities prevalent over Nairobi can be the reason the sub-cluster 2-9 that enhance

dust loading. Coagulation and condensation processes may lead to significant relative humidity over Nairobi of about 77.75 % during the time interval. This might be the reason to sub-clusters 1-7, 3-6 and 5 for accumulation mode aerosol particles originating from both vehicle and industrial emissions dominating the Nairobi atmosphere.

Figure 5.12 below shows a dendrogram for 23 weekly τ averages for 440 nm wavelength channel over Nairobi and Mbita (October-December 2007)

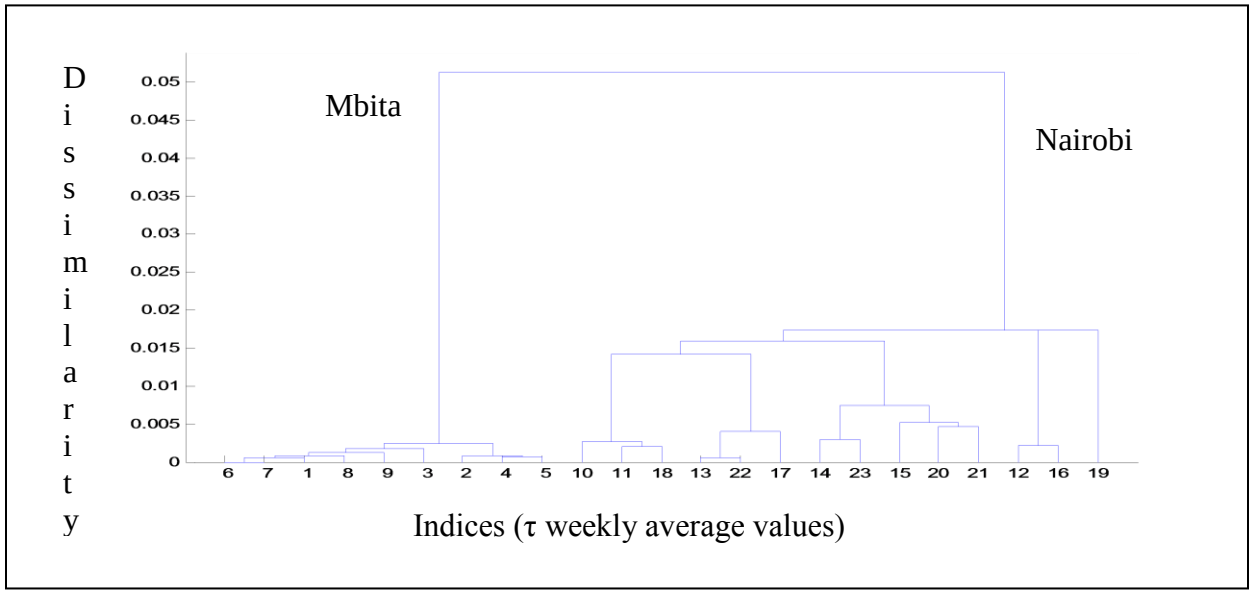

Figure 5.12: Spatial characterization of 23 weekly average τ from Nairobi and Mbita for 440 nm aerosol size fraction (October-December 2007).

Differences in the levels of aging processes in the smoke particles can be attributed to sub-cluster 6-3 (for aging smoke particles) and sub-cluster 2-5, corresponding to fresh smoke particles characterized by low temperature (22.42℃) and lack of rain over Mbita (Figure 5.12). On the other hand, the chemical content i.e. sulfate and nitrate dominated aerosols from industrial emissions respond differently to the same amount of relative humidity (65.67 %) as seen in Table 7.2: Appendix over Nairobi. This greatly modulates the formation of this sub-cluster (12-19) of aerosol in the particle size regime. Vehicle emissions depending on the type of fuel used might be the reason to sub-clusters 10-18, 13-17, 14-23 and 15-21 while those aerosol particles originating from industrial emissions might be the reason to sub-clusters 12-16 and 19.

5.1.2.2 Spatial Variation Between Nairobi and Malindi

Weekly τ averages for Nairobi and Malindi (March-May 2008) are displayed in dendrograms for all possible wavelength channels. Figure 5.13 is a dendrogram for this variation in 675 nm wavelength channel.

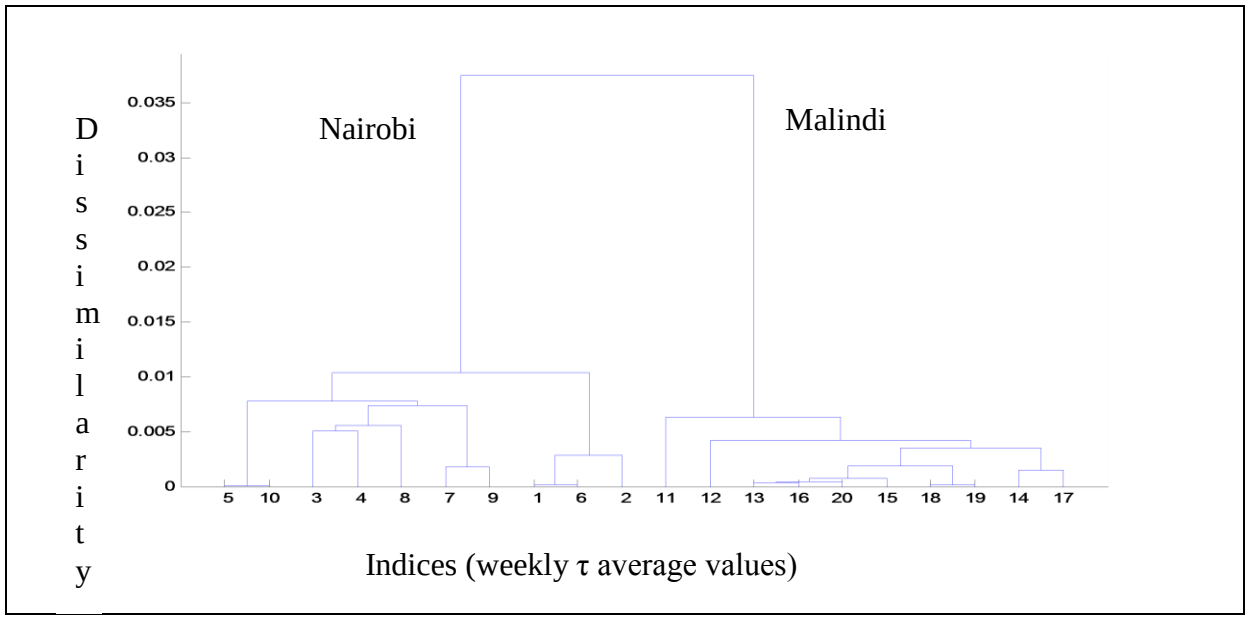

Figure 5.13: Spatial characterization of 20 weekly average τ from Nairobi and Malindi for 675 nm aerosol size fraction (March-May 2008).

The dendrogram in Figure 5.13 reveals that the spatial variation in the weekly τ average values is also divided into two main clusters i.e. cluster 1-10 corresponding to Nairobi while cluster 11-20 corresponds to Malindi. Basically, these two distinct groups between the sites correspond to variation in aerosol burden, mode of formation and chemical characteristics with their responses to the variation in relative humidity. For Malindi in this aerosol particle size, we note sub-clusters 14-17, 18-19, 13-15, 12 and 11 are modulated by the chemical characteristics of sea spray sea salt aerosol particles as influenced by variation in relative humidity over the site. On the other hand, Nairobi is characterized by sub-clusters 5-10, 3-8 and 7-9 that are modulated by the different types of fuels used that alter the chemical composition of both black and organic aerosol particles from vehicle emissions which respond differently to a variation in relative humidity. Sub-cluster 1-6 and 2 correspond to sulfate and nitrate dominated aerosol particles may be as result of industrial emissions.

5.1.3 Spectral Dependence of Aerosol Optical Depth

In order to study the spectral dependence in τ, the annual averages of τ for each site and year were obtained. The graphs of annual τ values verses wavelength channels (aerosol sizes) were plotted as indicated in Figure 5.14a-c below.

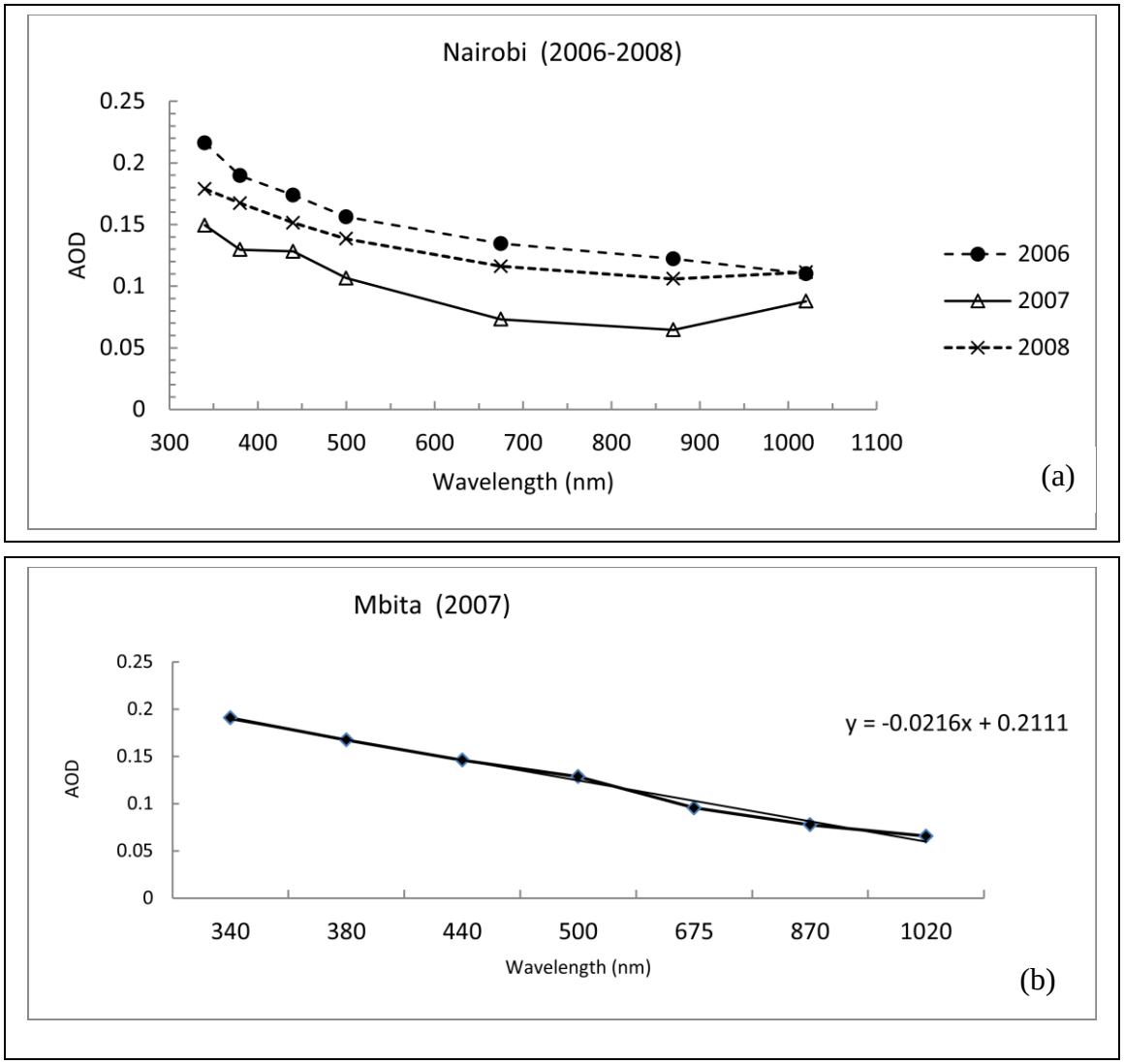

Figure 5.14: Spectral dependence of τ over (a) Nairobi and (b) Mbita in their respective years.

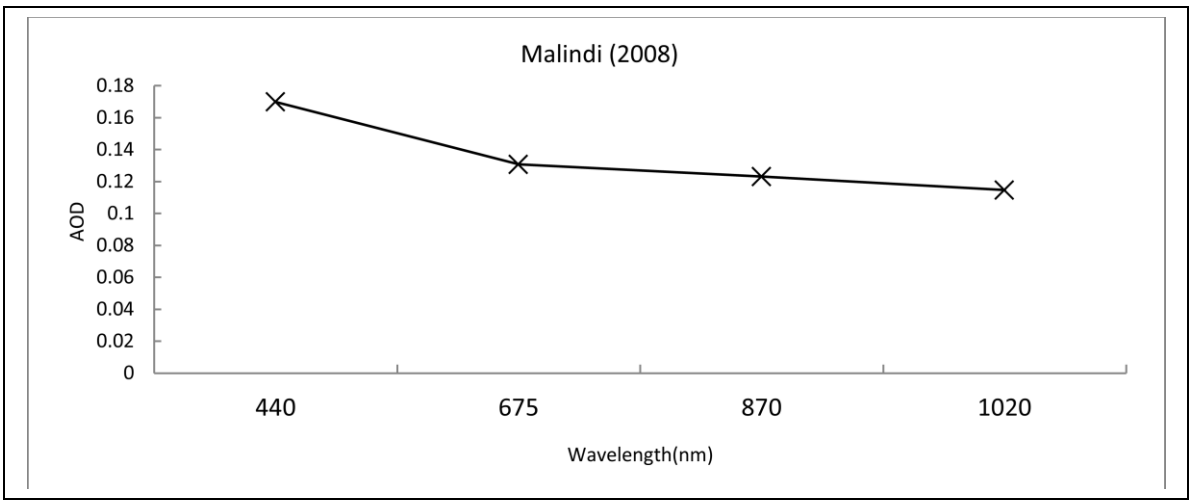

Figure 5.14c: Spectral dependence of τ over Malindi in 2008.

It is evident from Figure 5.14a-c that there is relatively strong dependence of τ on aerosol particle size (λ) for the smaller aerosol particle sizes as compared to larger particles [Eck *et. al.*, 1998]. This can be attributed to the presence of high aerosol number densities in the fine aerosol particles mode, hence the high τ values. These are known to selectively scatter the incoming solar radiation as compared to large sized particles that are known to absorb the incoming solar radiation. Figure 5.14a for Nairobi reveals an annual evolution in the spectral characteristics of τ which could be influenced by amount of rainfall which alters aerosol number densities by actively removing aerosol particles from the atmosphere through washout as noted from Table 7.1: Appendix. Significant aerosol number densities (Table 5.6) in short wavelengths from both vehicle and industrial emissions have higher τ values. We note a significant curvature in the series over Nairobi in 2007, which may be attributed to less amount of rainfall received as shown in Table 7.1: Appendix.

Local air circulation effects between Mbita and Lake Victoria may explain the almost linear spectral variation in τ is noted in Figure 5.14b over the site. An almost linear spectral variation in τ is also noted over Malindi in 2008. Thus we conclude that spectral variation in τ is dependent on aerosol mode of formation, their characteristics e.g. hygroscopicity and also amount of rainfall received over the site. These characteristics are known to modulate aerosol optical depth [Shettle and Fenn, 1979].

5.2 Angstrom Exponent (α)

5.2.1 Temporal Characteristics of Angstrom Exponent

Angstrom exponent (α) is related to size distribution of aerosol particles and it can also be used as a measure spectral dependence of τ when using the Ångström formula [Ångström, 1961]. Temporal variation of α over the three sites was probed using PLS-DA and PCR to validate each other. The two techniques were in agreement, revealing two significant PCs i.e. PC1 representing the hygroscopic aerosol particles as influenced by relative humidity (RH) while PC2 represents aerosol mode of generation as modulated by temperature. RH promotes coagulation and condensation processes not only for hygroscopic aerosol particles but also for mixtures containing non-hygroscopic aerosol particles e.g. organic and black carbon hence transforming their sizes. High temperature promotes photochemical processes through gas-to-particle conversion processes especially in heavily industrialized urban sites which in turn promote accumulation mode aerosol particles. Temporal classification of α also depends on rain and which regulates RH in the atmosphere through surface evaporation. The seasonal variation in α is indicated by the score plot for 440-675 nm wavelength pair for all the sites in Figure 5.15 as predicted by PLS-DA which was similar to that of PCR.

(a)

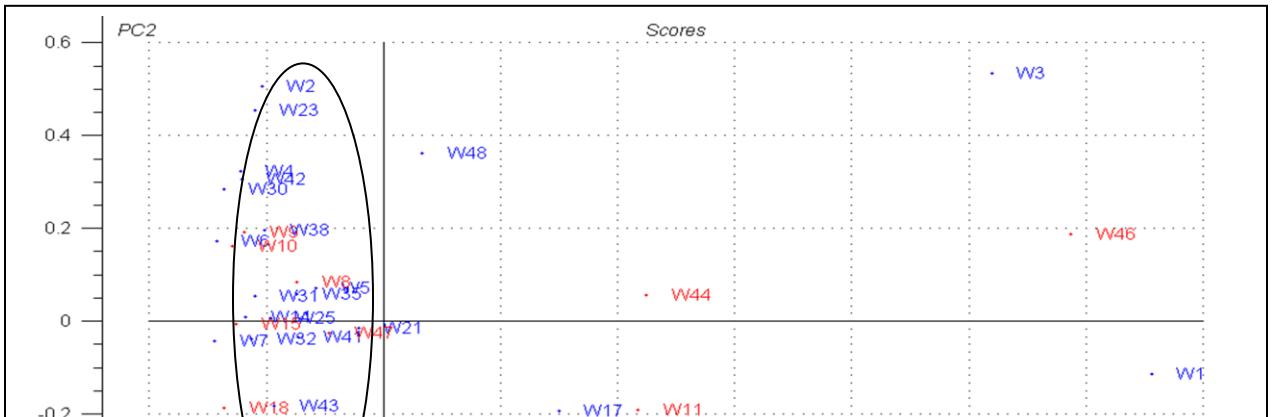

(b)

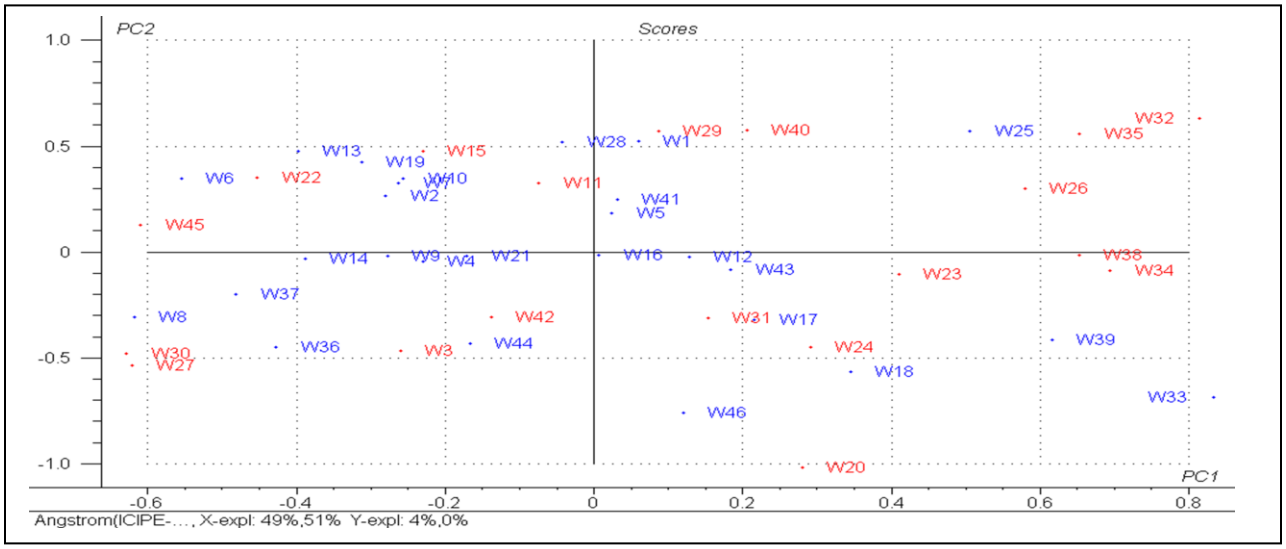
PC2
Scores
PC1
Angstrom(ICIPE-..., X-expl: 49%,51% Y-expl: 4%,0%

(c)

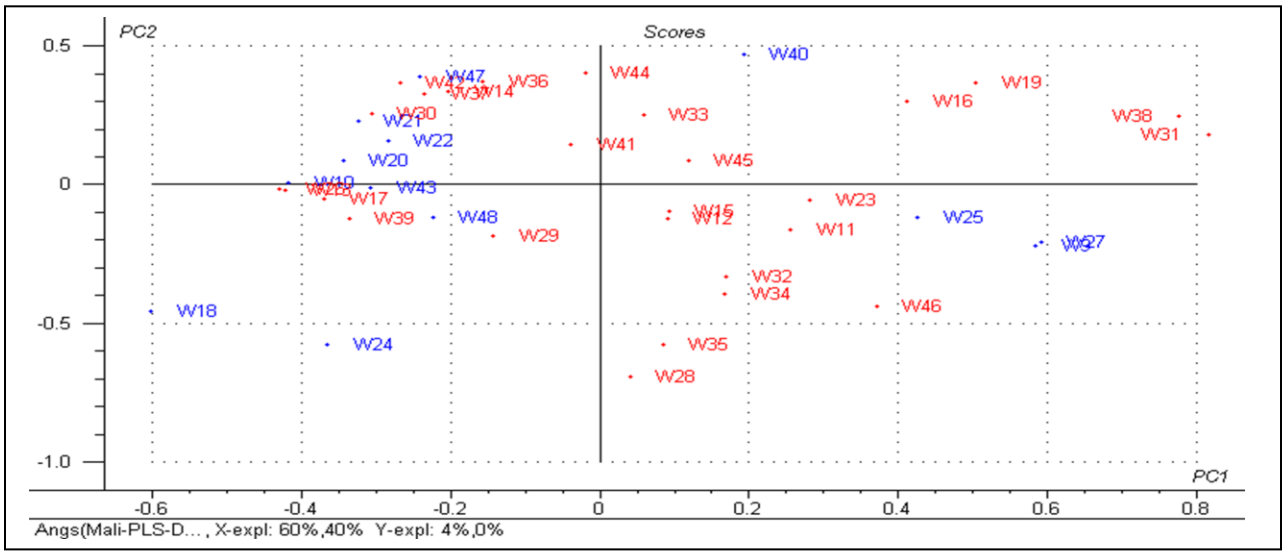
PC2
Scores
PC1
Angs(Mali-PLS-D..., X-expl: 60%,40% Y-expl: 4%,0%

Figure 5.15: Example of plot of scores with X and Y loadings for 48 samples of the PLS-DA model at 440-675 nm wavelength pair over (a) Nairobi (2006), (b) Mbita, (c) Malindi.

Aerosol particle size distribution over the three sites is heavily dependent on both RH and temperature as indicated in the score plots for α values in Figure 5.15a-c. Rainfall episodes over the study sites aid in altering RH but do not directly affect aerosol size transformations processes. Figure 5.15a reveals variation in aerosol size transformations in the 440-675 nm wavelength pair over Nairobi whereby RH and temperature accounts for 77 % and 23 % of the explained variance respectively. The weekly averages (W5, W7, W8, W21, W24, W25, W31, W32, W35 and W47 as shown in Figure 5.15a) are characterized by a low weekly total rainfall average (13.65 mm) and relatively high temperature (21.49℃). This modulates RH through surface evaporation hence aerosol size transformations probably through coagulation and condensation processes. Temperature influences on aerosol number densities through photochemical processes are inhibited slightly due to low temperatures of an average (17.75 ℃) as observed in week number W16, W18, W19, W20, W22, W24, W39 and W45 (Table 7.2: Appendix). RH modifies α not only for hygroscopic aerosol particles but also for mixtures containing non-hygroscopic aerosol particles e.g. organic and black carbon, thus, transforming their sizes by wetting the particles hence altering their effective radius.

Significant variation in α as indicated by both RH and temperature is similar as seen in the explained variance for Figure 5.15b-c over Mbita and Malindi respectively. Local air circulation between Mbita and Malindi from Lake Victoria and the Indian Ocean respectively aid in aerosol transportation and size transformations. A summary of the explained variance for the two PCs over the study sites in all the possible wavelength pairs is indicated in Table 5.2.

Table 5.2: Comparison of variation characteristics in α at different sites and wavelength pairs values using both PLS-DA and PCR.

Site	Method	Explained variance for PC1 and PC2 in % Wavelength ranges (nm)									
		340-440		380-500		440-675		440-870		500-870	
		PC1	PC2	PC1	PC2	PC1	PC2	PC1	PC2	PC1	PC2

Nairobi (2006)	PLS-DA	46	54	59	41	77	23	74	26	77	23
	PCR	55	45	64	36	77	23	75	25	78	22
Mbita (2007)	PLS-DA	58	42	53	47	49	51	50	50	50	50
	PCR	59	41	56	44	54	46	53	47	51	49
Malindi (2008)	PLS-DA					60	40	56	44	54	46
	PCR					67	33	64	36	55	45

Influence of RH on α is dependent on chemical composition of aerosol particles which in turn determines whether the particle is behaving as hygroscopic or non-hygroscopic. On the other hand, temperature alters aerosol number density particularly for urban environments through photochemical processes due to industrial emissions, since aerosol particles produced through photochemical process dominate the accumulation mode aerosol particles. They are known to be sensitive to aerosol size transformations through coagulation and condensation processes. For Mbita, we note that RH influence on α is slightly higher in the 340-440 nm wavelength pair and remains relatively constant for the rest of other wavelength pairs. This shows that the α wavelength pair 340-440 nm is more sensitive to aerosol size transformations as influenced by RH as compared to the longer wavelength pairs. The aging process of biomass burning aerosol particles in the shorter wavelength pairs is accompanied by their size transformations due to their hygroscopic characteristics, which are influenced by RH through coagulation and condensation processes. A close agreement between PLS-DA and PCR as techniques used in probing the size transformations and distributions over the study sites was noted.

Aerosol particles of hygroscopic and water-soluble nature from maritime conditions over Malindi undergo coagulation and condensation processes as a result of RH. This alters their sizes since RH enhances growth in their effective radius, thus, explaining the significant variation for α in the shorter wavelength pair i.e. 440-675 nm. The hygroscopic properties of sea salt and sea spray aerosol particles arising from maritime conditions over the site are controlled by aerosol mixture composition. Thus, it was noted that size transformations as caused by RH are of a lesser degree as compared to that caused by differences in aerosol mixing. Influences of RH decline with increasing wavelength pairs over the site; hence aerosol particles in 440-675 nm wavelength

pair are sensitive to their size transformations as compared to those in the longer wavelength pairs.

5.2.2 Spatial Characteristics of Angstrom Exponent

Spatial characteristics in α was probed in the same time intervals to that of τ using the HCA technique in the wavelength pair 440-675 nm. Significant variations in aerosol size transformations were noted in this wavelength pair. These variations are as indicated in Figure 5.16a and b between Nairobi and Mbita and Nairobi and Malindi respectively.

(a)

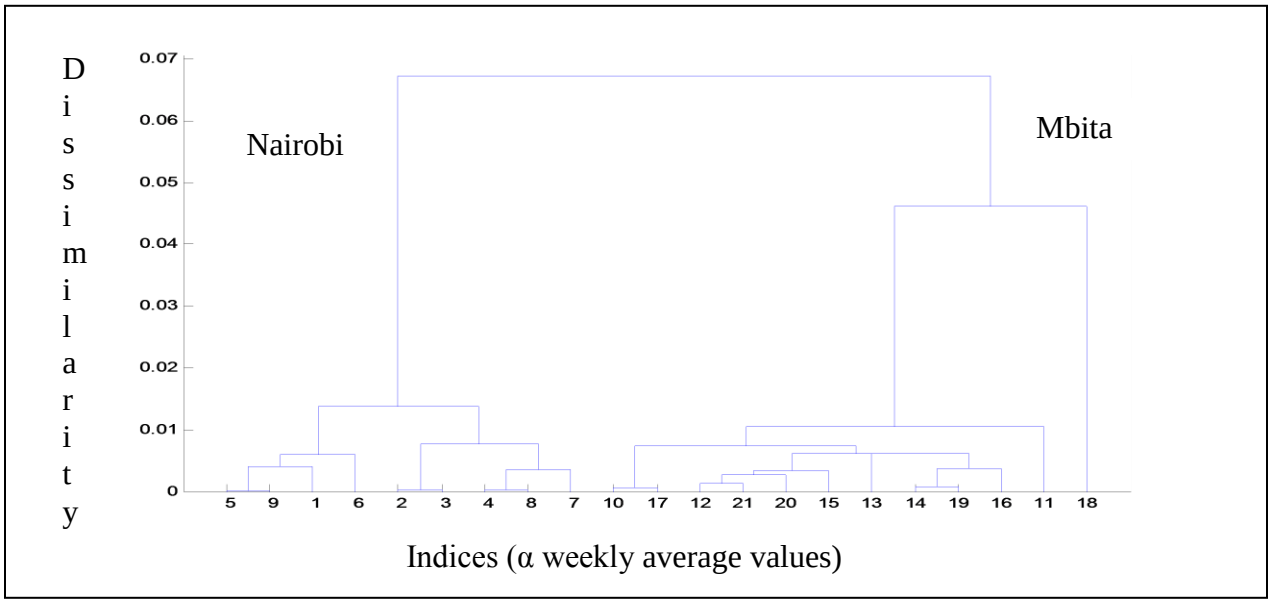

(b)

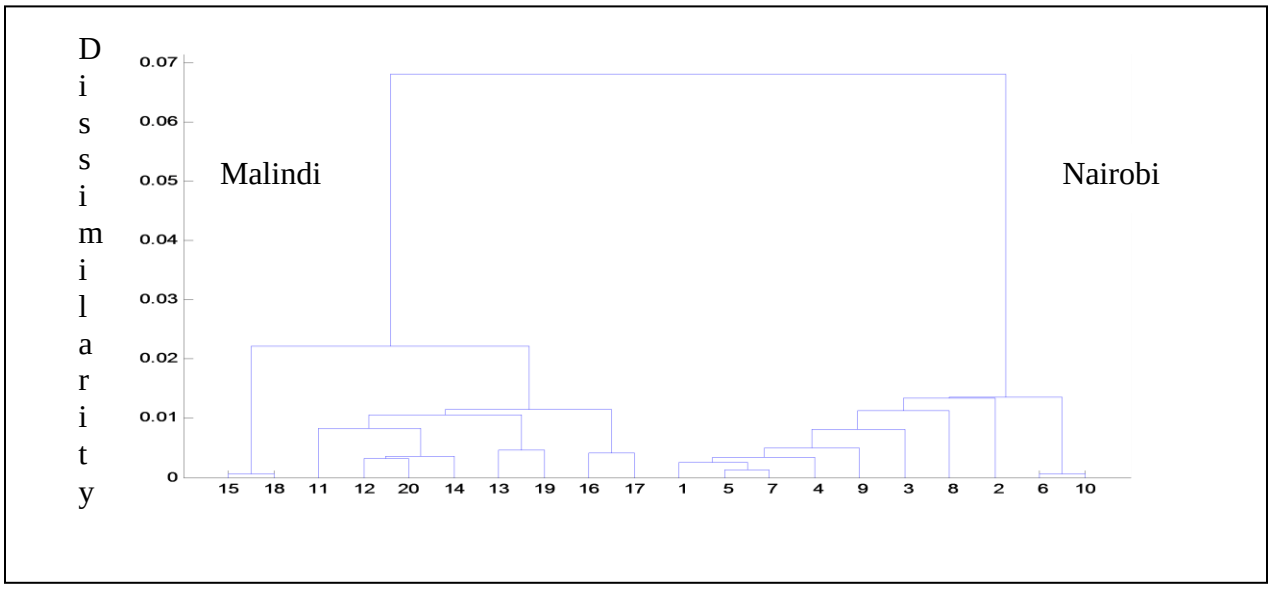

Figure 5.16: Spatial variation for weekly α average in the 440-675 nm wavelength pair over (a) Nairobi and Mbita (October-December 2007) and (b) Nairobi and Malindi (March-May 2008)

Spatial variations in α as indicated in the dendrograms in Figure 5.16 are attributed to variations in RH and aerosol mixture composition which affect aerosol size transformations. For Nairobi and Mbita (Figure 5.16a), aerosol particles of anthropogenic origin may be the reason for the observed spatial variations i.e. Nairobi is likely to be dominated by both black and organic carbon particles from vehicular emissions (5-6) and sulfates and nitrate dominated particles from industrial effluents (2-7). Both nitrate (2-2) and sulfate (4-7) dominated aerosol particles are of hygroscopic nature; that explains the variation in α due to changes in RH over Nairobi. On the other hand, Mbita is dominated by biomass burning aerosol particles whose aging processes is accompanied by their growth thus increasing in size due to their equally hygroscopic nature. This explains the sub clusters (10-11); they correspond to aerosol smoke particles that are at different stages of the aging processes.

Indices (α weekly average values)

Likewise, maritime aerosol particles composed of mostly sea salt and sea spray are also of hygroscopic nature and they mix up and thus absorb the RH in the atmosphere hence the observable spatial variations in the dendrogram in Figure 5.16b. Malindi corresponds to a main cluster (15-17) while that of Nairobi corresponds to (1-10) cluster. Various sub clusters within the main cluster over Malindi can be due to variations in aerosol composition of maritime aerosol particles which alters their size transformations. It is therefore important to note that aerosol characteristics i.e. aerosol mixture composition, hygroscopic property and their mode of generation explain the spatial variation between Nairobi (1 to 10 cluster) and Malindi (15-17) as shown in Figure 5.16b.

5.3 Relative Validation of AERONET τ and α Data

τ and α annual average values as determined by AERONET sun spectrophotometry over the study sites were compared with MODIS measurements from the average values on both Terra and Aqua satellites for validation. The degree of resolutions stated in Section 4.3 covers each

AERONET site, thus, average values between Nairobi and Mbita for τ (AERONET site for Malindi lacks the 500 nm wavelength channel data) and that of α for the three sites were used in validation. This was accomplished by using AERONET τ at 500 nm and α at 440-675 nm and MODIS τ data at 550 nm and α at 470-660 nm since this were the closest wavelength channels available. τ and α average values for the entire period of study as determined by both AERONET and MODIS together with percentage variations were obtained.

The τ value for both AERONET and MODIS satellite data was found to be 0.129 and 0.145 respectively (with a percentage variation of 12.4 %) while that of α as determined by AERONET and MODIS was found to be 0.798 and 0.885 respectively (with a percentage variation of 10.9 %).

The level of agreement for τ was well within the expected uncertainty of about 10 % over West Africa during the Dust and Biomass-burning Experiment [Johnson *et. al.,* 2009], given the difficulty in retrieving aerosol optical properties due to the variation in land cover over the study sites. Aerosol variability in their mixing and density together with sampling differences may also be attributed to the slight variation in the two modes of remote sensing for τ. On the other hand, slight variation in α is mostly likely due to lack of sufficient mixtures of aerosol particles dominating the area of consideration in the parameters retrieving algorithm.

5.4 Single Scattering Albedo

Single scattering albedo (ω) estimates the magnitude and sign of the radiative forcing due to atmospheric aerosols. ω of 1 implies aerosol particle extinction of the incoming solar radiation due to scattering whose impact on radiative forcing is negative; conversely, ω of zero implies aerosol particle extinction due to absorption which impacts positively on the radiative forcing. Annual ω averages (at zero SZA) for the three sites at their respective times are shown in Table 5.3 below.

Table 5.3: Annual ω averages (at zero SZA)

Site	Year	440 nm	675 nm	870 nm	1020 nm
Nairobi	2006	0.54	0.52	0.52	0.52

	2007	0.53	0.52	0.53	0.53
	2008	0.58	0.58	0.58	0.58
Mbita	2007	0.58	0.57	0.57	0.57
Malindi	2008	0.51	0.49	0.49	0.50

It was noted that there is no significant spectral dependence in ω over the study sites. Nairobi has an annual percentage increase of 11.5 % across all wavelength channels except for λ = 440 nm (7.8 %) from 2006 to 2008. This suggests increasing aerosol number densities of sulfate and nitrate dominated aerosol particles as a result of industrial emissions through photochemical processes that are known to scatter the incoming solar radiation. Aerosol scattering of the incoming solar radiation impacts negatively on the radiative forcing thus cooling the earth's surface. Effects of mixing for both sulfate and nitrate dominated aerosols and both black and organic carbon aerosol particles due to vehicular emissions may explain the low observed ω values at zero SZA. Local air circulation over Mbita and the effect of biomass burning aerosol particles that evolves in size due to their hygroscopic property. These aerosol particles absorb the incoming solar radiation, which explains why the low ω values as compared to those of Nairobi. Higher influence of anthropogenic aerosol particles which are known to scatter the incoming solar radiation explains why Nairobi has higher ω values as compared to that of Malindi in 2008 across all wavelength channels.

5.5 Asymmetric Factor

Asymmetric factor (g) is commonly used to describe the angular distribution of scattered light in radiative transfer models. When g approaches +1, scattering is peaked in the forward direction while when it approaches -1 then scattering is peaked in the backward direction. For $g = 0$, scattering of radiation by aerosol particles is isotropic. The annual averages of the asymmetric factor are indicated in Table 5.4 below.

Table 5.4: Annual and spatial variation of the asymmetric factor

Site	Year	440 nm	675 nm	870 nm	1020 nm
Nairobi	2006	0.48	0.46	0.46	0.46

	2007	0.48	0.46	0.46	0.46
	2008	0.48	0.49	0.47	0.47
Mbita	2007	0.45	0.41	0.40	0.40
Malindi	2008	0.47	0.45	0.45	0.46

From Table 5.4 above, we note constant g values over Nairobi in the 440 nm wavelength channel while 870 nm and 1020 nm channels reveal a 2.2 % increase from 2006 to 2008. A 6.5 % increase in g values in the 675 nm wavelength channel is noted over the same period. This significant increase in the 675 nm wavelength channel is attributed to increasing scattering of the incoming solar radiation in the forward direction over Nairobi. As noted over Nairobi, g values tend more to zero rather than unit in any wavelength channel, this suggests an isotropic form of scattering of solar radiation by aerosol particles of different sizes.

Mbita shows a decline in scattering (at zero SZA) of the incoming solar radiation with increasing aerosol particle sizes. Thus, absorption of the incoming solar radiation due to mineral dust and biomass burning aerosol particles dominates the site. Mbita has lower g values as compared to that of Nairobi in 2007 across all the wavelength channels. This shows that the site is mainly dominated by aerosol particles that absorb rather than scatter the incoming solar radiation. For Nairobi, there is no significant variation in forward scattering of the incoming solar radiation with aerosol particles sizes. This can be as a result of aerosol composition that alters their scattering properties irrespective of their sizes. Influences of aerosol composition originating from sea spray and sea salt maritime conditions might be the reason for the enhanced g values as compared to that of Mbita though in different years.

5.6 Refractive Index

The complex refractive index over the three sites is summarized in Table 5.5 below showing variation in both real and imaginary parts.

Table 5.5: Annual averages of complex refractive indices

Site	Year	440 nm	675 nm	870 nm	1020 nm

Nairobi	2006	1.56+i0.042	1.56+i0.042	1.57+i0.042	1.57+i0.040
	2007	1.54+i0.035	1.54+i0.029	1.55+i0.026	1.56+i0.026
	2008	1.54+i0.032	1.54+i0.035	1.54+i0.035	1.54+i0.033
Mbita	2007	1.51+i0.012	1.52+i0.012	1.60+i0.004	1.53+i0.011
Malindi	2008	1.54+i0.051	1.55+i0.056	1.55+i0.049	1.55+i0.051

Annual real refractive index (n) for both Nairobi and Malindi in 2008 is almost equal, while the imaginary refractive index (k) for the later is higher as compared to that of Nairobi. This means that solar radiation by scattering aerosols based on the chemical composition is the same for both Malindi and Nairobi in 2008 and is independent of aerosol particle size. For Nairobi, this dominant aerosol composition species has been decreasing over the years 2006-2008, again independent of aerosol particle size. Absorption properties of aerosols dominating Malindi seems to be far pronounced as compared to that of Nairobi in the same year. This can be as a result of hygroscopic nature of maritime aerosol particles i.e. sea salt and sea spray that evolve in their sizes thus absorbing the incoming solar radiation. There is a drop in imaginary index values from 2006 to 2008 over Nairobi in 440 nm wavelength channel which can be attributed to a drop in the aerosol number densities of absorbing aerosols due to rainfall washout (see Table 7.2: Appendix). The effect of local air circulation and biomass burning over Mbita produces smoke aerosols particle which evolve in size with age, causing the low k value of 0.012 as compared to other sites across all wavelength channels.

5.7 Physico-Chemical Properties

Physico-chemical properties of aerosol particles alter radiative characteristics of an atmosphere when their chemical composition and sizes in the atmosphere change. These two characteristics depent on aerosol generational processes, origin and influences from meteorological parameters. Aerosol number densities can be derived from the AERONET aerosol optical properties i.e. aerosol optical depth and extinction cross section over the three sites of study as summarized in Table 5.6.

5.7.1 Flux Loss

Extinction cross section is a fraction of radiant flux lost from a collimated solar radiation beam per unit area of aerosol due to the aerosol extinction characteristics. From basic principles, extinction cross section (δ_e) is determined from aerosol particle size using equation 3.4. It is assumed that the efficiency with which the radiation in the atmosphere interacts with aerosol particles is unit and is a function of radius of aerosol particles, wavelength and complex refractive index of the incoming solar radiation i.e. $Q_{s,a,e}(r, m, \lambda) = 1$. The δ_e for the three sites at 340 nm, 380 nm, 440 nm, 500 nm, 675 nm, 870 nm and 1020 nm wavelength channels were found to be 9.08×10^{-10} cm^2, 1.13×10^{-9} cm^2, 1.52×10^{-9} cm^2, 1.96×10^{-9} cm^2, 3.58×10^{-9} cm^2, 5.94×10^{-9} cm^2 and 8.17×10^{-9} cm^2 respectively; these are plotted in Figure 5.17.

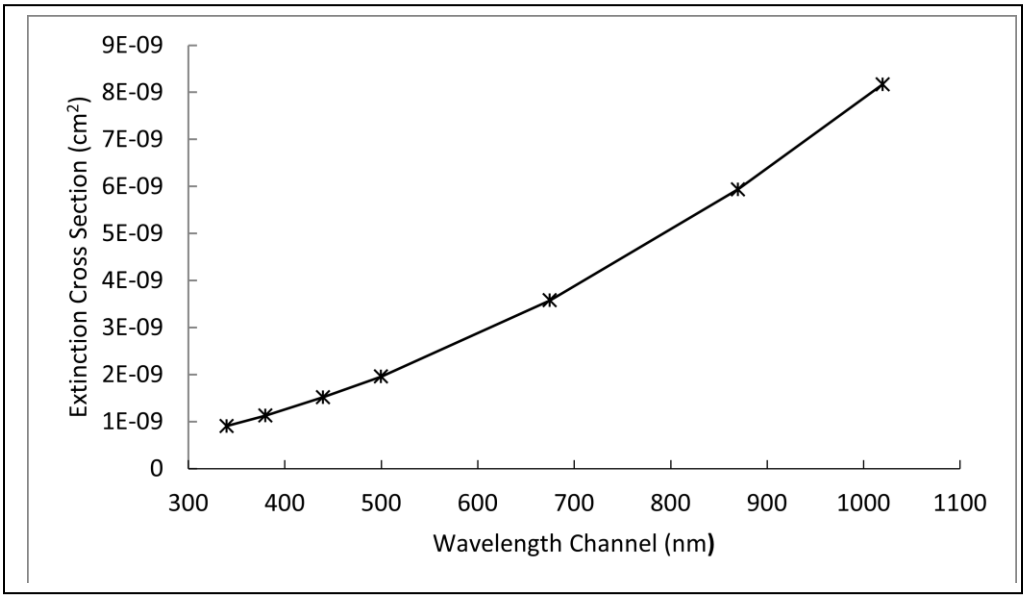

Figure 5.17: Extinction cross section as a function of wavelength channels over the study sites

There is an increasing extinction cross section with aerosol particle size. This signifies an increase in the fraction of radiant flux lost with increasing aerosol particle size in the atmosphere. Low radiant flux lost in the UV regime is attributed to the fact that most of the incoming solar radiation in these aerosol particle sizes is already absorbed by the ozone and other atmospheric constituents that limit its arrival in the troposphere and lastly on the Earth's surface. Increasing aerosol particle sizes in the visible and IR regimes act as good scatterers and absorbers (depending on the aerosol particle composition) of the incoming solar radiation. This explains

the reason why we note higher δ_e particularly in the visible and IR aerosol particle sizes as compared to that of UV aerosol regime.

5.7.2 Aerosol Number Density

Aerosol number densities (N) over the three study sites were determined using τ annual averages with the extinction cross section at all possible wavelength channels as shown in equation 3.5. Aerosol number density (N) for the various aerosol particle sizes are shown in Table 5.6.

Table 5.6: Average aerosol number density distribution over the study sites.

Site	Year	Average aerosol Number Density (N) × 10^7/cm^3						
		340 nm	380 nm	440 nm	500 nm	675 nm	870 nm	1020nm
Nairobi	2006	16.24	11.89	8.35	6.88	1.97	1.02	1.10
	2007	24.58	16.52	11.55	8.16	3.63	2.02	1.35
	2008	19.81	15.04	9.87	7.14	3.35	1.85	1.35
Mbita	2007	24.22	16.86	11.23	8.67	3.97	1.52	0.98
Malindi	2008			13.8		4.47	2.53	1.71

An appreciable variation in the aerosol number densities is noted over Nairobi dominated by aerosol particles in the 675 nm and 870 nm as a consequence of industrial and vehicular emissions. A significant aerosol number density increase of 45.7 % and 49.5 % in both 675 nm and 870 nm wavelength channels respectively is noted from 2006-2007. This is as a result of decrease in the total amount of rainfall received (of about 13.8 %). This limits aerosol removal processes through washout between 2006-2007 (see Table 7.1: Appendix). A decrease of 7.7 % and 54 % in the same wavelength channels is revealed between 2007-2008 periods, this is attributed to an increase of about 14.1 % of rainfall received over Nairobi in the same period.

Thus, it was noted that aerosol wet removal processes through washout explains variations in aerosol number densities observed in Table 5.6 over Nairobi. An average increase in aerosol number density for all the remaining wavelength channels was 22.1 % from 2006-2007 and drops by 20.9 % from 2007-2008. Mbita has higher aerosol number densities across wavelength

channels than that of Nairobi in 2007, this may be due to local air circulation, biomass burning, biogenic influences and dust loading activities prevalent in the area. On the other hand, Malindi has the highest aerosol number densities across all common wavelength channels (in 2008) as a result of local air circulation and long distance transport of fine aerosol particles by Monsoon winds from Arabian Indian desert.

5.8 Radiative Characteristics of Atmospheric Aerosols

Radiative characterization of atmospheric aerosols over Nairobi, Mbita and Malindi were performed using the COART model on assumption of a clear sky composed of aerosols only. The atmospheric profile utilized in this model for all the three sites was tropical with a boundary layer aerosol model of MODRAN urban, MODRAN rural and MODRAN maritime for Nairobi, Mbita and Malindi respectively. The total aerosol loading was confined by a visibility of 23.0 km with a land surface albedo of 0.1 which represents the average distribution of vegetation cover in most land cases. Spectral irradiances i.e. up and down (at λ = 440 nm, 675 nm, 870 nm and 1020 nm), integrated fluxes (λ from 440 nm to 1020 nm) and the reflectance at Solar Zenith Angles (SZAs) ranging from 0^0 to 80^0 in steps of 10 degrees were determined at 0 km and 12 km above sea level over the sites under consideration. The three aerosol radiative properties analyzed in this work are discussed below.

5.8.1 Spectral Irradiance ($E_o(z,\lambda)$)

Spectral irradiance ($E_o(z,\lambda)$) is the power density of the solar radiant flux incident on the surface of an aerosol particle per unit wavelength. The variation in the calculated (according to the COART-model) spectral irradiance with SZAs for the three sites is shown in Figure 5.18a-h. It had almost similar trends to those for Nairobi in 2008.

Down irradiance	Up irradiance

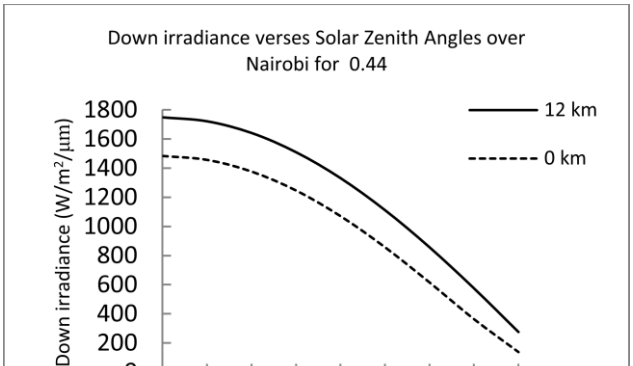

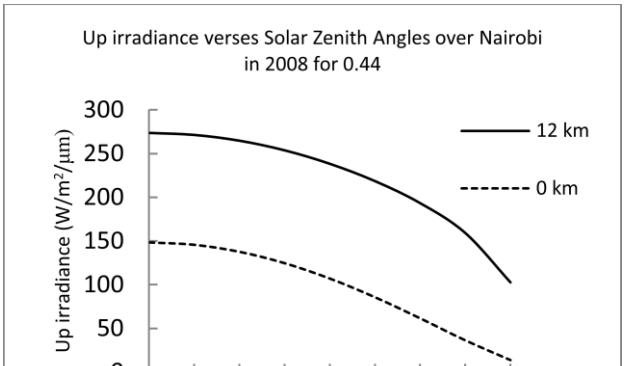

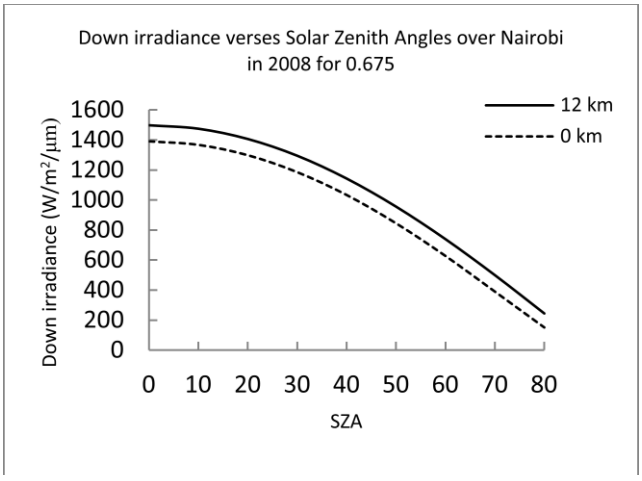
Down irradiance verses Solar Zenith Angles over Nairobi in 2008 for 0.675
Down irradiance (W/m²/μm)
SZA
12 km
0 km

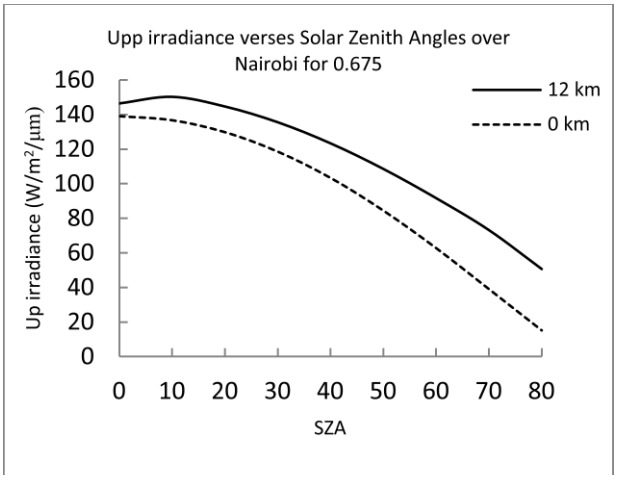
Upp irradiance verses Solar Zenith Angles over Nairobi for 0.675
Up irradiance (W/m²/μm)
SZA
12 km
0 km

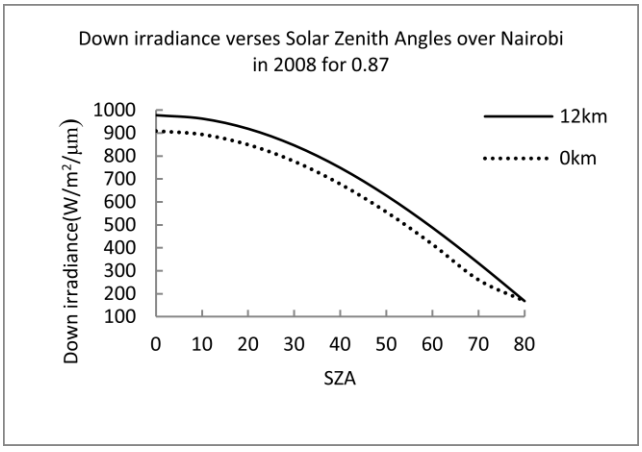
Down irradiance verses Solar Zenith Angles over Nairobi in 2008 for 0.87
Down irradiance(W/m²/μm)
SZA
12km
0km

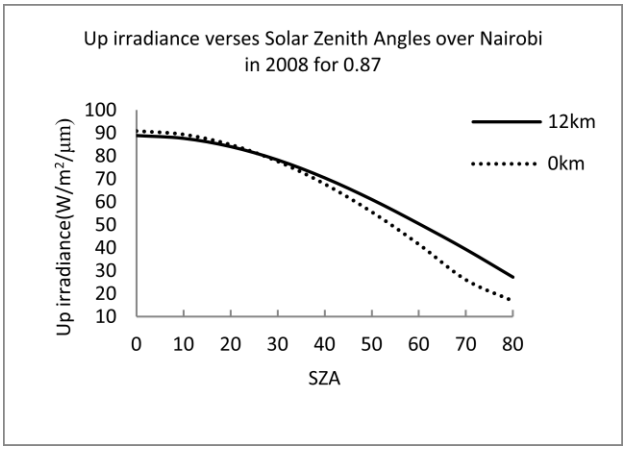
Up irradiance verses Solar Zenith Angles over Nairobi in 2008 for 0.87
Up irradiance(W/m²/μm)
SZA
12km
0km

e

f

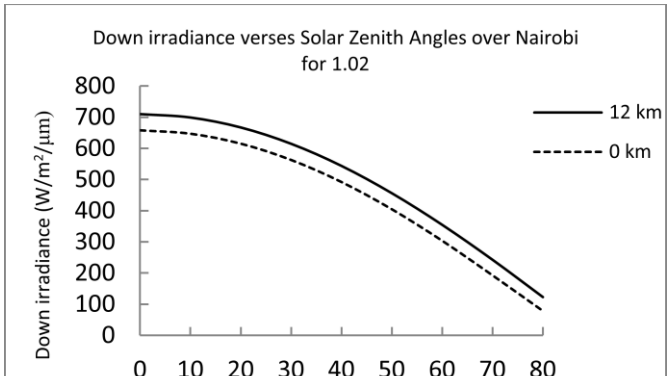
Down irradiance verses Solar Zenith Angles over Nairobi for 1.02
Down irradiance (W/m²/μm)
12 km
0 km

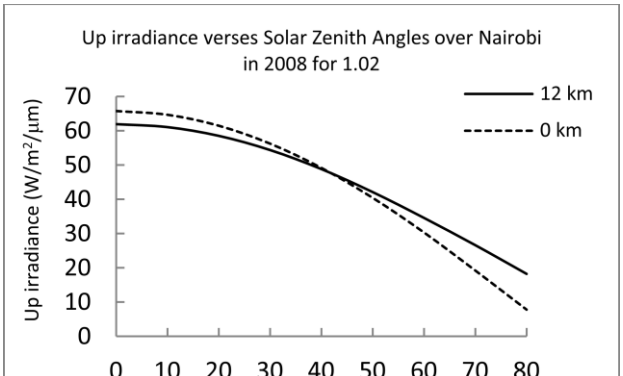
Up irradiance verses Solar Zenith Angles over Nairobi in 2008 for 1.02
Up irradiance (W/m²/μm)
12 km
0 km

Figure 5.18a-h: COART-modeled spectral irradiances (down and up) verses SZA at different wavelengths over Nairobi in 2008

A declining difference between downwelling irradiances with wavelength at 0 km and 12 km levels was noted. This suggests that absorption and scattering of radiation by aerosols at 12 km level is more dominant in the visible but reduces in the IR aerosol particle size regime. The decrease is more marked at larger SZA with the degree appearing to be independent of aerosol particle size. This is due to a uniform decrease in solar intensity at larger SZAs. There is a uniform variation of downwelling irradiance with SZA at all atmospheric levels. The low sun case (SZA 0^0 ~ SZA 20^0) is characterized by high downwelling irradiances since most of it is direct and strikes the surface at a glancing angle unlike in the high sun case (SZA 50^0 ~ SZA 80^0) where most of the downwelling irradiance is diffuse in nature hence the low spectral irradiance values [Zhonghai *et. al.,* 2006]. This then leads to a drop in downwelling irradiances reaching the earth's surface (0 km) which can still be attributed to increased absorption and scattering of the incoming solar radiation by aerosol particles of different sizes.

Figure 5.18b, d, f and h reveal that up irradiances in the atmosphere decrease with increasing SZAs across all the wavelength channels. This decrease is attributed to strong Fresnel reflection on the earth's surface (0 km) experienced by the incoming solar radiation. Figure 5.18f and h above correspond to λ = 870 nm and 1020 nm respectively. These two present a unique scenario where the radiant energy reflected into the atmosphere from the surface is slightly higher than that at 12 km level (SZA 0^0-SZA 20^0 and vice versa for SZA 40^0-SZA 80^0 for 870 nm and SZA 0^0-SZA 40^0 and vice versa for SZA 60^0-SZA 80^0 for 1020 nm). The point of intersection between the upwelling irradiances at the two atmospheric levels for both 870 nm and 1020 nm was at SZA 30^0 and SZA 50^0 respectively. This is a consequence of solar heating effect characteristic of the IR radiation in these wavelength channels. This effect accelerates dust loading through heating promoting absorption of both incoming and terrestrial solar radiation

causing the up irradiance at the surface to be more as compared to that at 12 km level for higher optical air mass factor values and vice versa for lower optical air mass factor values which translates to cooling effect on the surface.

The ratio of up/down irradiance for the net irradiance between 12 km and 0 km atmospheric levels for both down and up irradiances were determined. An increase in this ratio signifies an increase in radiant energy lost per unit surface area and vice versa in a given λ. This was done at specific wavelength channels i.e. 440 nm, 675 nm, 870 nm and 1020 nm and zero SZAs over the study sites as shown in Table 5.7.

Table 5.7: Net up and down irradiances various spectral ranges over study sites at zero SZAs

Site	Year	λ(nm)	Net down irradiance ($W/m^2/nm$)	Net up irradiance ($W/m^2/nm$)	Up/down
Nairobi	2006	440	291.56	138.81	0.4762
		675	119.84	15.62	0.1303
		870	56.61	5.89	0.1040
		1020	53.43	4.29	0.0803
	2007	440	224.45	109.62	0.4884
		675	74.54	10.36	0.1390
		870	53.60	9.60	0.1791
		1020	47.88	4.76	0.0994
	2008	440	265.06	125.35	0.4728
		675	107.35	13.05	0.1220
		870	50.13	4.43	0.0884
		1020	52.60	3.83	0.0737
Mbita	2007	440	274.67	125.58	0.4572
		675	106.36	24.34	0.2288
		870	53.48	2.76	0.0516
		1020	47.46	2.18	0.0459

Malindi	2008	440	306.78	120.63	0.3932
		675	129.56	22.44	0.1729
		870	68.84	7.98	0.1159
		1020	60.38	5.23	0.0866

A declining difference in both down and up irradiances with respect to aerosol particle size was noted between the 12 km and 0 km atmospheric levels for all years under consideration over the study sites. Thus, the radiant energy lost between the two atmospheric levels due to the presence aerosol particles declines with increasing aerosol particle size. This may be due to the heating effect of the incoming solar radiation which increases with wavelength. Variation in the ratio of the net up to down irradiance marches closely the variation in aerosol number density in a specific wavelength channel (see Table 5.6), which shows that aerosol particles of different sizes alter both up and down irradiance. An increase in aerosol number density between 2006-2007 across all wavelength channels is accompanied a percentage increase in the irradiance ratio by 2.6 %, 6.7 %, 7.2 % and 2.4 % for 440 nm, 675 nm, 870 nm and 1020 nm respectively. This signifies an increase in the radiant flux lost hence a cooling effect on the surface over Nairobi during the period.

There is a significant increase in the irradiance ratio for the 675 nm and 870 nm wavelength channels. This suggests that aerosol particles in these sizes dominate over Nairobi that may be as a result of both vehicular and industrial emissions. Hence, it was noted that a drop in aerosol number density affected the radiant solar energy during the period of study over Nairobi. On the other hand, a decrease in aerosol number density between 2007-2008 periods was accompanied by a decrease in the ratio by 2.7 %, 12.2 %, 50.6 % and 25.6 % for 440 nm, 675 nm, 870 nm and 1020 nm respectively. This suggests that changes in aerosol number density significantly affect radiant solar energy through either absorption or scattering of the incoming solar radiation. The loss of radiant solar energy as caused by aerosol particles is dominant in the 440 nm, 675 nm and 870 nm wavelength channels since most of aerosol particles from vehicle and industrial emissions dominate these aerosol particle sizes.

Comparison of the COART-modeled irradiance ratios was derived between Nairobi-Mbita and Nairobi-Malindi in 2007 and 2008 respectively. An insignificant variation in radiant flux lost was noted between Nairobi and Mbita across all wavelength channels except for that of 675 nm. Fresh smoke aerosol particles from biomass burning that correspond to the 675 nm wavelength channel might explain higher irradiance ratio of 0.2288 over Mbita as compared to that of 0.1390 for Nairobi (see Table 5.7). On the other hand, irradiance ratios for Malindi remain high as compared to that of Nairobi across all wavelength channels except for 440 nm channel. The loss in the radiant flux energy due to aerosol particles in these sizes is as a result of both sea spray and sea salt aerosol particles that absorb or scatter incoming solar radiation. These aerosol particle sizes dominate over Malindi due to the prevailing maritime conditions.

5.8.2 Integrated Fluxes

Integrated Fluxes (IF) corresponds to the integration of spectral irradiance over the entire spectrum arriving at the top of the terrestrial atmosphere. IF was determined between the spectral range 440-1020 nm with a spectral resolution of 10 nm using the COART model with similar settings as those used for the determination of the spectral irradiance. The variation of down and up integrated fluxes over the study sites was similar to that of Nairobi in 2008 with optical air masses are as shown in Figure 5.19a and b respectively.

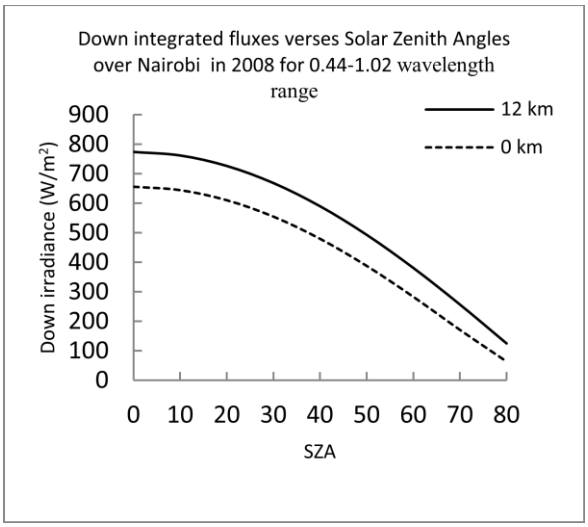

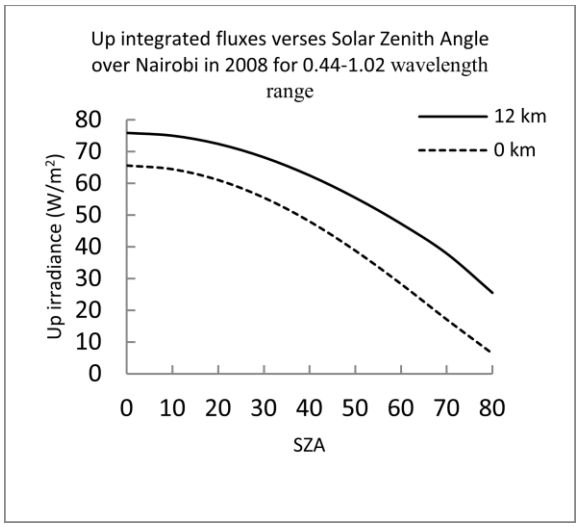

a b

Figures 5.19a-b: Modeled integrated fluxes of down and up irradiance at 12 km and 0 km above sea level for varying SZAs respectively over Nairobi in 2008.

Both down and up integrated irradiance decrease with increasing optical air mass factor (increasing SZAs) as indicated in Figure 5.19a and b. The net down and up integrated irradiance over Nairobi from 2006 to 2008 was noted to vary with aerosol number densities at the two atmospheric levels. Variations in net down and up integrated fluxes at zero SZA are shown in Table 5.8 together with the up/down ratio between the periods of study.

Table 5.8: Variation in net integrated fluxes at the two atmospheric levels over the study sites.

Site	Year	Net down (W/m^2)	Net up (W/m^2)	Up/down
Nairobi	2006	121.98	12.89	0.1065
	2007	103.24	11.33	0.1098
	2008	118.38	12.09	0.1023
Mbita	2007	114.36	11.97	0.1047
Malindi	2008	130.76	14.15	0.1082

Variations in integrated fluxes over Nairobi at the two atmospheric levels reflect the variation in aerosol number densities as indicated in Table 5.6. An increase in aerosol number densities in the wavelength channels under consideration from 2006-2007 time interval translates to an increase in the up/down integrated flux ratio by about 3.1 %. Thus, an increase in aerosol number concentration allows for more attenuation of incoming solar radiation through absorption and scattering. On the other hand, a decrease in aerosol number density from 2007-2008 translates to a decrease in the ratio by about 6.8 % since incoming solar radiation attenuation is enhanced between the two atmospheric levels. It was also noted that the up to down ratio in Table 5.8 remains virtually constant over the study sites. This implies that the radiant flux lost in the entire

spectrum under consideration over the three study sites is almost constant and significant changes can only be noted after a full solar cycle.

5.8.3 Radiative Forcing Impacts Due to Atmospheric Aerosols

Radiative forcing is the change in the net radiation either at the top of the atmosphere or Earth's surface due to secular variations in the concentrations of radiative active species e.g. aerosols. A positive change in the flux implies a warming effect on the earth by the sun and vice versa for a negative flux. Radiative forcing effects of aerosol particles on the surface of the earth for the studied sites was accomplished by use of equation 3.24 and is shown in Table 5.9 at zero SZA.

Table 5.9: Radiative forcing due to aerosol particles over the study sites.

Site	Year	Net Integrated Flux (W/m^2)	Radiative Forcing $K/(W/m^2)$
Nairobi	2006	592.74	0.46
	2007	601.29	0.45
	2008	590.46	0.46
Mbita	2007	593.73	0.46
Malindi	2008	578.97	0.47

Radiative forcing impacts due to aerosols remain virtually constant throughout the study period over Nairobi. Like wise, Mbita and Malindi do reflect almost the same values as compared to that of Nairobi. This implies that the impact of changes in secular climate drivers e.g. aerosols on radiative forcing is almost uniform over Kenya and is approximated as $0.46\ K/(W/m^2)$.

CHAPTER 6

CONCLUSIONS AND FUTURE OUTLOOK

6.0 Conclusions

An attempt to explain the temporal characteristics of τ with respect to weekly total rainfall and temperature was a success. The multivariate nature of environmental data calls for advanced tools of analysis. The use of multivariate techniques i.e. PCA and PLS-DA, PCR and HCA in the study of both temporal and spatial characteristics for τ and α weekly average values over the study sites was achieved. Temporal characteristics in both τ and α are modulated by weekly total rainfall, relative humidity, temperature, local air circulation patterns, aerosol mode of generation and composition together with the urban heat island effect over the study sites.

Local air circulation (for both Malindi and Mbita) as a result of the Indian Ocean and Lake Victoria respectively and urban heat island effects (for Nairobi) enhances aerosol transportation over the study sites. This explains the spatial characteristics that are seen to be particle size

independent over each site. Classifications in both τ and α for an individual site is depend on aerosol characteristics e.g. aerosol mode of formation, aerosol burden, aerosol mixture composition, hygroscopic property relative humidity and temperature. Wet deposition of aerosol particles is particle size independent and supersedes dry deposition; spectral dependence of τ varies with aerosol number density that changes with weekly total rainfall over Nairobi. There was no significant spectral dependence in ω, g and both n and k at zero SZA over the study sites. Wet deposition of aerosol particles over Mbita dominates in the shorter wavelengths (particle sizes) attributed to both local air circulation between the site and Lake Victoria.

Both τ and α value agreed to within reasonable levels of accuracy, this shows consistency in the two remote sensing techniques. Annual variation in the spectral irradiance, integrated fluxes and reflectance was noted due to changes in aerosol number densities over Nairobi. Variation in spectral irradiance was significant in 675 nm and 870 nm wavelength channels that may be due to the dominance by aerosol particles originating from vehicular, industrial emissions and urban heat effect over Nairobi. There was a declining loss in radiant energy with increasing aerosol particle sizes over sites of study. The variation in up and down irradiance between 12 km and 0 km atmospheric levels with respect to optical air mass factor may translate to either a cooling or heating effect on the earth's surface. The radiant flux lost in the entire spectrum under consideration remained constant. The radiative forcing effect calculated from aerosol optical properties remained relatively constant at $0.46\,K/(\mathrm{W/m^2})$ despite the observed differences in the various aerosol particle properties dominating the each site.

6.1 FUTURE OUTLOOK

Other than AERONET network that is limited to three locations in the entire country (Kenya), there is a need to perform size-fractionated trace chemical and radiogenic analysis and characterization of environmental aerosols using chemometric-based spectroscopic methods. This increases the capacity to model and predict aerosol dynamics as well as diagnose and classify aerosol-derived environmental risk (health, climate, pollution) episodes in the country in relation to meteorological parameters, season and geography (spatial variability) over carefully chosen sites that represent the entire country. Impacts of other atmospheric constituents e.g.

green house gases and trace gases together with clouds and their environmental risks need to be quantified over the study region.

It is important to note that atmospheric aerosols are not the only active species responsible for the modulation of radiative characteristics and hence climate. There is a need to retrieve and radiatively model aerosol characteristics in relation to greenhouse densities over selected Kenyan atmosphere utilizing AERONET and MAX-DOAS measurements among other aerosol campaigns.

References

Ackermann, J. (1998). The extinction–to–backscatter ratio of atmospheric aerosol: a numerical study, *J. Atmos. Ocean. Technol*. **15**, 1044-1050.

Alados-Arboledas, L., Lyamani, H. and Olmo, F. J. (2003). Aerosol size properties at Armilla, Granada (Spain), Q. *J. R. Meteorol. Soc.*, **129,** 1395-1413.

Alados-Arboledas, L., Lyamani, H. and Olmo, F. J. (2004). Long-term changes in aerosol radiative properties at Armilla (Spain), *Atmos. Environ.*, **38,** 5935-5943.

Alexandridis, A., Haralambos, S. and Bafas, G. (2004). Modeling and control of continous digesters using the PLS methodology, *Chem. Eng. Comm.* **191,** 1271-1284.

Alpert, P., Kaufman, Y.J., Shay-el, Y., Tanre, D., Da Silva, A. and Joseph, Y.H. (1998). Dust forcing of climate inferred from correlation between dust data and model errors, *Nature*, **395**, 367-370.

Angstrom, A. (1964). The parameters of atmospheric turbidity, *Tellus*, **16**, 64-75.

Angstrom, A. (1929). On the atmospheric transmission of sun radiation and on dust in the air, *Geografiska. Annaler.* **2,** 156-166.

Badarinath, K. V. S., Sharma, A. R. and Shailesh, K. M. (2009). Impact of emissions from anthropogenic sources on satellite-derived reflectance, *Advances in Space Research,* **43,** 1545-1554.

Balkanski, Y., Schulz, M., Chaquin, T. and Guibert, S. (2007). Reevolution of mineral aerosol radiative forcings suggest a better agreement with satellite and AERONET data, *Atmos. Chem. Phys.***7,** 81-95.

Bolle, H.J. (1977) Radiation in the atmosphere, *Science press, Princeton.*

Brimblecombe (1996), Air Composition and Chemistry, Cambridge University Press.

Cachorro, V.E., Duran, P., Vergaz, R. and de Frutos, A.M. (2000). Columanar physical and radiative properties of atmospheric aerosols in north central Spain, *J. Geophys. Res.* **105(D6),** 7161-7175.

Cook J., Highwood, E.J., Coe, H., Formenti, P., Haywood, J.M. and Crosier, J. (2007). A comparison of aerosol optical and chemical properties over Adriatic and Black Seas during summer 2004: Two case-studies from ADRIEX, *Q.J.R. Meteorol. Soc,* **133:**(S1) 33-45.

D'Almeida, G.A., Koepke, P. and Shettle, E.P., (1991). Atmospheric aerosol-global climatology and radiative characteristics, *A. Deepak, Hamphy,* Volume 561 pp.

Di Lorio, T., di Sarra, A., Junkermann, W., Cacciani, M., Fiocco, G. and Fua, D. (2003). Tropospheric aerosols in the Mediterranean: 1. Microphysical and optical properties, *J. Geophys. Res.,* **108(D10),** 4316-4333.

Dubovik, O., Holben, B.N., Eck, T.F., Smirnov, A., Kaufman, Y.J., King, M.D., Tanre, D. and Slutsker, I. (2002).Variability of absorption and optical properties of key aerosol types observed in worldwide locations, *J. Atmos. Sci*. **59**, 590-608.

Dubovik, O., Holben, B.N., Kaufman, Y.J., Yamasoe, M., Smirnov, A., Tanre, D. and Slutsker, I. (1998). Single scattering albedo of smoke retrieved from the sky radiance and solar transmittance measured from the ground, *J. Geophys. Res.* **103,** 31903-31923.

Eck, T.F., Holben, B.N., Slutsker, I. and Setzer, A. (1998). Measurements of irradiance attenuation and estimation of Single Scattering Albedo for biomass burning aerosols in Amazonia, *J. Geophys. Res.,* **103**, 31865-31878.

Ghan, S. J., McFarquahar, G., Korolev, A., Liu, P., Strapp, W., Verlinde, H. and Wolde, M. (2008). ISDAC Flight Planning Document, DOE/SC-ARM-0801.

Gemperline, P. (2006). Practical guide to chemometrics, *Taylor and Francis Group.*

Hanel, G. (1994). Optical properties of atmospheric particles: Complete parameter sets obtained through polar photometry and an improved inversion technique, *Appl. Opt.,* **33,** 7187-7199.

Hansen, J., Sato, M. and Ruedy, R. (1997). Radiative forcing and climate response, *J Geophys. Res*. **102(D6)**, 6831-6864.

Hansen, J., Sato, M., Lacis, A. and Ruedy, R. (1998).The missing climate force, *Philos. Trans. R. Soc.* London B **352**, 231-240.

Harrisson, R.M., Shi, J.P. and Jones, M.R. (1999). Continous measurements of aerosol physical properties in urban atmosphere, *Atmos. Environ.* **33,** 1037-1047.

Hatzianastassiou, N, Katsoulis, b, and Vardavas.L. (2004) Sensitivity analysis of aerosol direct radiative forcing in ultraviolet-visible wavelengths and consequences for the heat budget. *Tellus* **56B** 368-381.

Haywood, J. M. and Shine, K. P. (1995).The effect of anthropogenic sulfate and soot aerosol on 25 clear sky planetary radiation budget, *Geophys. Res. Lett.***22**, 603-606.

Haywood, J.M., Roberts, D.L., Slingo, A., Edwards, J.M. and Shine K.P. (1997). General circulation model calculation of the direct radiative forcing by anthropogenic sulfate and fossils-fuel soot aerosols, *J. climate,***10,** 1562-1577.

Hedge, P., Sudheer, A. K., Sarin, M. M. and Manjunatha, B. R. (2007). Chemical characteristics of atmospheric aerosols over Southwest coast of Indian, *Atmospheric Environment,* **41,** 7751-7766.

Hedwig, D. and Maenhaut, W. (1990). Application of principal component and cluster analysis to the study of the distribution of minor and trace elements in normal human brain, *Chemometrics and Intelligent Laboratory Systems,* **9,** 273-286.

Hess, M., Koepke, P. and Schult, I. (1998). Optical properties of aerosols and clouds: The software package OPAC, *Bull. Am. Meteorol. Soc*. **79,** 831-844.

Holben, B. N., Eck, T.F., Slutsker, I., Tanre, D., Buis, J.P., Setzer, A., Vermote, E., Reagan, J.A., Kaufman, Y.J., Nakajima, T., Lavenu, F., Jankowiak, I. and Smirnov, A. (1998). AERONET-A federated instrument network and data archive for aerosol characterization, *Remote sens. Environ*. **66,** 1-16.

Holben, B. N., Eck, T.F., Slutsker, I., Tanre, D., Buis, J.P., Setzer, A., Vermote, E., Reagan, J.A., Kaufman, Y.J., Nakajima, T., Lavenu, F., Jankowiak, I. and Smirnov, A**.** (2001). An emerging ground based aerosol climatology: Aerosol optical depth of AERONET, *J. Geophys. Res.* **106,** 12067-12097.

Ichoku, C., Robert, L., Kaufman, Y.J., Remmer, L.A., Rong-Rong, Li., Vanderlei, J.M., Holben, B.N., Abuhasan, N., Slutsker, I., Eck, T.F., and Pietras, C. (2002). Analysis of the performance characteristics of the five channel micro tops ii sun photometer for measuring aerosol optical thickness and precipitable water vapor, *J. Geophys. Res*. **107**, No. D13, 10.1029/2001JD001302.

Intergovernmental panel on climate change (IPCC). (2001). Climate Change 2001: *The specific basis. Contribution of working group 1 for the third assessment report.* Houghton, J.T., Ding, Y., Griggs, D. J., Noguer, M., Van der Linden, P. J., Dac, X., Maskell, K., Johnson, C. A. (eds.) Cambridge University Press: UK.

Intergovernmental panel on climate change (IPCC). (2007). Climate Change 2007: *The specific basis. Contribution of working group 1 for the fourth assessment report. Assesment Report of the Intergovernmental Panel on Climate Change* [Solomon, S., Qin, D., Manning, M., Chen, Z., Marquis, M., Averyt, K.B., Tignor, M. and Miller, H. L. (eds)]. Cambridge University Press, Cambridge, United Kingdom and New York, NY, USA. 131-234.

Jaenicke, R. (1993). Tropospheric aerosols in *Aerosol-Cloud-Climate interactions,* (Ed. P.V. Hobbs), *Int. Geophys. Series,* **54,** *Academic Press, San Diego, Califonia*, pp 1-31.

Johansen, A. M., Siefert, R. L. and Hoffmann, M. R. (2000). Chemical composition of aerosols collected over the tropical North Atlantic Ocean, *J. Geophys. Res,* **105,** 15277-15312.

Johnson, B.T., Christopher, S., Haywood, J.M., Osborne, S.R., McFarlane, S., Hsu, C., Salustro, C. and Kahn, R. (2009). Measurements of aerosol properties from aircraft, satellite and ground-based remote sensing: A case study from the Dust and Biomass-burning Experiment (DABEX). *Q.J.R. Meteorol. Soc.***D01**: 10.1002.qj.420.

Johnson, B.T., Osborne, S.R., Haywood, J.M. and Harrison, M.A.J. (2008). Aircraft measurements of biomass burning aerosol over West Africa during DABEX. *J. Geophys. Res.* **113**: D00C06, D0I:10.1029/2007JD009451.

Kato, S., Ackerman, T.P., Mather, J.H., and Clothiaux, E.E., (1999) The K-distrbution method and correlated-k approximation for shortwave radiactive transfer model, *J. Quant. Spectrose. Radiat.Transfer* **62**,109-121.

Khoder, M. I. and Hassan, S. K. (2008). Weekday/weekend differences in ambient aerosol level and chemical characteristics of water-soluble components in the city centre, *Atmospheric Environment,* **42,** 7483-7493.

Kikas, U., Reinhart, A., Vaht, M. and Veismann, U. (2001). A case study of the impact of boundary layer aerosol size distribution on the surface UV irradiance, *Atmos. Environ.* **35,** 5041-5051.

Krekov G.M., (1993). Models of atmospheric aerosols. In Aerosol effects on climate, Jennings S.G. (ed.) *University of Arizona Press*:Tucson, Arizona.

Laakso, L., Tareq, H., Aarnio, P., Komppula, M., Veijo, H., Viisanen, Y. and Markku, K. (2003). Diurnal and annual characteristics of particle mass and number concentrations in urban, rural and Arctic environments in Finland, *Atmos. Environ.* **37,** 2629-2641.

Lacis, A.A. and Mishchenko, M.I. (1995). In: Charlson, R.J., Hietzenberg, J.(Eds.), Climate Forcing, Climate Sensitivity and Climate Response: A radiative modeling perspective on Atmospheric Aerosols, in Aerosol Forcing of Climate, John Wiley, New York, pp. 11-42.

Lenoble, J. (1991). The particulate matter for biomass burning: A tutorial and critical review of its radiative impact. *Global Biomass burning: Atmospheric climate and biospheric implications*, J. S. Levine, Ed., MIT press 381-386.

Leon, J.F., Chazette, P., Pelon, J., Dulac, F. and Randriamiarisoa, H. (2002). Aerosol direct radiative impact over the INDOEX area based on passive and active remote sensing. *J. Geophys. Res.*, **107(D19).**

Levin, Z., Joseph, J.H. and Mekler, Y. (1980). Properties of sharav (Khasim) dust – Comparison of optical and direct sampling data, *J. Atmos. Sci.,* **37**, 1270-1278.

Levoni, C., Cervino, M., Guzzi, R. and Torricella, F. (1997). Atmospheric aerosol optical properties: a data base of radiative characteristics for different components of classes, *Appl. Opt.* **36,** 8031-8041.

Li, F., Vogelman, A.M. and Ramanathan, V. (2004). Saharan dust aerosol Radiative forcing measured from space. *J. Climatol.* **17,** 2558-2571.

Li, J. and Mao, K (1990). Properties of atmospheric aerosols inverted from optical remote sensing, *Atmos. Environ.,* **24A**, 2517-2522.

Li, Z., Xiangao, Xia, Maureen. C., Wen Mi, Holben, B., Pucai,W., Hongbin, C., Si-Chee,Tsay., Eck, T.F., fengsheng,Z., and Dutton. E.G. (2007).Aerosol optical Properties and their radiative effects in northern china. *J. Geophys.Res*. **112,** D22501, doi:10291 2006JD007382

Liousse, C. and Cachier, H. (1995). Measurement of black carbon aerosol in the atmosphere of two different source regions – Real time data for Paris region and Savanna site of the Ivory Coast, *Environ. Technol.,* **13**, 959-967.

Menon, S., Hansen, J., Nazarenko, L. and Luo, Y.F. (2002). Climate effects of black carbon aerosols in China and India, *Science*, **297**, 2249-2252.

Mönkkönen, T., Pai, P., Maynard, A., Lehtinen, K.E.J., Hämeri, K., Rechkemmer, P., Ramachandran, G., Prasad, B. and Kulmana, M. (2005). Fine particle number and mass concentration measurements in urban India households, *Science of the Total Environment.* **347,** 131-147.

Myhre, G., Stordal, F., Restad, R. and Isaksen I. S. A. (1998). Estimates of the direct radiative forcing due to sulfate and soot aerosols, *Tellus*, **5OB,** 463-477.

Nair, P.R., Susan, K.G., Parameswaran, K., Marina, A., Alappattu, D.P., Mannil, M. and Kunhikrishnan, P.K. (2009). Short-term changes in the aerosol characteristics at Kharagpur (22^{o}

19’ N, 87^{o} 19’ E) during winter, *Journal of Atmospheric and solar terrestrial Physics.* Doi: 10.1016/j.jastp.2009.06.010.

Osborne, S.R., Johnson, B.T., Haywood, J.M., Baran, A.J., Harison, M.A.J. and McConnell, C.L. (2008). Physical and optical properties of mineral dust aerosol during the Dust and Biomass-burning Experiment, *J. Geophys. Res.* **113:** D00C03, DOI: 10.1029/2007JD009551.

Otterman, J., Fraser, R.S. and Bahethi, O. P. (1982). Characterization of tropospheric desert aerosols at solar wavelength by multispectral radiometry from Landsat, *J. Geophys. Res.* **87,** 1270-1278.

Penner, J. E., Dickinson, R.E. and O’Neill, C. A. (1992). Effects of aerosol from biomass burning on the global radiation budget, *Science.* **256,** 1432-1434.

Penner, J. E., Zang, S.Y., Chin, M., Chuang, C. C., Feicher, J., Feng, Y., Geogdzhayer, I. V., Ginoux, P., Herzog, M., Higurashi, A., Koch, D., Land, C., Lohmann, U., Mishchenko, M., Nakijima., T., Pitari, G., Soden, B., Tegen, I. and Stowe, L. (2002). A comparison of model and satellite- derived aerosol optical depth and reflectivity, *J. Atmos. Sci.* **59,** 441-460.

Perrone, M. R., Santese, M., Tafuro, A.M., Holonben, B. and Smirnov A. (2005). Aerosol load characterization over south-east Italy for one year of AERONET sun photometer measurements, *J. Atmos. Res.* **75,** 111-133W.
Qiu, J, Liquan, Y, and Xiaoye, Z. (2004). Characterization of imaginary part and single scattering albedo of urban aerosols in Northern China, *Tellus* **56B**, 276-284.

Ramanathan, V., Crutzen, P.J., Kiehl, J.T. and Rosenfeld, D. (2001). Aerosol, climate and the hydrological cycle, *Science* **294,** 2119-2124.

Ramaswamy, V., Boucher, O., Haigh, J., Hauglustaine, D., Haywood, J., Myhre, G., Nakijama, T., shi, G. Y. and Solomon, S. (2001): Radiative forcing of climate change. In: Climate change in 2001: The Specific Basis. Contribution of the working group 1 to the Third Assessment Report of the IPCC [Houghton et. al. (eds.)]. Cambridge University Press, United Kingdom and New York, NY, USA, 349-416.

Reagan, J.A., Thomason, L.W., Herman, B.M. and Palmer, J.M. (1986). Assessment of atmospheric limitations on the determination of the solar spectral constant from ground –based spectra radiometer measurements, *IEEE Trans. Geosci. Remote Sens*, **GE-24**,258-265.

Sabbah, I., Ichoku, C., Kaufman, Y.J. and Remer, L. (2001). Full year cycle of desert dust spectral optical thickness and precipitable water vapor over Alexandria, Egypt, *J. Geophys. Res.*, **106**, 18305-18316.

Seinfeld, J.H. and Pandis, S.N. (1998). Atmospheric Chemistry and Physics, Wiley Interscience, New York.

Sharma, D.K., Rai, J., Israil, M. and Pratap, S. (2003). Summer variation of atmospheric aerosol number concentrations over Roorkee, India. *Journal of atmospheric and solar terrestrial physics.* **65,** 1007-1019.

Shettle, E.P. and Fenn, R. W. (1979). Models of aerosols of lower troposphere and effect of humidity variations on their optical properties, AFCRL. *The. Rep* 79021; Air Force Cambridge Research Laboratory, Hanscom Air Force Base, MA, 100pp.

Smirnov, A., Holben, B.N., Eck T. F., Dubovik, O., Frouin, R. and Slutsker I.(2003). Maritime component in aerosol optical models derived from AERONET data, *J. Geophys. Res.* **108,** 433.DOI 10.1029/2002JD002701.

Sokolik, I. N. and Toon, O. B. (1996). Direct radiative forcing by anthropogenic airborne mineral aerosols, *Nature.* **381,** 681-683.

Stanier, C.O., Khlystov, A.Y. and Pandis, S.N. (2004). Ambient aerosol size distributions and number concentrations measured during the Pittsburgh Air Quality Study (PAQS), *Atmos. Environ.* **38,** 3275-3284.

Toledano, C., Cachorro, V.E., Berjon, A., de Frutos, A.M., Sorribas, M., de la Morena, B. A. and Goloub, P. (2007). Aerosol optical depth and Angstrom exponent climatology at El Arenosillo AERONET site (Huelva, Spain), *Q.J.R. Meteorol. Soc.* **133,** 795-807.

Toledano, C., Wiegner, M., Garitammer, M., Seefeldner, M., Gasteiger, J., Műller, D. and Koepke, P. (2009). Spectral aerosol optical depth characterization of desert dust during SAMUM 2006, *Tellus,* **61B,** 216-228.

Twomey, S. (1991). Aerosol, cloud and Radiation, *Atmos. Environ.,* **25,** 2435-2442.

Vergaz, R., Cachorro, V.E., de frutos, A.M., Vilaplana, J.M. and de la morena (2005). Columna characteristics of aerosols by spectroradiometer measurements in the maritime area of the Cadiz Gulf (Spain), *Int. J. Climatol.* **25,** 1781-1804.

Weast R. (ed.) (1985). *Handbook of Chemistry and Physics,66th edition.CRC Pres,*Florida.

Wenny, B.N., Schafer, J.S., Deluisi, J.J., Saxena, V.K., Barnard, W.F., Petropavlovskikh, I.V. and Vergamini, A.J. (1998). A study of regional aerosol radiative properties and effects on ultraviolet-B radiation, *J. Geophys. Res.* **103,** 17083-17097.

Westaphal, D. L. and Toon, O. B. (1991). Simulations of microphysical radiative and dynamical process in a Continental- scale Forest fire smoke plume, *J. Geophys. Res.* **96**, 22379-22400.

Whitby, K.T. (1978) The physical characteristics of sulfur aerosols. *Atmos. Environ.* **12,** 135-159.

Wittrock, F., Oetjen, H., Richter, A., Fietkau, S., Medeke, T., Rozanov, A. and Burows, J.P. (2004) MAX-DOAS measurements of atmospheric trace gases in Ny-Ålesund-Radiative transfer studies and their application, *Atmos. Chem. Phys.,* **4,** 955-966.

WMO (1983). Radiative commission of IAMAP meeting of experts on aerosols and their climatic effects. World Metrological Organization Rep. WCP55, 28-30.

World Climate Program (WCP) (1986). A Preliminary Cloudless Standard Atmosphere for Radiation Computation *World Meteorol Organization*: Geneva.

Xia Xiang-ao, Chen Hong-Bin, Wang Pu-Cai, Zong Xue-Mei, Qiu Jin-Huan and Philippe Gouloub, Lageo. (2005). Aerosol properties and their spatial and temporal variations over north China in spring 2001, *Tellus*, **57B,** 28-39.

Yu, S., Saxena, V.K., Wenny, B.N., Deluisi, J.J., Yue, G.K. and Petropavlovskikh, I.V. (2000). A study of the aerosol radiative properties needed to compute aerosol forcing in the southern United States, *J. Geophys. Res.* **105,** 24739-24749.

Zege, E.P., Ivanov, A.P. and Katsev, I.L. (1991). Image transfer through a scattering medium. Springer-Verlag, New York.
Zhonghai, J. and Stamnes, K. (1994). Radiative transfer in nonuniformly refracting layered media: Atmosphere-ocean system, *Applied optics,***33, No. 3,** 431-442.

Zhonghai, J., Thomas, P., Charlock, Rutledge, K., Stamnes, K. and Yingjian, W. (2006). Analytical solution of radiative transfer in the coupled atmosphere-ocean system with a rough surface, *Optics,***45, No. 28,** 7443-7455.

Zhonghai, Jin "National Aeronautics and Space Administration" Coupled Ocean and Atmosphere Radiative Transfer. From January 2008 to August 2009.
http://www.cave.larc.nasa.gov/cave/.

Appendix

Table 7.1: Annual averages of rainfall data over Nairobi from 2006-2008

Year	Annual rainfall data (mm)
2006	41.06
2007	35.90
2008	40.09

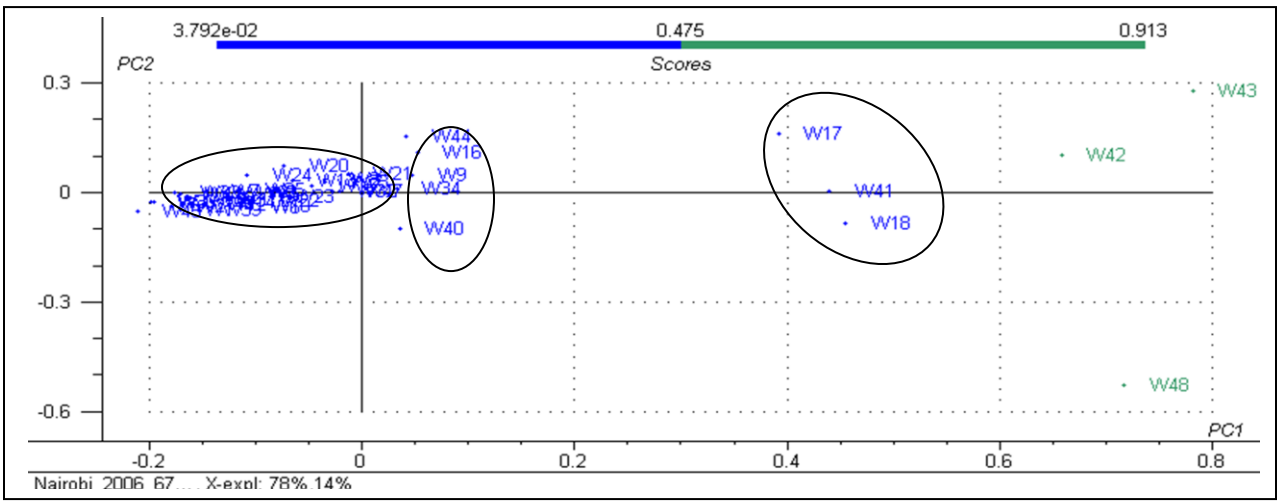

Figure 7.1: Example of plot of scores for 48 samples in four variables data set at λ=675 nm for Nairobi (2006)

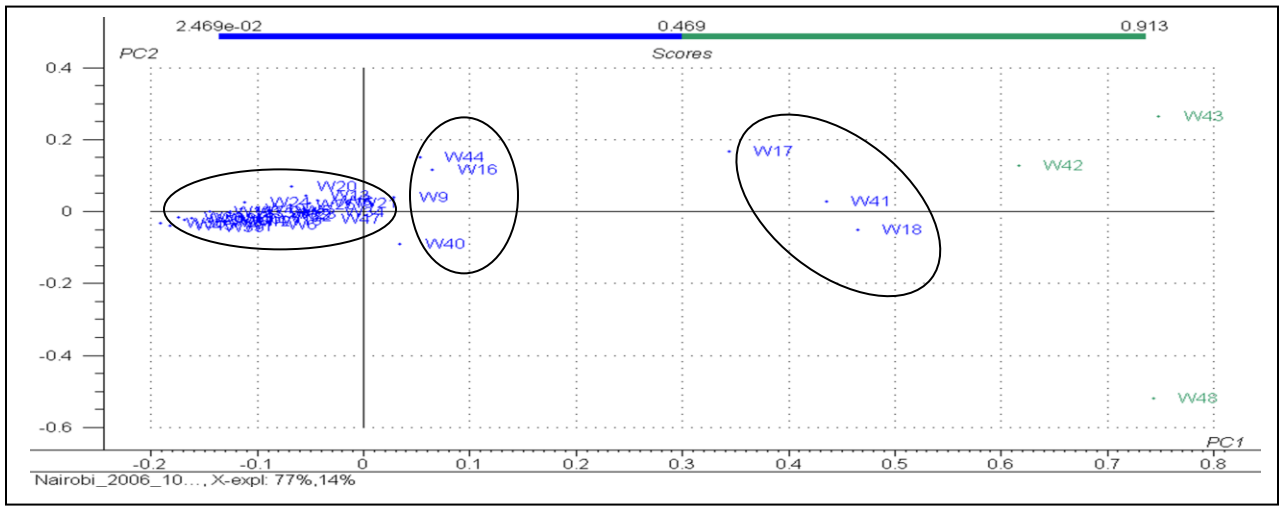

Figure 7.2: Example of plot of scores for 48 samples in four variables data set at λ=1020 nm for Nairobi (2006)

Table 7.2: Weekly averages of selected meteorological parameters over study sites

Week	Nairobi (2006)			Mbita (2007)			Malindi (2008)		
	Rainfall(mm)	R/H (%)	Temp (^{0}c)	Rainfall(mm)	R/H (%)	Temp (^{0}c)	Rainfall (mm)	R/H (%)	Temp (^{0}c)
W1	8.70	70.71	18.47	23.57	70.50	23.05	7.86	72.85	26.45
W2	3.75	64.10	20.72	7.86	68.35	23.75	7.53	69.09	25.72
W3	7.00	68.41	19.57	42.71	73.40	23.16	6.37	71.42	24.57
W4	5.67	62.37	19.99	21.50	72.22	23.97	35.36	67.87	24.99
W5	5.94	62.57	19.92	36.57	75.50	23.77	77.86	68.57	24.92
W6	4.90	60.42	21.06	18.57	68.57	23.92	55.13	75.71	26.85
W7	4.56	61.90	21.48	0	49.24	25.58	0	64.85	25.85
W8	18.50	66.48	22.12	0	47.60	23.78	18.78	79.52	26.66
W9	30.95	72.42	18.67	2.85	63.85	24.96	185.43	81.42	28.42
W10	15.50	71.78	18.40	42.85	62.07	24.62	25.56	82.28	28.14
W11	17.29	70.44	17.01	50.92	64.73	23.30	8.43	74.64	25.64
W12	39.33	69.81	20.49	7.60	58.42	24.72	44.33	73.81	25.49
W13	45.38	73.64	18.52	0	49.14	25.81	285.43	79.64	26.71
W14	35.90	79.28	19.25	50.71	67.35	24.22	31.65	79.28	26.25
W15	83.85	70.80	18.60	100.86	60.65	23.36	71.57	80.80	25.21
W16	40.75	83.53	18.85	73.89	78.38	24.13	44.50	69.53	24.85
W17	93.86	83.71	19.07	33.34	70.07	24.01	31.57	69.71	24.14
W18	125.50	83.78	19.06	4.71	64.35	24.60	5.95	68.78	24.68
W19	0	76.79	18.07	40.71	71.59	23.39	0	63.79	24.42
W20	30.56	75.71	18.04	2.70	65.71	24.13	0	61.71	25.55
W21	0.71	77.21	16.22	65.86	68.42	23.20	0	62.21	24.14
W22	11.25	76.35	14.89	69.29	75.35	22.42	0	61.35	23.89
W23	0	73.66	13.74	20.00	64.58	23.12	0	66.96	24.64

W24	0.87	75.99	10.02	0	48.58	22.91	17.75	72.99	23.64
W25	0	77.20	10.77	35.43	71.35	22.45	0	61.34	23.85
W26	0.37	82.64	09.42	0	63.07	23.15	0.18	74.85	24.42
W27	2.85	76.08	10.63	5.86	56.14	23.07	0.14	72.28	24.57
W28	40.00	80.49	09.77	0	47.97	23.56	9.75	79.43	24.77
W29	45.86	76.71	09.57	0	47.64	22.61	47.86	77.14	23.85
W30	5.75	73.42	09.00	0	51.07	22.37	8.58	72.85	23.27
W31	0	68.61	09.50	12.42	64.08	22.83	0	67.14	23.67
W32	16.56	70.72	14.31	0.41	60.67	23.79	14.58	69.64	24.80
W33	5.57	69.07	16.85	16.00	73.42	22.63	8.43	68.57	23.42
W34	0.75	75.14	17.27	0	45.28	22.03	104.21	78.57	23.26
W35	57.00	72.93	19.25	0.45	63.19	23.01	5.27	71.76	23.25
W36	0.85	68.23	18.19	0	62.72	23.82	0.12	66.18	23.19
W37	0	63.21	20.35	32.86	67.42	23.94	0	62.85	20.35
W38	10.50	66.57	19.35	8.71	64.71	23.99	10.05	67.14	24.35
W39	17.43	67.13	19.90	0	59.47	24.47	7.51	66.85	25.90
W40	26.11	69.68	20.42	99.70	57.93	23.92	46.46	69.09	24.42
W41	0	69.78	19.11	47.29	69.34	23.15	54.71	80.28	24.11
W42	0	68.57	18.64	11.71	62.14	23.37	15.25	85.71	24.64
W43	0	70.04	18.98	70.12	65.66	23.50	114.57	71.07	24.98
W44	8.75	71.04	18.21	39.11	62.31	24.00	237.50	82.04	24.21
W45	8.71	78.21	19.25	5.85	52.28	23.52	21.57	78.21	26.25
W46	80.00	77.14	18.33	132.57	73.45	22.12	7.86	77.57	23.33
W47	44.45	73.44	18.77	0	61.49	23.90	35.43	73.85	24.77
W48	0	71.91	19.32	14.10	61.67	24.15	184.65	83.45	23.32

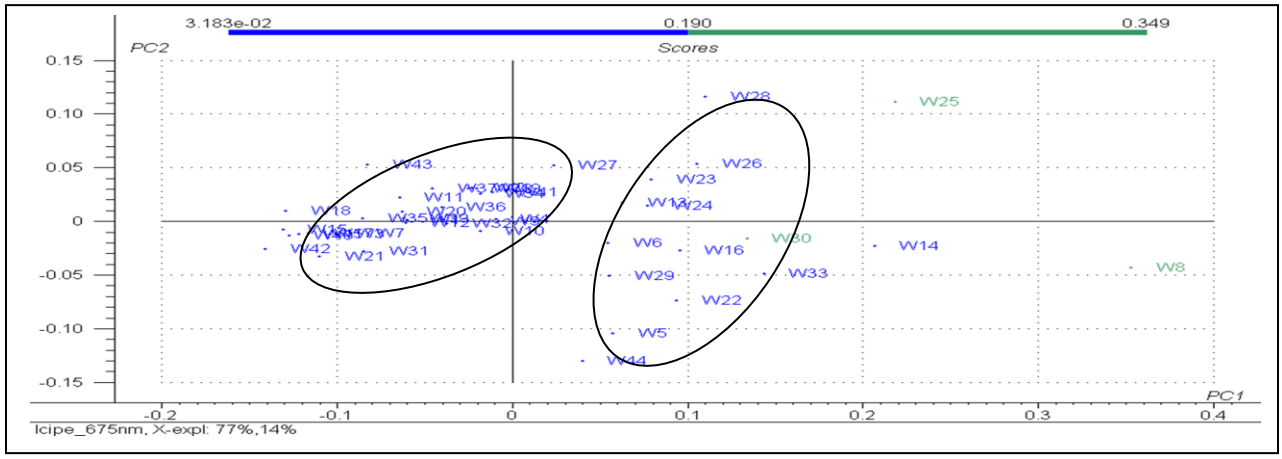

Figure 7.3: Example of plot of scores for 48 samples in four variables data set at λ=675 nm for Mbita (2007)

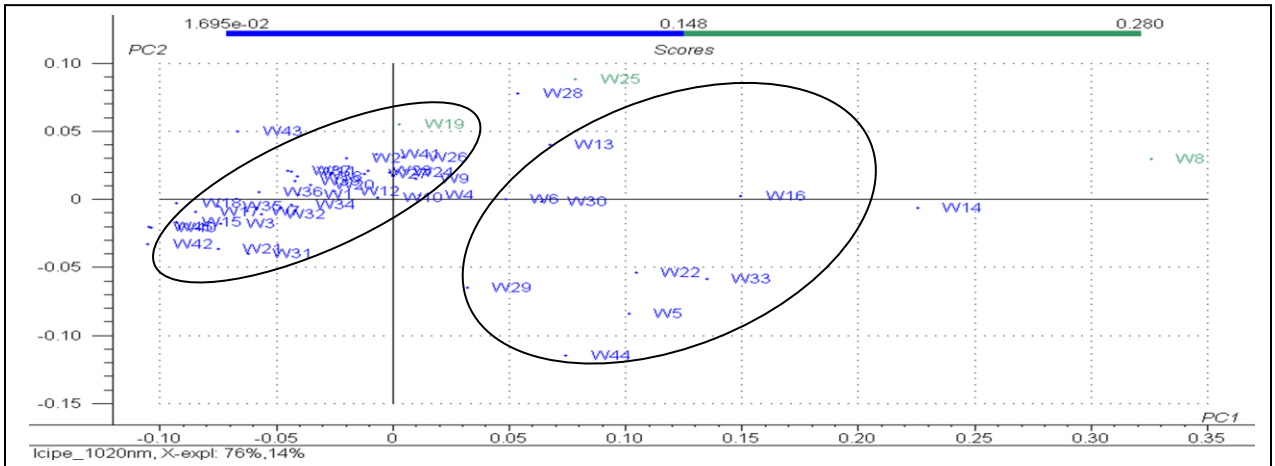

Figure 7.4: Example of plot of scores for 48 samples in four variables data set at λ=1020 nm for Mbita (2007)